High-Frequency Ultrasound Analysis of Soft Material Characterization

by

Koushik Paul

A Dissertation Presented in Partial Fulfillment
of the Requirements for the Degree
Doctor of Philosophy

Approved February 2022 by the
Graduate Supervisory Committee:

Leila Ladani, Chair
Jafar Razmi
Julianne Holloway
Xiangjia Li
Yongming Liu

ARIZONA STATE UNIVERSITY

May 2022

ABSTRACT

Ultrasound has become one of the most popular non-destructive characterization tools for soft materials. Compared to conventional ultrasound imaging, quantitative ultrasound has the potential of analyzing detailed microstructural variation through spectral analysis. Because of having a better axial and lateral resolution, and high attenuation coefficient, quantitative high-frequency ultrasound analysis (HFUA) is a very effective tool for small-scale penetration depth application. One of the QUS parameters, peak density had recently shown a promising response with the variation in the soft material microstructure. Acoustic scattering is arguably the most important factor behind different parametric responses in ultrasound spectra. Therefore, to evaluate peak density, acoustic scattering at different frequency levels was investigated. Analytical, computational, and experimental analysis was conducted to observe both single and multiple scattering in different microstructural setups. It was observed that peak density was an effective tool to express different levels of acoustic scattering that occurred through microstructural variation. The feasibility of the peak density parameter was further evaluated in ultrasound C-scan imaging. The study was also extended to detect the relative position of the imaged structure in the direction of wave propagation. For this purpose, a derivative parameter of peak density named mean peak to valley distance (MPVD) was developed to address the limitations of peak density. The study was then focused on detecting soft tissue malignancy. The histology-based computational study of HFUA was conducted to detect various breast tumor (soft tissue) grades. It was observed that both peak density and MPVD parameters could identify tumor grades at a certain level. Finally, the study was focused on evaluating the feasibility of ultrasound

parameters to detect asymptotic breast carcinoma i.e., ductal carcinoma in situ (DCIS) in the surgical margin of the breast tumor. In that computational study, breast pathologies were modeled by including all the phases of DCIS. From the similar analysis mentioned above, it was understood that both peak density and MPVD parameters could detect various breast pathologies like ductal hyperplasia, DCIS, and calcification during intraoperative margin analysis. Furthermore, the spectral features of the frequency spectrums from various pathologies also provided significant information to identify them conclusively.

DEDICATION

I would like to dedicate this achievement to my mother, Kabita Paul. Nothing will
be enough to match the amount of sacrifice that you have made in your life for me. Like
all the achievements in my life, this one is a small token of my gratitude for your
unconditional love, care, and support. Without you, this little boy from a small local town
would not be able to come this far. Thank you for always paying interest in what I do.
Thank you for always keeping faith in me. I am proud to be your son. This one is for you,
Ma!

ACKNOWLEDGMENTS

TABLE OF CONTENTS

LIST OF TABLES

LIST OF FIGURES

xiii

CHAPTER 1

INTRODUCTION

Throughout the world, ultrasound analysis has turned out to be a widely-used non-destructive testing method [1][2]. Its application includes but is not limited to determining the characteristics of materials including detecting defects, evaluating the microstructure, and measuring thickness, density, elastic modulus, etc. Compared to other non-destructive testing methods, ultrasound has a higher penetration depth and has less impact on the human body. Also, it is economically cheap which makes it a very common testing tool in today's medical applications [3][4]. This chapter discusses the motivation for this research with a clear problem statement. Then it discusses the currently available and previous technologies associated with the solution and their limitations. After that, it will delineate the potential of ultrasound in solving the problem including the details about ultrasound parameters, ultrasound propagation methods, previous works on ultrasound analysis of tissue characterization. The chapter ends with the research goal and research outline to achieve the goal.

1.1 Problem Statement

Breast cancer or breast carcinoma is an uncontrolled growth of epithelial cells in the breast [5]. It is the second most common cancer in women but can affect men as well [6]. In the United States, Breast Cancer is the most common form of cancer among women. After Lung cancer, it is the second leading cause of death for US women. In 2017, around 63,410 cases of in situ breast carcinoma and 252,710 new cases of invasive breast cancer among US women are expected to be diagnosed. Until breast cancer gets spread to the nearby tissues it does not cause any pain or discomfort which makes breast cancer hard to detect

unless being careful of checking for it regularly. For this reason, breast cancer remains a significant cause of concern in public health [7]. The more traditional way to treat breast cancer is modified radical mastectomy (MRM). Over time due to both emotional and esthetic benefits, breast conservation therapy (BCT) has become the preferred treatment over MRM although MRM offers better local control compared to BCT [8].

Breast-conserving therapy (BCT) is a combination of two different processes called lumpectomy and irradiation therapy. Lumpectomy is the surgery where the lump (breast tumor) along with some surrounding normal tissue (surgical margin) (Fig.1) is excised from the breast. After the surgery, the tumor along with the margin is sent to a pathologist for further microscopic analysis. Most people usually receive radiation therapy of 5 to 7 weeks shortly after lumpectomy to eliminate the existing cancer cells in the rest of the breast tissue. But if the patient is pregnant, has already gone through this process before, has extensive cancer in multiple areas of the same breast then radiation therapy is not recommended to them. Therefore, if abnormalities are found in the margin (positive margin shown in Fig.1a) during the pathological test, the patient has to go through some additional surgery. As a result, to avoid local recurrence (LR), the goal is to obtain a negative (cancer-free) margin shown in Fig.1(b) [9]–[14].
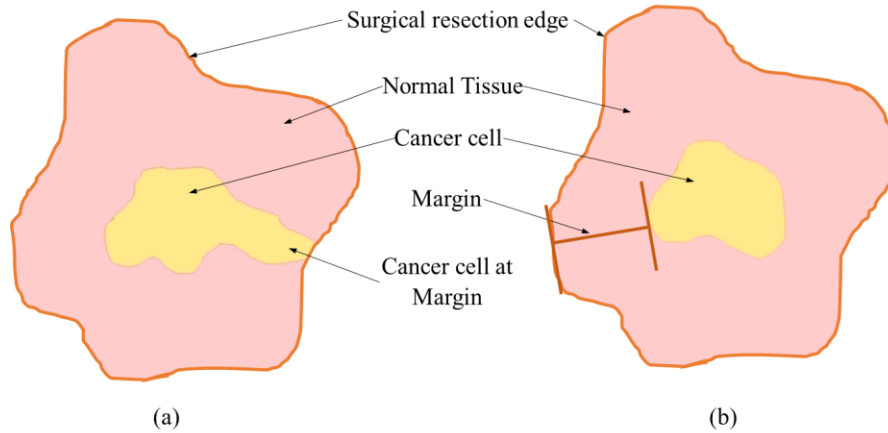
Fig.1　Diagram of (a) positive margin and (b) negative margin

The standard and innovative margin evaluation processes are divided into two categories-pre-operative process and intraoperative process. The preoperative processes include mammography and magnetic resonance imaging (MRI). By screening mammography the tumors can be detected while they are still small [10]. But it was shown that these preoperative processes did not significantly affect the rate of margin re-excision [11][12].

When the margin detection is done during the time of surgery, it is called the intraoperative margin detection process. Some of the intraoperative margin detection processes are frozen section analysis, touch preparation cytology, near-infrared optical imaging (NIF), X-ray diffraction, micro-computed tomography (Micro-CT), X-ray diffraction, and high-frequency ultrasound [15]. During frozen section analysis, the margin is being frozen, sliced, and microscopically analyzed [16][17]. However, this process requires a lot of time and the availability of a pathologist during the surgery. During touch preparation cytology, a glass slide of the specimen is prepared to analyze the margin [16]. The slide preparation can be done in either touch or scrape method. However, this method also requires the

3

accessibility of a cytologist. In addition to that, the process is limited to superficial cells as well as it does not give any margin width information [16]. During near-infrared optical imaging, the fluorescent probes are excited by NIR light which emits photons at a predefined wavelength range. These photons are then detected by the optical imaging system. Based on this technology, a device called Spectroscopic Tissue Scanner has been established which combines both diffuse reflectance spectroscopy and intrinsic fluorescence spectroscopy [18]. The main challenge to make optical NIR technology successful are signal quantification, depth penetration, and the development of imaging agents for human use [16]. The X-ray diffraction process works by defining the material's molecular structure to analyze the structure of the crystalline substance. This technique has been used to create images similar to conventional CT scanners but has been downsized to a smaller scale using so-called micro-CT. But it takes several minutes to perform Micro-CT scans on each specimen [16]. Another intraoperative margin detection process is measuring the electrical properties of tissue. A commercial attempt to create an intraoperative margin assessment device that would evaluate the margin based on its electromagnetic property is called MarginProbe[TM] (Dune Medical Devices Ltd., Israel). It was able to detect malignant tissue within the surgical specimen up to a depth of 1 mm .74 mm [19]. This device is now in clinical practice and also demonstrated constant data and lowered the re-excision rate by more than 50% in overall clinical studies. However, this is also not the perfect solution for margin evaluation as it gives 30% false-positive and also false-negative measurements. False-negative measurements result in re-excision which is completely undesirable [16]. False positive results in further excision of healthy tissue [20].

This research was driven by the necessity of finding an improved intraoperative surgical margin detection process. The goal is to develop an ultrasound measurement as well as imaging technique that would require minimum supervision and at the same time will provide instantaneous accurate data on margin detection.

1.2   Background and Literature Review

This section will discuss the feasibility of various ultrasound parameters for non-destructive analysis (e.g., surgical margin detection). Then it will review previous studies on ultrasound analysis of breast cancer. Lastly, it will discuss the feasibility of medical ultrasound imaging in tissue characterization.

1.2.1   Ultrasound Parameters

Clinical ultrasounds are widely used to examine different organs such as the eye, liver, breast, kidney of the human body [21]. It allows us to study the material through individual analytical measurements as well as to visualize the internal structure. It is shown in some studies that, there is a strong dependence between ultrasonic wave propagation and histological features of tissues including cell structure, cell number density, tissue microstructure, and tissue heterogeneity [22], [23]. Therefore it can be said that ultrasound has the potential to differentiate normal and cancer-affected tissues [16]. There are several benefits of using ultrasound. Ultrasound machines occupy comparatively much smaller space and are easy to carry. These machines cost around half the price of MRI machines. Furthermore, ultrasound is the most commonly used non-destructive method because of its high penetration depth. A lot of small ultrasound transducers are available now which allows us to use them for small-scale applications [24] [25].

The parameters used to analyze standard ultrasound waves are amplitude and time of flight (TOF) information [23]. Ultrasound analysis is performed in two methods- pulse-echo and pitch-catch configuration. In the pulse-echo configuration shown in Fig.2(a), the material is placed between an ultrasonic transducer and a reflector. The transducer creates an ultrasonic pulse that travels through the material. The wave gets reflected on the transducer after hitting the reflector (bottom edge) or any flaws. If the sound beam returns while being reflected any flaws, then it can easily be distinguished by the foreknowledge of sound velocity. In the through transmission (pitch-catch) process shown in Fig.2(b), instead of using one transducer the sample is placed between two transducers. One transducer is used to create the wave and another one is used to receive the wave. In this method, the principle of understanding the flaw position is also the same. However, using conventional ultrasound has some limitations. The parameters, amplitude, and TOF information can only provide information of the position of the flaw but it does not provide any idea of the actual internal structure of the material [8][26]. Also, it requires the presence of a skilled operator to correctly assess the pulse parameter [16]. Studies had been conducted to overcome these limitations that led the research towards Quantitative Ultrasound (QUS).
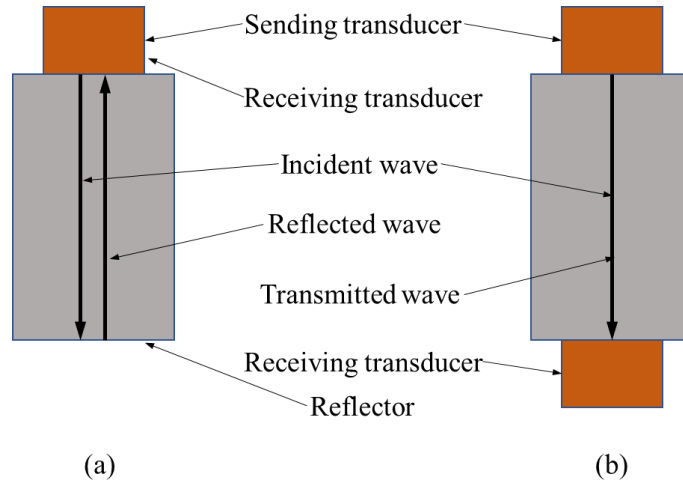
Fig.2   Diagram of (a) Pulse-echo and (b) Pitch-catch ultrasound analysis setup

As a tissue characterization technique, QUS can differentiate between abnormal and healthy tissues. It can also detect the change in tissue properties by relating them to different parameters of the system which fluctuates with varying properties [24], [26], [27]. Most of the studies on QUS were done based on the backscattered RF spectrum acquired from the pulse-echo technique. The parameters developed from analyzing the amplitude of the RF signal are nonlinearity parameter [28], and speed of sound [26], [29]. Furthermore, the power spectrum of the RF signals provide frequency-dependent parameters like backscatter coefficient [30], [31], spectral slope [32]–[34], spectral intercept [33], effective scatterer diameter [35], and integrated backscatter coefficient [29], [36], [37]. Both the amplitude and frequency-based spectral analysis can be utilized in the case of parameters like absorption and attenuation coefficient [29], [38], [39]. The application of the QUS includes monitoring cell decay [34], [40], analyze cardiac irregularities [41], characterizing tumors [26], [42].

7

Based on the frequency range, the ultrasound can be classified into two categories- low-frequency (< 10 MHz) and high-frequency (> 10 MHz) ultrasound. Because of the high frequency, the wavelength becomes smaller which provides better axial resolution compared to the low-frequency ultrasound [43]. Furthermore, high frequency possesses a better lateral resolution in the far-field since it diverges less compared to low-frequency ultrasound [43]. Since ultrasound attenuation is directly proportional to frequency, in contrast to having a better resolution in two directions, high-frequency ultrasound possesses low penetration depth compared to low-frequency ultrasound. In the case of backscatter spectra, high-frequency ultrasound provides an increased number of backscatter coefficients [44]. Therefore, high-frequency ultrasound can be a very effective tool of material characterization in the case of small-scale depth applications. So far high-frequency ultrasound has been applied in medical fields like dermatology [45], [46], cardiology [47], [48] and ophthalmology [49], [50].

Doyle *et al.* worked with different parameters of quantitative high-frequency ultrasound to evaluate tissue microstructure which are sound speed, attenuation measurement, spectrum, and cepstrum [51][52]. It was established that among all these parameters, peak density and slope of the Fourier transform of the ultrasonic spectra showed a large variation in different types of tissue microstructures [53] [54].

1.2.2   Peak Density

This paragraph will discuss the QUS parameter- peak density in detail. The parameter peak density coined by Doyle et al. is the number of peaks and valleys present in the frequency spectrum of an ultrasound signal. Fig.3 shows the peak density from two sample spectrums

while the left spectrum contains less peak density compared to the right spectrum. Since peak density is the summation of the local highest and lowest points in a spectrum, they can be achieved by taking the derivative of the spectrum with respect to the frequency. The number of times the first derivative spectrum will cross the zero frequency will be the amount of peak density presented in that spectrum. In this research, peak density has been analyzed comprehensively to characterize different types of material microstructure in terms of peak density values. The next chapters will discuss the relationship between multiple scattering and peak density. Furthermore, it will discuss the effect of the microstructural change on multiple scattering and how that level of multiple scattering can be established in terms of the peak density presented in the corresponding scattered spectrum.
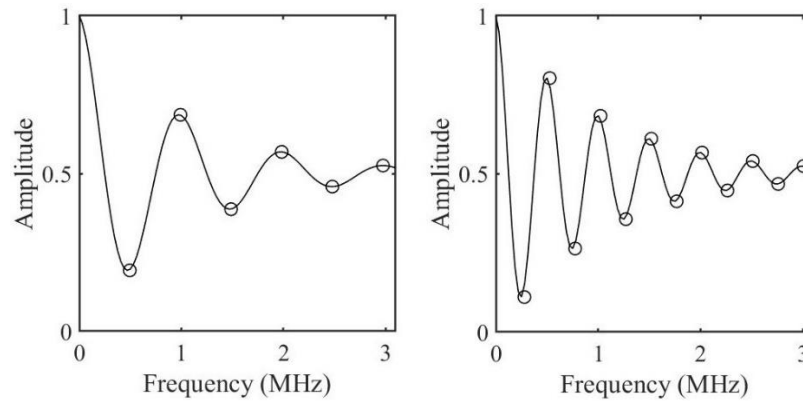
Fig.3   Peak density of sample frequency spectrum indicated by the circles

Although derivatives of the frequency spectrum, can calculate the peak density, it was observed that to find out the significant relationship between peak density and microstructural variation or scattering level, sometimes it is necessary to ignore minor fluctuations in the frequency spectrum i.e. small peaks and valleys. To be able to efficiently

9

eliminate those small peaks and valleys, Stromer et al. established an algorithm (Fig.4) to find the local extrema in a frequency spectrum while including a threshold criterion in that spectrum [55]. This threshold criterion is capable of eliminating small peaks from the spectrum. And when the threshold is set to zero, the algorithm counts all the peaks that can also be measured by taking the derivative of the spectrum.
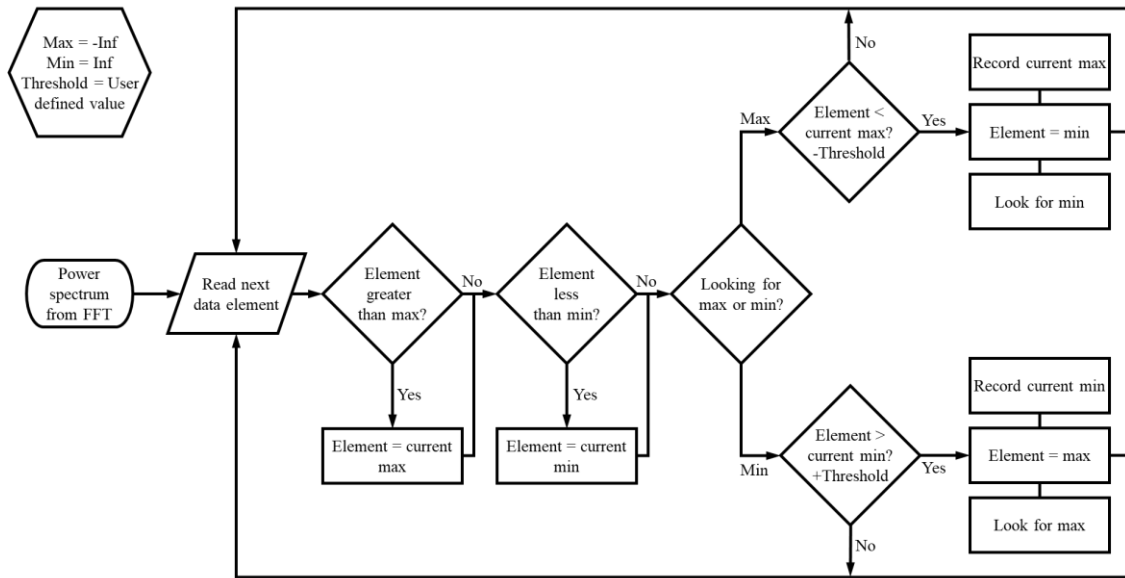
Fig.4   Peak counting algorithm with the threshold criterion

1.2.3   Ultrasound Analysis of Breast Cancer

Breast cancer or breast carcinoma is an uncontrolled growth of epithelial cells in the breast [5]. Each time cells divide inside normal breast ducts or lobules there is a chance of genetic mutation causing uncontrolled growth of cells resulting in tumor formation [5]. To histologically model the breast tumor, it is very important to know the difference between the tumor tissue and normal tissue. It is understood that the presence of abnormally high-dense tissue in the breast lobule may be a good indicator of a tumor [56]. This higher

density normally occurs through an increasing percentage of the fibro glandular tissue in the breast [57]. Pathologists use a grading system to specify the aggressiveness of tumor cells. The grading system consists of three factors: (1) percentage of cancer cells formed into tubules, (2) difference in the nuclei size between healthy and malignant cells (nuclear pleomorphism), and (3) rate of cancerous cell division. Based on these factors, pathologists divide the tumor into three grades where the higher the grade, the larger the difference in histological structures between cancerous and normal tissue.

Different types of analysis were conducted to investigate the relationship between histological features and ultrasound parameters. Empirical analysis showed a strong correlation between histological changes in properly characterized tissues and ultrasound scattering [58], [59]. In the case of experimental outcomes, empirical models were only relevant for homogenous tissues [33]. For the analytical analysis, ultrasound scattering was averaged from the uniform distribution of cells which simplified the acoustic scattering [60]. Therefore, the effect of structural heterogeneity, wave-mode conversion, and multiple scattering was ignored in analytical analysis. To overcome these issues, iterative multipole simulation models were developed to accurately evaluate the ultrasound analysis parameters to detect the changes in histological features [61], [62]. In these studies, histological features like the size of the cell and nucleus were evaluated. These simulation models successfully evaluated multiple ultrasonic scattering in complex histological structures while taking wave mode propagation into account. But the studies did not include viscoelasticity, and the cellular shape could have been more histologically accurate. The multiple scattering was also limited to a range of cells. Furthermore, the transducer properties could also be closely approximated in the numerical models.

Backscattered ultrasound measurements were mostly evaluated in the above-mentioned studies [60], [62]–[64]. Thus, the potential of the forward scattering for histology-based evaluation is yet to be explored. In the case of evaluating backward scattering, the pulse-echo mode of ultrasound analysis was used wherein the case of the forward scattering, pitch-catch, or through transmission ultrasound analysis mode was applied [65]–[67]. During ultrasound propagation through the medium, acoustic scattering is a very important factor controlling the response parameters. When the acoustic wave collides with another medium with different sound velocities, it scatters in different directions depending on the wavelength and medium structure size [66]. Based on the number of structures on the acoustic propagation path, there could be either single or multiple acoustic scattering [62]. At the microscopic histological level, multiple scattering occurs at two different levels. Firstly, the scattered wave from numerous cells causes one level of multiple scattering. Secondly, scattered waves from the different intra-cellular interfaces (ECM-cytoplasm, and cytoplasm-nucleus) inside a cell can cause another level of multiple scattering [62]. Based on the frequency range, acoustic wave scattering can also be categorized into different levels [68]. In the case of breast tissue, multiple scattering was found very significant for the frequencies at approximately 4 MHz [69]. In that frequency level, diffuse ultrasound scattering occurs where the scattered wave goes in all directions with equal magnitude. But at the high-frequency level, diffractive scattering occurs where wave scatters in all directions with different amplitude [65]. It was found that in diffractive scattering, the ultrasound response parameters are strongly dependent on structure size, numbers, and propagation path [70].

In the area of Breast-Conserving Surgery (BCS), although ultrasound-guided excision was found effective (decreasing positive margin rate) for palpable tumors, it was not conclusively recommended for the impalpable tumors [71]. Ultrasound imaging was used intraoperatively to evaluate the lumpectomy lesion [72]–[75]. But it was found that ultrasound imaging was not as effective as other intraoperative pathologic technologies stated above [76].

1.2.4 Ultrasound Imaging in Tissue Characterization

Ultrasound analysis is mostly used as an imaging tool in the medical field due to its availability, cost-effectiveness, and safe usage (no ionizing radiation) [65]. It has the potential of having several centimeters of penetration depth, depending on the frequency range used [77]. Three types of scanning modes are available in ultrasound imaging which are A-scan, B-scan, and C-scan. The A-scan mode works one-dimensionally, only providing amplitude data of the returning echoes from various reflectors situated along the wave propagation direction. On the other hand, the B-scan and C-scan modes provide a two-dimensional image of the plane parallel and perpendicular to the wave direction, respectively [26].

In the medical sector, B-scan imaging is widely used for diagnostic purposes. B-scan ultrasound imaging was used for detecting the abnormalities in dense breasts. To identify the breast duct pathology, high-frequency ultrasound (4-14 MHz) was used to increase the resolution of the B-scan image [78]–[82]. The imaging process only uses the RF signal envelope [65]. It fails to provide quantitative measurement related to biological and structural attributes for characterization [32], [83]–[85]. The only quantitative ultrasound

parameter that was found for this application was using the elastographic grey-scale patterns [79]. But since no correlation was found between histological pattern (nuclear grade) and strain pattern, ultrasound elastography was not recommended for the diagnostic purpose [79].

The image quality in the C-scan mode highly depends on the lateral resolution of the ultrasound since the imaging plane is perpendicular to the wave direction. Therefore, the element size used in the ultrasound transducer, as well as the focusing ability of transducer crystal, play heavily in determining the image quality in C-scan mode. Additionally, the frequency level also plays an important role in the image resolution since the high-frequency ultrasound beam diverges slowly which makes the beam diameter smaller in the far zone [43]. Furthermore, during image reconstruction, parameter measurement inaccuracies can result in low image quality (e.g., poor edge detection) for which fuzzy pre-processing procedures are applied [86], [87]. Both pulse-echo and pitch-catch techniques were evaluated to produce C-scan images in ultrasonic measurements [88]. Pitch-catch methods are mostly used in industrial applications whereas pulse-echo techniques have been adopted in medical applications [88]–[97].

In the industrial sector, C-scan images can provide very high-resolution subsurface images that can evaluate defect size, delamination, and welding quality [90], [91], [96]. In the medical sector, by utilizing QUS, a C-scan image can potentially characterize various tissue properties [65], [98]. For example, in the ophthalmology field, by measuring the ultrasonic backscatter properties, C-scan imaging was used to evaluate eye tissue structures [94]. Various ultrasound parameters of the C-scan method have been evaluated so far.

Standard parameters like amplitude, time of flight, and quantitative parameters like attenuation, and spectral intensity have been utilized in C-scan imaging [55], [88], [90]. Some non-conventional parameters have also been investigated to improve the image quality further in terms of precise detection [55]. One of those parameters is spectral peak density. It was evaluated by Stromer et al. where it was compared against standard ultrasound parameters [55]. Peak density showed similar, and in some cases, better performance compared to the other parameters, however, the quality of the image was dependent on the application through an intuitive threshold magnitude criterion [55].

1.3   Objectives

This research was initially inspired by the development of an instantaneous intraoperative margin detection process. But the scope of this research is not limited to its implementation in medical applications. The goal of this research is to perform an in-depth analysis of quantitative ultrasound physics at a high-frequency level to establish its application in breast cancer treatment. Standard ultrasound parameters available in medical application mostly provides insight into the structure position and shape. Some of the quantitative ultrasound (QUS) parameters have shown promise to offer more detailed information about the structure's physical and mechanical properties. Some additional QUS parameters have shown their effectiveness in material characterization but unfortunately not been researched in depth. Furthermore, most of the applications of ultrasound use the pulse-echo mode. But at the high-frequency level, ultrasound attenuates faster while propagating through the material making the pulse-echo method less advantageous since the wave must travel a distance twice the depth of the material. Therefore, the through-transmission or pitch-catch method can be promising in the use of high-frequency ultrasound apart from

15

the usage of two transducers instead of one because of its enhanced resolution at the micron level. Therefore, the work presented here will address all these shortcomings by incorporating a high-frequency QUS ultrasound analysis by the through-transmission method. One of the QUS parameters, peak density showed a lot of promise while being very sensitive towards materials microstructure. Unfortunately, to the author's knowledge, only one research group had worked with this parameter in material characterization. As a result, this research has conducted an ultrasound analysis using peak density as the QUS parameter. In this study, peak density has been evaluated comprehensively from the ultrasound physics aspect to understand its sensitivity towards various microstructural parameters. To enhance the understanding of this parameter finite element models have been developed and studied to study its feasibility in the imaging application. Furthermore, the finite element study has been implemented to understand the feasibility of QUS to evaluate cellular level inhomogeneity of breast tumors. Finally, a similar analysis has been utilized to detect specific types of carcinomas in surgical margin tissue of breast tumors.

1.4 Research Outline

Chapter 2 discusses the underlying physics of acoustic waves. First, it explains different modes of acoustic wave propagation. Then the discussion delineates different types of acoustic scattering depending on the ultrasound frequency and structure size. In the end, the chapter detailed insight regarding acoustic scattering from a single scatterer while propagating through solid and fluid.

Chapter 3 includes a comprehensive study on high-frequency ultrasound analysis while evaluating peak density for variation in several microstructural features. This includes an

analytical measurement of peak density from the single scattering of the ultrasound wave. Later, the chapter describes a computational analysis of multiple scattering of ultrasound in different microstructural arrangements while measuring peak density for every analysis. Then it explains the relationship between peak density and multiple scattering. Furthermore, it includes the effect of ultrasound attenuation on peak density. Lastly, the chapter concludes with experimental validation of the above studies which includes statistical analysis to measure the level of significance of different microstructural parameters on peak density.

Chapter 4 delineates the finite element modeling of ultrasound C-scan imaging of soft material structures. It also includes the computational study on detecting microstructure position through MPVD of high-frequency ultrasound in a fluid medium.

Chapter 5 describes the study of various tumor grades detection through high-frequency quantitative ultrasound analysis. This includes a computational modeling cell-based tumor with various histological features. Ultrasound peak density and MPVD parameters associated with the frequency spectrums of different tumor grades were compared in this study.

Chapter 6 presents a quantitative ultrasound analysis study of computational modeling of surgical margin analysis of breast tumors. This study is focused on detecting the ductal malignancies in breast tissue. The breast pathologies include normal breast duct, ductal hyperplasia, ductal carcinoma in-situ, benign and malignant calcifications.

Finally, chapter 7 concludes the current study with recommendations for some potential research ideas based on the current research. The future recommendation includes

experimental ultrasound analysis of soft tissues with varying pathology. It also includes analyzing the ultrasound parameters for different characteristics of the transducer. Furthermore, it recommends evaluating the current ultrasound parameters in the field of photoacoustic imaging and hard material characterization.

CHAPTER 2

ACOUSTIC PHYSICS

This section will discuss the basics of acoustic wave propagation and different level of acoustic scattering. In the end, it will describe the scattering theory and analyze the peak density from the theory for different scattering criteria.

2.1 Acoustic Wave Propagation

Sound is mechanical radiant energy that travels as longitudinal or compressional wave (in solid and fluid) and transverse or shear wave (in solid). It generates through the vibration of the particle in certain directions inside a medium (Fig.5). The general properties of a sound wave are frequency (f), wavelength (λ), and velocity (v) which are related as $v = f\lambda$. Since sound travels as single mode of wave propagation in fluid compared to multiple modes of wave propagation in solid, analyzing acoustics in the fluid is easier compared to the solid. In this study, both forms of acoustic wave propagation were evaluated. The theory of acoustics wave propagation in solid and fluid are discussed below.
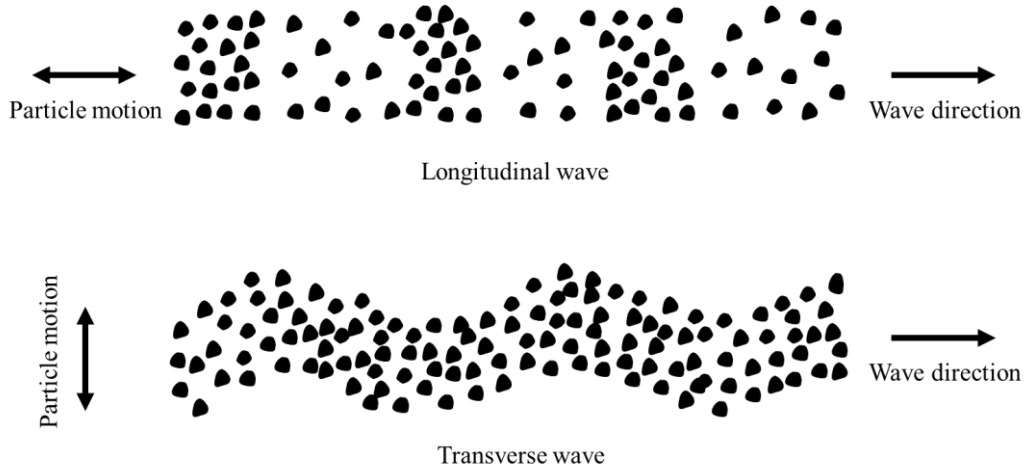
Fig.5   Diagram of different wave propagation

In solid, the propagation of sound is expressed by particle displacement which is governed by Navier's equation. For a linear and homogeneous material, Navier's equation is the following

$$\rho \frac{\partial^2 \boldsymbol{u}}{\partial t^2} = (\lambda + 2\mu)\nabla(\nabla.\boldsymbol{u}) - \mu\nabla \times (\nabla \times \boldsymbol{u}) \qquad (2.1)$$

Here, $\boldsymbol{u}$ is the displacement vector, ρ is solid density, and μ and λ are Lamé constants expressing the solid's mechanical properties. The displacement vector, $\boldsymbol{u}$ consists of a shear component, $\boldsymbol{u_S}$ as well as a longitudinal component, $\boldsymbol{u_L}$ [99], [100]. Furthermore, these longitudinal and shear components can be described as a gradient of the scalar displacement ($\nabla \times \boldsymbol{u_L} \ is \ zero$) and curl of the displacement vector ($\nabla.\boldsymbol{u_S} \ is \ zero$).

20

Therefore, the Navier's equation in terms with longitudinal and shear wave breaks down into the following two equation.

$$\rho \frac{\partial^2 \boldsymbol{u_L}}{\partial t^2} = (\lambda + 2\mu)\nabla(\nabla.\boldsymbol{u_L}) \qquad (2.2)$$

$$\rho \frac{\partial^2 \boldsymbol{u_S}}{\partial t^2} = -\mu\nabla \times (\nabla \times \boldsymbol{u_S}) \qquad (2.3)$$

The above two equations can be further simplified through the following vector identity relation $[\nabla \times (\nabla \times \boldsymbol{u}) = \nabla(\nabla.\boldsymbol{u}) - \nabla^2\boldsymbol{u}]$ showing below

$$\rho \frac{\partial^2 \boldsymbol{u_L}}{\partial t^2} = (\lambda + 2\mu)\nabla^2\boldsymbol{u_L} \qquad (2.4)$$

$$\rho \frac{\partial^2 \boldsymbol{u_S}}{\partial t^2} = \mu\nabla^2\boldsymbol{u_S} \qquad (2.5)$$

In case of static problem, the above equations yield as Laplace equation ($\nabla^2\boldsymbol{u_L} = \nabla^2\boldsymbol{u_S} = 0$)

But in the case of steady-state time dependence (purely sinusoidal), the equations can be simplified by considering displacement components as

$$\boldsymbol{u}(k,t) = \boldsymbol{u}(k)e^{-i\omega t} \qquad (2.6)$$

where $\omega = 2\pi f$ and $k = \frac{2\pi f}{c}$, is the wavenumber, and t is time.

The modified Navier's equations for both components simplify into the Helmholtz equation are given below.

$$\left(\nabla^2 + k_L{}^2\right)\boldsymbol{u_L} = 0 \tag{2.7}$$

$$\left(\nabla^2 + k_S{}^2\right)\boldsymbol{u_S} = 0 \tag{2.8}$$

Here k_L and k_S are longitudinal and shear wavenumber, respectively.

In fluid, the acoustic propagation is expressed in terms with the pressure field (p) inside the medium through the following equation

$$\rho c^2 \nabla \left(\frac{1}{\rho}\nabla p\right) - \rho\frac{\partial^2 p}{\partial t^2} = 0 \tag{2.9}$$

Here, ρ is the fluid density, c is wave speed.

Similar to the case of wave propagation in solids, the pressure field can be assumed as stationery and harmonic with frequency f.

$$p(f,t) = p(f)e^{-i\omega t} \tag{2.10}$$

From the above two equations, the simplified waveform becomes

$$\rho\nabla\left(\frac{1}{\rho}\nabla p(f)\right) - \left(\frac{2\pi f}{c}\right)^2 p(f) = 0 \tag{2.11}$$

By introducing the wavenumber k in the equation and considering the fluid as incompressible, the equation further simplifies into a generalized Helmholtz equation.

$$(\nabla^2 + k^2)p = 0 \tag{2.12}$$

Both wave propagation phenomena explained above will be used throughout this research.

2.2 Acoustic Scattering

While propagating through a medium, if the wave interacts with a change in medium property or simply if the wave faces an object in its path, some energy gets absorbed and some get reradiated from the interface [101]. This reradiated wave creates acoustic scattering. Depending on the wavelength of the incident wave and the size of the structure which deflects the wave from its surface, the acoustic scattering can be divided into three categories. The parameter used to define these different types of scattering is ka, where k is the wavenumber and a is the size of the scatterer or the object which is causing the scattering.

When $ka \gg 1$ i.e. the wavelength of the incident wave is much larger compared to the scatterer size, a certain amount of incident energy gets transmitted through the object and the rest of the energy gets reflected from the interface of the medium and the object [102]. This is known as specular scattering shown in Fig.6(a). The fraction of transmitted intensity (ITC) and reflected intensity (IRC) shown in the following equations depend on the

variation in properties such as density (ρ) and wave speed (c) between two mediums [103]. These properties are defined as impedance (Z), where $Z = \rho c$.

$$IRC = \left[\frac{(Z_2 - Z_1)}{(Z_2 + Z_1)}\right]^2 \tag{2.12}$$

$$ITC = 1 - IRC = \frac{4Z_2 Z_1}{(Z_2 + Z_1)^2} \tag{2.13}$$

Here Z_1 and Z_2 are the impedance of the initial propagation medium and the scattering object, respectively.
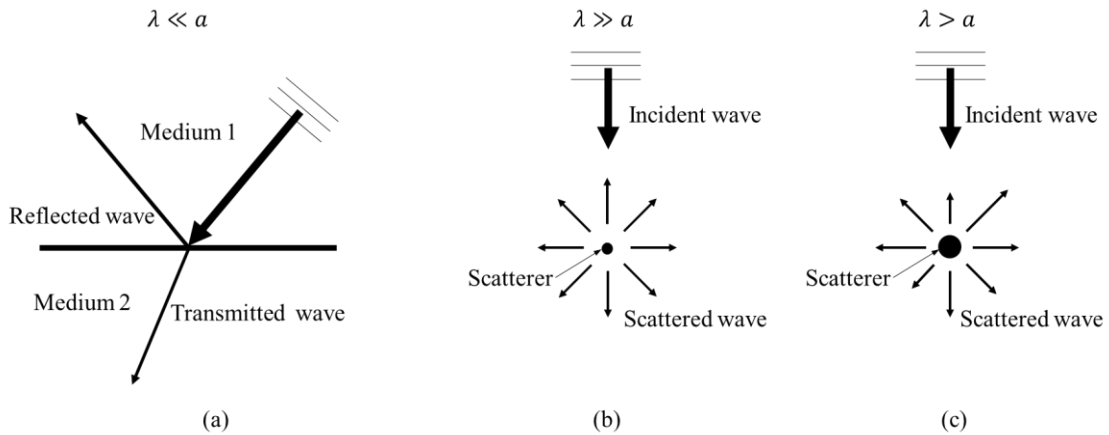
Fig.6　(a) Specular scattering, (b)Diffuse scattering, and (c) Diffractive scattering

When $ka \ll 1$, the scattering is known as diffuse, or Raleigh scattering is shown in Fig.6(b). In this case, the wave from the surface of the object scatters equally in all directions. The level of scattering is proportional to the fourth power of the incident wave frequency.

The third scattering regime is known as diffractive scattering shown in Fig.6(c) where the wavelength is bigger or in the order of the scatterer size ($i.e. ka \lesssim 1$) [26]. The scattering mechanism in this region is complicated the wave gets scattered in all directions with various intensities. Since this study mostly focuses on high-frequency ultrasound analysis, the scattering mostly falls in the diffractive scattering regime.

Depending on the number of objects in a wave propagation medium as well as impedance mismatch between mediums, the scattering can be further divided into two categories-single scattering, and multiple scattering. Single scattering occurs when there is only one object inside a medium or the impedance mismatch only occurs for a single time. Therefore, the scattered wave does not get to interact further on the way of propagation. In contrast, multiple scattering occurs when there are multiple objects present inside a medium. In that case, the scattered wave from one object can again behave as an incident wave in the case of another object situating in its way of propagation. Furthermore, multiple scattering can also occur with a single object if there are different layers with various impedance variations inside the object. In that case, the multiple scattering occurs inside the object while it propagates through different layers. Therefore, the level of scattering does not depend on the number of objects present along the way of propagation but the number of surfaces with different impedances. Single scattering is only used to develop a theoretical model since the scattering level is simple to solve. Sometimes multiple scattering problems are simplified assuming single scattering from the different surfaces to keep the analysis simpler. But in reality, multiple scattering occurs in most of the acoustic scattering scenarios. In this thesis, both single and multiple scattering was evaluated by numerical and experimental analyses. The next section will describe different

scattering models and one of the single scattering models applications in terms of peak density.

2.3 Single Diffractive Scattering

This section will discuss the single scattering model developed by Faran and Hickling [104], [105]. In this model, the scatterers are considered as solid spheres immersed in a fluid medium. Therefore, there is no shear wave propagation in the medium i.e., the wave mode conversion is neglected. For the simplicity of the calculation, only a single scattering will be evaluated. The incident wave (P_i) is considered as plane wave traveling through the medium which is expressed by the following equation.

$$P_i = P_o e^{-ik(x-ct)} = P_o e^{-ik(rcos\theta - ct)} \tag{2.14}$$

P_o is incident pressure amplitude, k is the wavenumber, c is wave speed, t is time, r and θ correspond to the usual polar coordinates. The time component is ignored by assuming a time-harmonic wave to simplify the problem. It is convenient to express the incident plane wave as plane wave expansion because of the spherical nature of the scattered wave.

$$P_i = P_o \sum_{l=0}^{\infty}(2l+1)i^l j_l(kr)P_l(cos\theta) \tag{2.15}$$

Here, j_l is spherical Bessel function of the second kind and P_l is Legendre polynomial respectively, k is the wavenumber, r and θ correspond to the polar coordinate.

26

In this model, the scatterer is considered elastic. Therefore, the shear and compressional waves are considered to measure the scattered wave pressure. The boundary conditions in the fluid-solid interface take into account the wave propagation in solid governed by Navier's equation showed in Eq. (2.1).

So, the boundary conditions were (1) the fluid pressure Incident (P_i) and scattered (P_s) pressure fields to be equal to normal stress component of solid, (2) normal displacements in the fluid and solid are equal and (3) the shear stress to be zero which are shown through the following equation:

$$P_i + P_s = -T_{rr} \tag{2.16}$$

$$u_{i,r} + u_{s,r} = -u_{solid,r} \tag{2.17}$$

$$T_{r\theta} + T_{r\Phi} = 0 \tag{2.18}$$

Here T_{rr}, $T_{r\theta}$, and $T_{r\Phi}$ are the stress tensors of the solid respectively and $u_{i,r}$ and $u_{s,r}$ normal displacement components (incident and scattered respectively) of fluid and $-u_{solid,r}$ is the normal displacement component of the solid in the spherical coordinates respectively.

After sound scattering, the scattered pressure (P_s) wave can be expressed as,

$$P_s = -P_o \sum_{l=0}^{\infty} (2l + 1)(-i)^{l+1} sin\eta_l e^{i\eta_l} h_l^{(2)}(kr) P_l(cos\theta) \qquad (2.19)$$

Since the focus was on pitch-catch mode, at the far-field $(r \to \infty)$ sound pressure of the scattered field is described as,

$$P_{s,far} = -\frac{P_o}{k_3 r} \sum_{l=0}^{\infty} (2l + 1) sin\eta_l e^{-ikr} P_l(cos\theta) \qquad (2.20)$$

Here, η_l is the scattering phase angle of lth wave due to scatterer properties, $h_l^{(2)}$ is the Hankel function. The phase shift angle was expressed as,

$$\eta_l = tan^{-1}\left[\frac{tan(\delta_l(k_3 a))(tan\Phi_l + tan\alpha_l(k_3 a))}{tan\Phi_l + tan(\beta_l(k_3 a))}\right] \qquad (2.21)$$

Where,

$$tan\alpha_l(k_3 a) = -\frac{(k_3 a)j_l'(k_3 a)}{j_l(k_3 a)} \qquad (2.22)$$

$$tan\beta_l(k_3 a) = -\frac{n_l'(k_3 a)}{n_l(k_3 a)} \qquad (2.23)$$

$$tan\delta_l(k_3 a) = -\frac{j_l(k_3 a)}{n_l(k_3 a)} \qquad (2.24)$$

$$\tan \Phi_l = -\frac{\rho_3}{\rho_1} \tan \xi \,(ka, v) \tag{2.25}$$

$$\tan \xi \,(ka, v) =$$

$$\left[-\frac{(k_2 a)^2}{2} \frac{\dfrac{(k_1 a)j_l'(k_1 a)}{(k_1 a)j_l'(k_1 a) - j_l(k_1 a)} - \dfrac{2(l^2 + l)j_l(k_2 a)}{(l^2 + l - 2)j_l(k_2 a) + (k_2 a)^2 j_l''(k_2 a)}}{\dfrac{(k_1 a)^2 \left[\left(\dfrac{v}{1 - 2v}\right)j_l(k_1 a) - j_l''(k_1 a)\right]}{(k_1 a)j_l'(k_1 a) - j_l(k_1 a)} - \dfrac{2(l^2 + l)[j_l(k_2 a) - k_2 a j_l'(k_2 a)]}{(l^2 + l - 2)j_l(k_2 a) + (k_2 a)^2}}\right] \tag{2.26}$$

α_l, β_l, δ_l, ξ are the scattering phase angle, Φ_l is boundary impedance scattering phase-angle, v is Poisson's ratio, j_l and n_l are spherical Bessel functions of a first and second kind respectively, ρ_1 and ρ_3 are the density of the scatterer and surrounding fluid respectively, $k_1 a$, $k_2 a$, and $k_3 a$ are the wavenumbers corresponding to compressional wave in scatterer, shear wave in scatterer, and sound wave in the surrounding medium respectively, where $k = c/\lambda$ and c is velocity and λ is the wavelength, a is the scatterer diameter and r is the far-field distance from the center of the scatterer.

Two of the simplification of this case is the sphere can be modeled as either a hard or soft scatterer. In the case of the hard or rigid sphere, a Neumann boundary condition showed in Eq. (2.27) and in that case, the phase shift is shown in Eq. (2.28).

$$\frac{\partial p_i}{\partial r} - \frac{\partial p_s}{\partial r} = 0 \tag{2.27}$$

29

$$sin\eta_l e^{i\eta_l} = \frac{j_l'(ka)}{h_l^{(2)'}(ka)}$$

(2.28)

The far-field$(r \rightarrow \infty)$scattered pressure, in this case, would be

$$P_{s,far} = -P_o \sum_{l=0}^{\infty}(2l+1)(-i)^{l+1}\frac{j_l'(ka)}{h_l^{(2)'}(ka)}i^{l+1}\frac{e^{-ikr}}{r}P_l(cos\theta)$$

(2.29)

In the case of the soft sphere, a Dirichlet boundary condition showed in Eq. (2.30) and in

that case, the phase shift is shown in Eq. (2.31).

$$P_i + P_s = 0$$

(2.30)

$$sin\eta_l e^{i\eta_l} = \frac{j_l(ka)}{h_l^{(2)}(ka)}$$

(2.31)

The far-field$(r \rightarrow \infty)$scattered pressure in the case of the soft sphere would be

$$P_{s,far} = \sum_{l=0}^{\infty}-(2l+1)\frac{j_l(ka)}{h_l^{(2)}(ka)}P_l(cos\theta)$$

(2.32)

30

Results could also be achieved from the elastic solution by taking $\rho_3 \to 0$ (soft sphere) and $\rho_3 \to \infty$ (hard-sphere).

CHAPTER 3

RELATIONSHIP BETWEEN PEAK DENSITY AND ACOUSTIC SCATTERING

This study focuses on developing a relationship between peak density and acoustic scattering, hence peak density in soft tissue phantoms containing hard scatterers and particles. The outcome of this study can also be found in [70]. To relate the effect of different geometrical and microstructural parameters on the scattering and peak density, peak density was measured in different scattering conditions in a pitch-catch method using tissue phantom containing different scatterer sizes and thicknesses. Furthermore, to evaluate spatial distribution impact on the resulting peak density, samples with different scatterer densities were tested. Analytical evaluation and computational calculations were conducted to theoretically relate these parameters. Analytically, the peak density was calculated from Faran and Hickling's single scattering model using a spherical scatterer while varying its diameter [104], [105]. Peak density was also measured from the computational model and experiment while varying the scatterer size, spatial distance (by changing the volume ratio of scatterers), and ultrasound travel distance (by varying the sample thickness). Agarose phantom with glass microspheres was used with 3 different levels of phantom thickness, microsphere size, and number. Two 25 MHz transducers were used to perform the ultrasound analysis in a pitch-catch method. The received scattered signal was transformed using Fast Fourier Transform (FFT) and passed through signal processing steps before the peak density was evaluated.

3.1 Analytical Analysis

For the elastic sphere scenario, the single scattering was evaluated for various scatterer sizes over a certain frequency range. The medium was chosen as water where sound

propagation speed was taken from the soft tissue for better imitation of the soft material environment. The physical parameters are listed in Table 1.

Table 1   Physical parameters used for the analytical model

Parameter	Value
Poisson's ratio (ν)	0.22
Compressional wave speed in scatterer (c_1)	$5770\ m/s$
Shear wave speed in scatterer (c_2)	$3430\ m/s$
Sound wave speed in fluid (c_3)	$1540\ m/s$
Glass density (ρ_1)	$2500\ kg/m^3$
fluid density (ρ_3)	$1000\ kg/m^3$

From Eq. (2.20), the pressure of the scattered ultrasound wave was calculated in the forward direction at different scattering conditions. The scatterer diameter was 10, 40, and 70 μm, and the propagation path distance was 1000 μm. The propagation properties were similar to soft tissue and the wave velocity was 1540 m/s. Pressure amplitude was measured along 18 to 41 MHz frequency range for each scatterer size to achieve the pressure amplitude spectrum which is shown in Fig.7. The total number of peaks and valleys (peak density) in each spectrum was calculated using a peak counting algorithm in MATLAB shown in Fig.4. For 10, 40, and 70 μm spheres, the calculated peak density were 0, 4, and

21. From Fig.7, it was observed that with the increase of scatterer size the pressure amplitude of the spectrum had been increased. Also, the variability in the spectrum amplitude was increased with the scatterer diameter which indicates the increase in peak density. Therefore, peak density can be defined as a parameter to express the level of scattering.
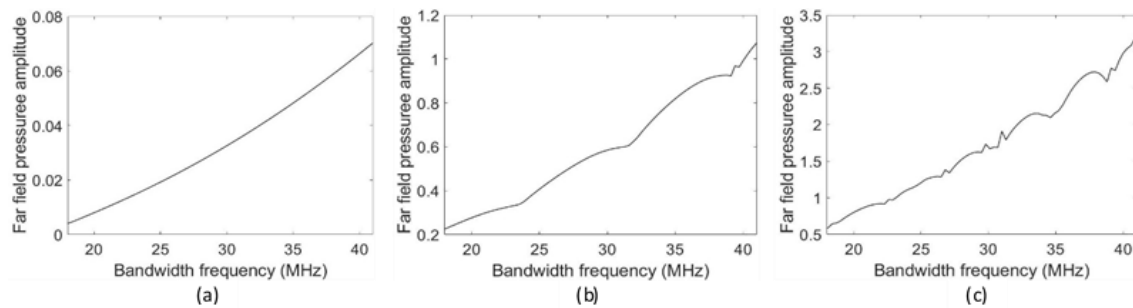
Fig.7   Frequency spectrum for scatterer size of (a) 10 μm, (b) 40 μm and (c) 70 μm

To understand the effect of ultrasound propagation path distance on peak density, the pressure spectrum was achieved from a 70 μm scatterer for a distance of 1000 and 3000 μm and plotted in Fig.8. The far-field distance was measured from the center of the sphere which was half of the total travel path- 500 and 1500 μm. From Fig.8, it was observed that with increasing distance, only the pressure amplitude level changed but the pattern of the pressure amplitude remained the same. Since the wave was going through a single scattering, the scattered wave was not getting interfered with by any other wave in the way. Therefore, increasing travel distance only decreased the amplitude level because of

attenuation but the pattern, as well as the peak density, remained the same. This made the travel distance an inactive parameter during single scattering to evaluate peak density.
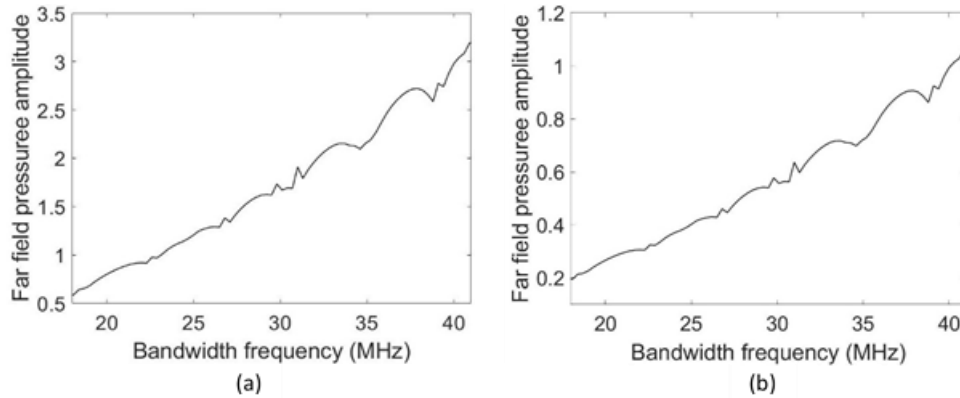
Fig.8   Frequency spectrum for a scatterer of 70 μm diameter at far field of (a) 500 μm

and (b) 1500 μm

3.2   Computation Analysis

Computational analysis is an effective method to understand internal physics while imitating the actual environment [106]. It enables us to mimic different types of DOE with a very minimal investment for the variation. In this current study, computation analysis was conducted to complement the experimental results. Furthermore, it was used to improvise different types of microstructural arrangements to characterize which would be arduous to create experimentally.

The current computation analysis is subdivided into two categories. One includes pure linear elastic wave propagation through various microstructural variations. And the other includes the attenuation of high-frequency ultrasound in the analysis. The goal of the first

35

analysis is to explore the scattering level without any interruption from the medium other than the internal structure. This helps us to understand the relationship between peak density and acoustic scattering from the scattering point of view. The major limitation of the first analysis is that it hinders understanding the limitation of high-frequency ultrasound which is the high attenuation coefficient. Therefore, the second model helps to overcome this limitation to explore the dependency of peak density on acoustic absorption inside the medium.

COMSOL Multiphysics 5.5a was used for the finite element simulation. The ability to solve governing equations in different physics in the same analysis and proper implementation of a boundary condition in the interface of two physics makes this computation tool an effective one. In this case, the partial differential equation in acoustics and solid mechanics was solved through COMSOL.

3.2.1 Linear Elastic Model

The material was designed as solid spheres dispersed in a fluid medium. Therefore, only longitudinal waves were propagated through the fluid medium. In the fluid medium, COMSOL solved the 2D Helmholtz equation for the pressure wave shown in Eq. (3.1).

$$\nabla \cdot \left(-\frac{1}{\rho_c} (\nabla p_t - \boldsymbol{q_d}) \right) - \frac{k_{eq}^2}{\rho_c} p_t = Q_m \tag{3.1}$$

k_{eq} is the equivalent wave number defined for wave velocity c_c in fluid and frequency f shown as,

$$k_{eq}^2 = \frac{(2\pi f)^2}{c_c^2} - k_z^2 = k^2 - k_z^2 \tag{3.2}$$

In this model, the out of plane wave number k_z, monopole and dipole source term Q_m and q_d was set to zero. ρ_c is the fluid density. The total pressure, p_t is the summation of the background pressure field (p_b) and backscatter pressure field (p_s). In the model, the background pressure field was expressed as wave propagation in $\widehat{e_x}$ direction defined as $p_b = p_0 e^{-kx}$. After applying all the adjustments, the modified Helmholtz equation became,

$$\nabla^2 p_t + k^2 p_t = 0 \tag{3.3}$$

In the solid region, the scatterers were modeled as linearly elastic isotropic material for which 2D Navier's equation was solved

$$-(2\pi f)^2 \rho_s \boldsymbol{u} = \nabla . S + \boldsymbol{F} e^{i\phi} \tag{3.4}$$

In this equation, f is sound frequency, S is Cauchy stress tensor, ρ_s is solid density, ϕ is the phase component of the force, $\boldsymbol{F}$ is acting force on solid, and $\boldsymbol{u}$ denotes the solid displacement field.

The equations in the acoustics and solid mechanics were coupled by the following boundary conditions

$$n \cdot \frac{1}{\rho_c} \nabla p_t = -n \cdot u_{tt} \tag{3.5}$$

$$F = p_t n \tag{3.6}$$

n was the normal unit vector to the boundary, u_{tt} was structural acceleration, and F was the acting load on solid, p_t was the total pressure, and ρ_c was the fluid density.

3.2.1.1 Model Description

The computational model consisted of a solid and fluid region. A perfectly matched layer was introduced to perform as a non-reflecting boundary layer to have an uninterrupted wave propagation through the boundary where the wave pressure was recorded. To select the proper mesh size, mesh size was decreased gradually and for each mesh size, peak density was measured. For the mesh size of one-eighth of the wavelength, the peak density result was converged for all the models. Therefore, it was selected as the maximum mesh size for all models. To capture perfect multiple scattering, the scatterers were distributed randomly. The medium layer area was 1x1 mm^2 with 70 µm height where the sound wave would travel 1 mm distance. To get the effect of sample thickness or various travel distances two more models having 1x2 and 1x3 mm^2 layer area was generated. For each of these three models, the number of scatterers used was 1, 5, and 9 per unit (mm) wave travel distance. Also, the scatterer size was selected as 10, 40, and 70 µm. Therefore, a total of 27 models were generated. To mimic a soft tissue medium, the fluid region's density (ρ_c) was kept 1000 kg/m^3 and sound velocity (c_c) was considered as 1540 m/s. Solid structures density (ρ_s) was 2500 kg/m^3, poison ratio (ν) was 0.22, Young's modulus (E_Y)

was 68 GPa and sound speed (c_s) was 5570 m/s. Fig.9 shows a typical computational model geometry used in this analysis having 5 scatterers of 40 µm diameter.
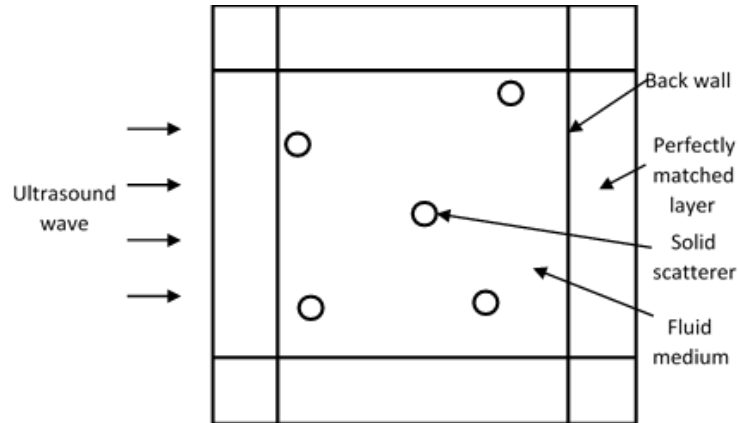
Fig.9   COMSOL model geometry for ultrasound analysis

3.2.1.2   Simulation Parameters

To achieve the frequency spectrum, the frequency was increased by 100 kHz starting from 18 MHz to 41 MHz. For each step frequency, the model calculated scattered pressure. Since the objective was to evaluate pitch-catch wave propagation, the pressure of the forward scattered wave was calculated on the far wall showed in Fig.9. After evaluating the average acoustic pressure on the back wall for each frequency step, it was plotted against the corresponding frequency to achieve the frequency spectrum. In the end, MATLAB was used to evaluate the data for measuring peak density. This procedure was repeated for all 27 models to compute the peak density.

3.2.1.3   Results

Fig.10 depicts the peak density for all the models calculated at each thickness level with varying scatterer sizes and numbers. An increasing trend of peak density was observed with the increase in each parameter. From the analytical study, it was understood that with increasing scatterer size the peak density increased from the single scattering. But when it came to multiple scattering, all the parameters which were thickness, scatterer size, and number contributed towards the multiple scattering to change the peak density. This result made peak density a very sensitive parameter while characterizing a material microstructure from every aspect.
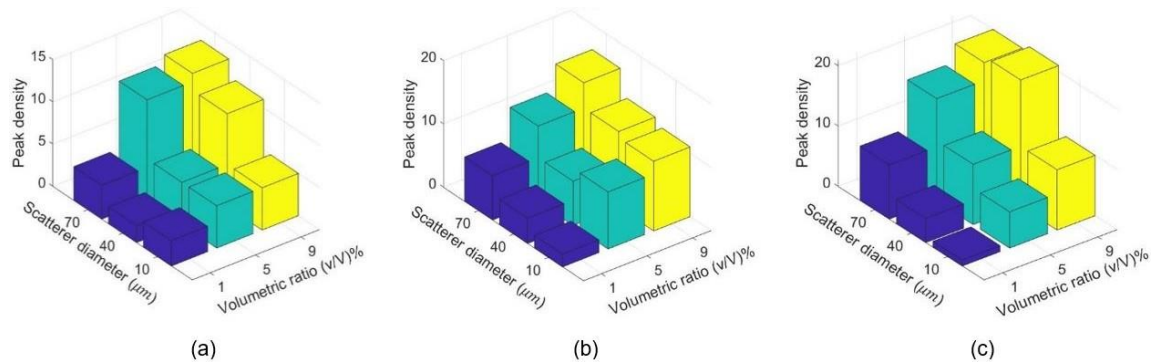
Fig.10 Computational peak density value of linear elastic for different scatterer number

and diameter at wave propagation distance of (a) 1 mm, (b) 2 mm, and (c) 3 mm

With the random distribution of scatterers, an important associated factor came into consideration which was the distance between the scatterers. Since the scatterers were distributed randomly in the medium, the distance among them was not controlled intentionally to support the randomness. But after understanding the sensitivity level of

peak density, it became an essential concern to evaluate the inter-scatterer distance effect on peak density while keeping every other parameter constant. A simple computational model of 1x1 mm² layer area was developed to explore this phenomenon. 9 glass scatterers were placed in a rectangular array inside the fluid region. The scatterer diameter was selected to be 40 µm. The scatterers were placed at an equal distance from each other. 7 models were developed by varying the distance between the scatterer which were 400, 300, 250, 150, 100, and 70 µm. Fig.11 shows two of the models having an inter-scatterer distance of 400 and 70 µm.

(a)   (b)
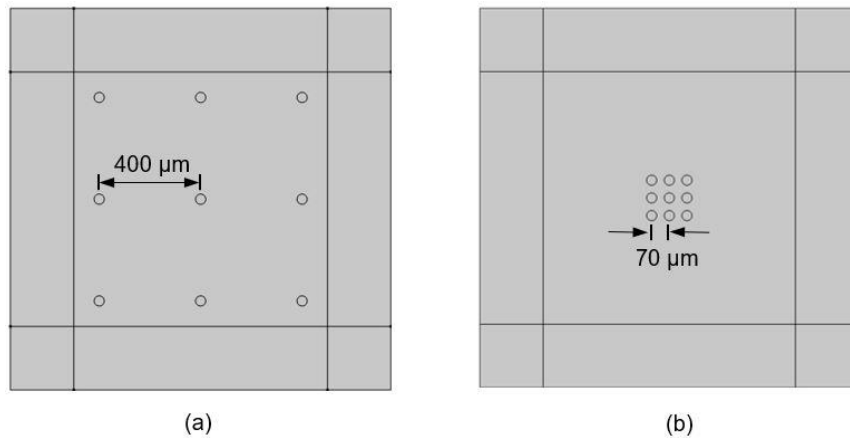
Fig.11 Computational model consisting inter-scatterer distance (a) 400 µm, and (b) 70 µm

Fig.12 showed the peak density plotted against the inter-scatterer distance. It was evident that the distance between the scatterers also played a vital role in the peak density variation. Especially when the distance increased, the scattered wave interfered with each other along the whole way while increasing the amount of scattering. It resulted in higher peak density. This phenomenon gave the peak density an advantage to detect the scatterer orientation during the analysis.

41
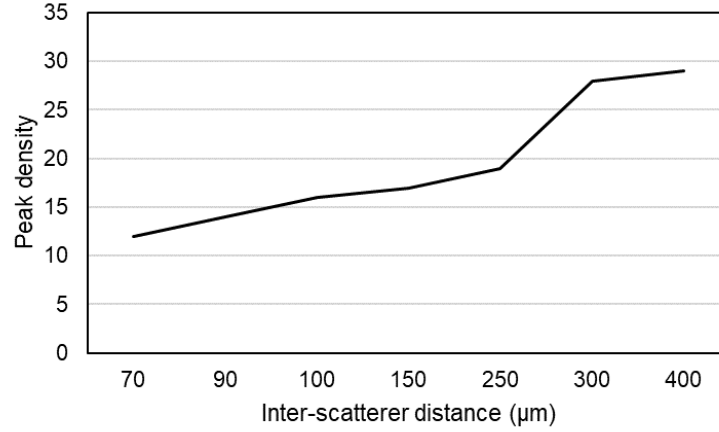
Fig.12 Peak density vs inter-scatterer distance

3.2.2 Linear Elastic Model with Attenuation

Since the peak density showed an increasing trend with increasing thickness, the ultrasound attenuation in high frequency needed to be evaluated. To understand the effect of attenuation on peak density, the attenuation coefficient (α) was introduced to the previous model. In this case, the attenuation coefficient depends on the frequency. Therefore, it affects the wave number shown in the following equation.

$$k_{eq}^2 = \left(\frac{2\pi f}{c_c} - i\ln(10)\frac{\alpha}{20}\right)^2 - k_z^2 \tag{3.7}$$

Since out of plane wave number k_z was zero, therefore, simplified equivalent wavenumber becomes,

$$k_{eq} = \frac{2\pi f}{c_c} - i\ln(10)\frac{\alpha}{20} \tag{3.8}$$

To mimic proper soft tissue environment attenuation coefficient value was chosen as $70\ dB/m$ at 1 MHz frequency.

42

From Fig.13 it is evident that even with attenuation the peak density shows the same trend of the elastic model with creasing scatterer size, scatterer number, and sample thickness. To evaluate whether the ultrasound attenuation affects the peak density to any extent an additional analysis was conducted.
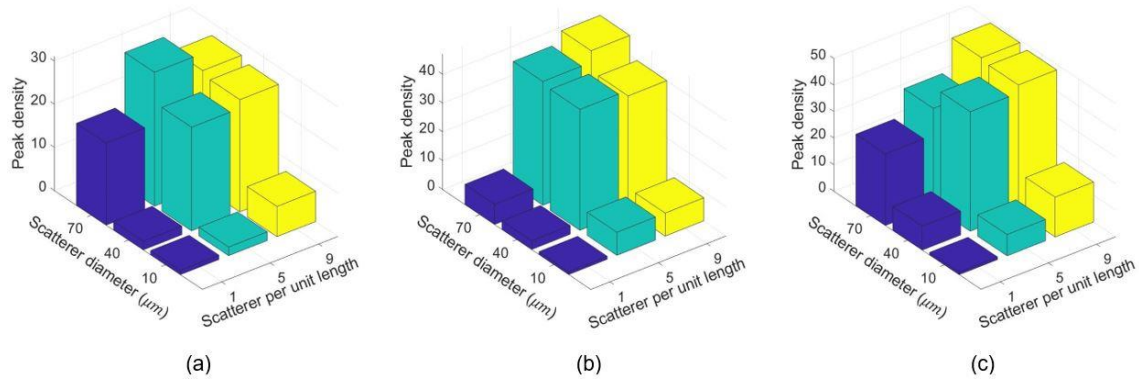
Fig.13 Computational peak density value for different scatterer number and diameter at wave propagation distance of (a) 1 mm, (b) 2 mm, and (c) 3 mm

Two sets of models were simulated. The first set of 9 models had 1, 2, and 3 mm propagation distance with each having a total number of scatterers 1, 5, and 9. The scatterer diameter was kept as 40 μm. The second set of 9 models had 1, 2, and 3 mm propagation distance with each having scatterer diameter 10, 40, and 70 μm. The total number of scatterers in each model was 5. The purpose of these simulations will be explained in detail in the result section.
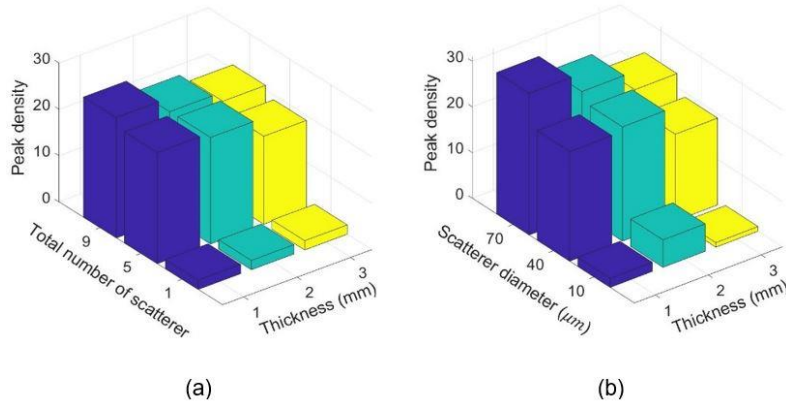
Fig.14 Peak density at increasing thickness with (a) increasing number of scatterers, (b) increasing scatterer size

Fig.14 shows the effect of ultrasound attenuation in multiple scattering as well as peak density. Fig.14a shows that peak density decreases with increasing thickness for the same number of scatterers with a constant diameter. But with the increasing number of scatterers, peak density started to increase in every thickness level. Similar results were found in the case of scatterer size in Fig.14b. Although peak density was decreasing with increasing thickness, it started to increase in each thickness level with increasing scatterer size. This explains that by increasing scatterer number or size, the multiple scattering level increases which result in higher peak density for the same level of attenuation. This validates the increasing trend of peak density along with increasing thickness in Fig.13. Because with increasing thickness, the total scatterer number was increasing since scatterers number were selected per unit thickness. This increasing amount of scatterers overcame the effect of attenuation by increasing the peak density. But ultrasound eventually attenuates faster at high frequency which will limit this peak density trend to a certain thickness level.

3.3 Experimental Analysis

An experimental setup was built to perform ultrasound analysis to evaluate the peak density.

3.3.1 Sample Preparation

The agarose-based phantom was prepared from high-purity agarose, water, n-propanol, evaporated milk, and thimerosal [107]. First, a mixture of agarose, water, and n-propanol was made and heated to 90°C. The weight ratio of those materials was 23:1:2 respectively. Then another mixture of evaporated milk and thimerosal was made and heated at 68°C. The weight ratio was 1.33:800 respectively. After that, both mixtures were added together at 55°C and then solidified. To introduce microstructural variation as well as to enhance the scattering properties of the soft material in terms of acoustic scattering, glass microbeads were inserted inside the sample. To keep similarity with the computational model, three types of glass microbeads of diameter 8-12 µm, 35-45 µm, and 65-75 µm were inserted inside the phantom. Each type of microbeads was mixed with the phantom in three different volumetric ratios- 1%, 5%, and 9% ($V_{microbead}/V_{total}$). Also, three levels of sample thickness were selected which were 1 mm, 2 mm, and 3 mm. Therefore, there were 27 types of phantom generated for the experimental analysis. The image of one of the phantoms with glass scatterers is shown in Fig.15. The image was taken through an optical microscope and a digital camera.
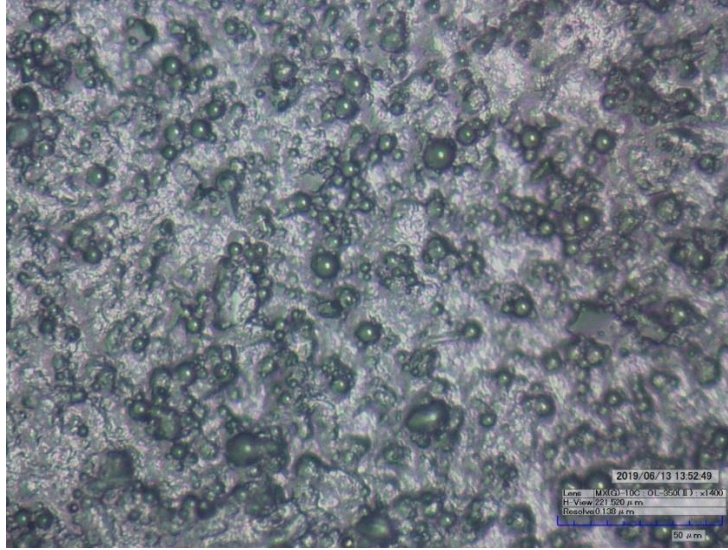
Fig.15 Agarose based phantom with glass microbeads

3.3.2   Experimental Setup

Fig.16 shows the experimental setup which consisted of two ultrasound transducers (25 MHz, 2 mm diameter, TransducerWorks, Centre Hall, PA, USA), a pulser receiver system (UTEX UT 340, UTEX Scientific Instruments Inc. Mississauga, Ontario L5L 1A3, Canada) and a mix-domain oscilloscope (Tektronix MDO 3052, Tektronix, Inc. Beaverton, OR 97077, USA), coupling gel (Aquasonic 100, Walmart INC), a height-adjustable station for phantom and transducer and tissue-mimicking phantom. The coupling gel was used to save the transducers from the damage occurring from the impedance mismatch between the transducer crystal and phantom. Also, the gel ensured less amount of intensity loss of the high-frequency wave along its way from the transducer to the phantom. For the ultrasonic transducers, the -6 dB frequency bandwidth was in the range of 18-41 MHz. The station for transducers and phantom was made in a way that either phantom or any

transducer position could be adjusted by changing the height of the structure. This was done to adjust the setup with different thicknesses of phantoms.
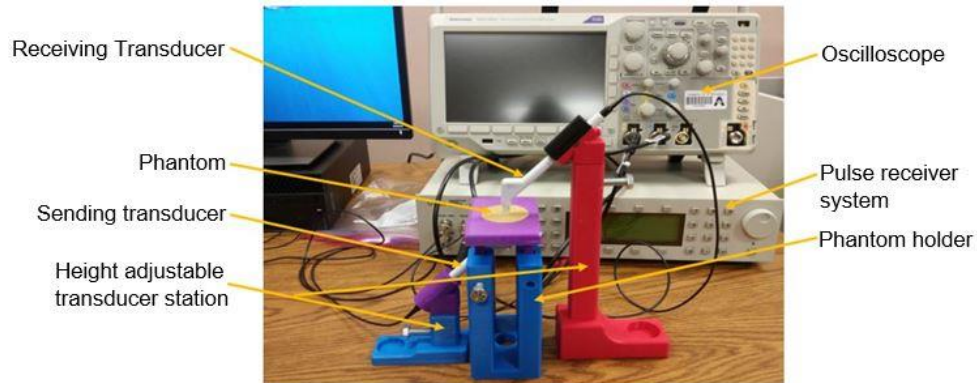
Fig.16 Photograph of ultrasound analysis setup

For each of the phantoms, the ultrasound analysis was conducted in 14 different places to calculate the peak density. The final peak density was then determined from the average of 14 results from each sample.

3.3.3 Data Acquisition

To proceed with the analysis, first, the high-frequency ultrasound signal was sent from the pulse receiver. Table 2 lists all the pulse parameters selected for signal generation. Fig.17 shows the experimental process steps. A pitch-catch technique was used to conduct the ultrasound analysis. Both transducers were aligned on top of each other to ensure proper sound propagation. The ultrasound signal was sent from one transducer which went through the coupling gel, and phantom and then was received by another transducer. The

received signal was again sent to the pulse receiver for further amplification. After that, the

signal was stored in the computer through the oscilloscope for further signal processing

and peak density calculation.
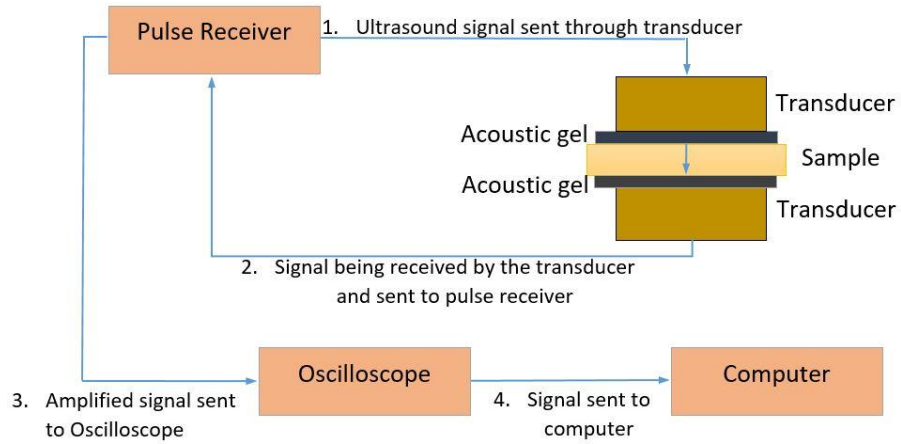
Fig.17 Schematic diagram of the ultrasound analysis process in pith-catch setup

Table 2   Ultrasound parameter

Parameter	Value
Voltage	100 V
P/C Gain	48 dB
Repetition Rate	19 kHz
Pulse Width	20 ns

3.3.4   Signal Processing and Peak Density Evaluation

The time-domain signal was stored in the computer from the oscilloscope and the signal

processing was performed through MATLAB. The first step of the signal processing was

windowing the signal. Stromer et al. showed that the rectangular window performed better

compared to Hamming, Hann, Tukey, and Blackman windowing function while

calculating the peak density [108]. Therefore, a rectangular window was applied to the time

domain signal to capture only the pulse generated by the transducer crystal. The windowed

signal was then transformed from the time domain to the frequency domain through Fast

Fourier Transformation (FFT). To eliminate any possible systemic consequences from the

pulse receiver and transducer, the signal was normalized by a reference signal. To generate

a reference signal, first, the ultrasound was generated in the same pitch-catch setup and

guided through the coupling gel only. The signal then went through all the signal

processing steps stated above. Then the FFT sample signals pressure amplitude was divided

by the pressure amplitude of the reference signal on each frequency step of the frequency

bandwidth to generate the calibrated signal. In the end, the number of peaks was counted

from the calibrated signal between the $18 - 41$ MHz frequency range. This procedure was

repeated for each of the 27 types of samples for 14 times. Fig.18 shows a typical numerical

frequency spectrum (thickness 3 mm and scatterer diameter 70 µm with 9 scatterers per

unit length) and a typical experimental frequency spectrum of a typical sample (thickness

3 mm, scatterer diameter 65-75 µm, and volume fraction 9%).
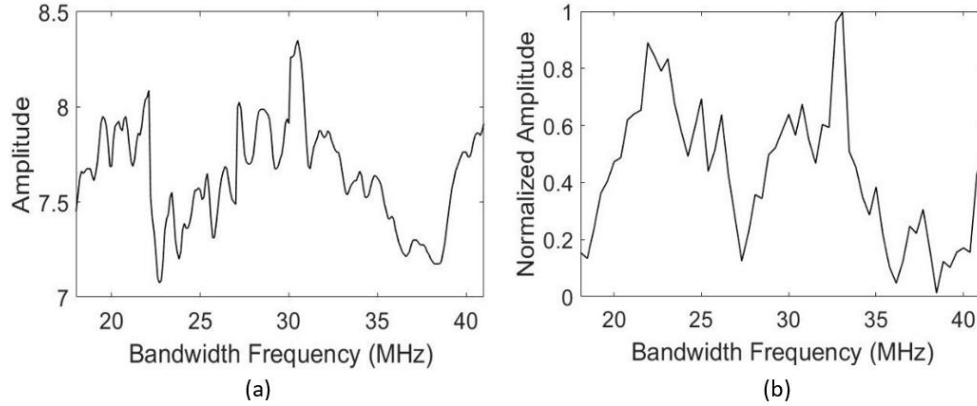
Fig.18 Frequency spectrum from (a) computation model and (b) experimental model

3.3.5   Results

Fig.19 shows the peak density calculated from the experimental analysis at each thickness level. Since there were 14 repetitive measurements conducted for each sample combination, an error bar is provided in Fig.19. The maximum error was ± 1.65 which indicates that the peak density difference between various sample combinations is significant. The peak density result was similar to the computational values. The experimental values also indicated that the peak density is sensitive towards all the parameters in the model. The highest value of peak density was received from the sample having a maximum thickness, scatterer size, and quantity.
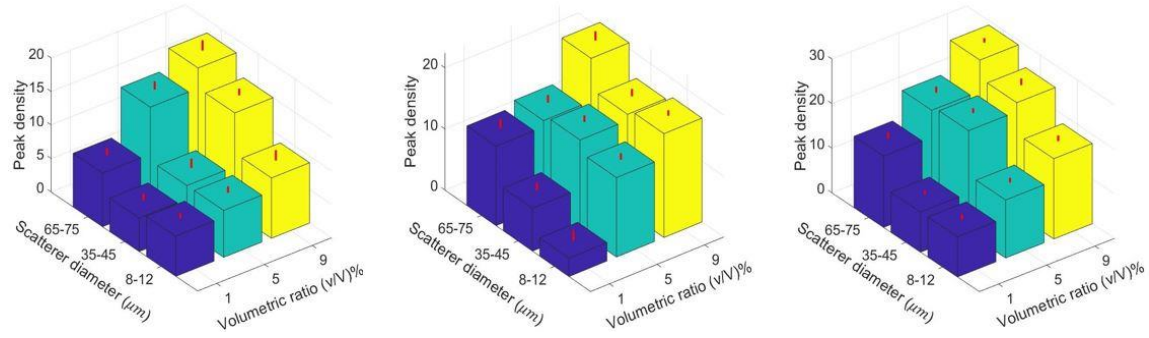
Fig.19 Experimental peak density value for different scatterer number and diameter at wave propagation distance of (a) 1 mm, (b) 2 mm, and (c) 3 mm

Since three different parameters were affecting the multiple scattering as well as the peak density value, it was important to statistically analyze the data to find out the significance level of each parameter. To achieve this, a full factorial DOF analysis was conducted consisting of 3 factors having three levels each to calculate the main effect of the parameters as well as interaction effects. The results are shown in Fig.20.

From the analysis, it was found that peak density is most sensitive towards volumetric ratio, then scatterer diameter, and lastly towards sample thickness. Although the scatterer size was only responsible for the peak density variation in single scattering, the number of scatterers also became effective towards the variation, in the case of multiple scattering. Also, the thickness or wave travel distance became active towards the change of peak density in the case of multiple scattering. Furthermore, there was no parameter interaction significance found in the analysis. It concludes that if one of the three parameters were kept

51

constant, it would not affect the other parameters' contribution towards the peak density variation.
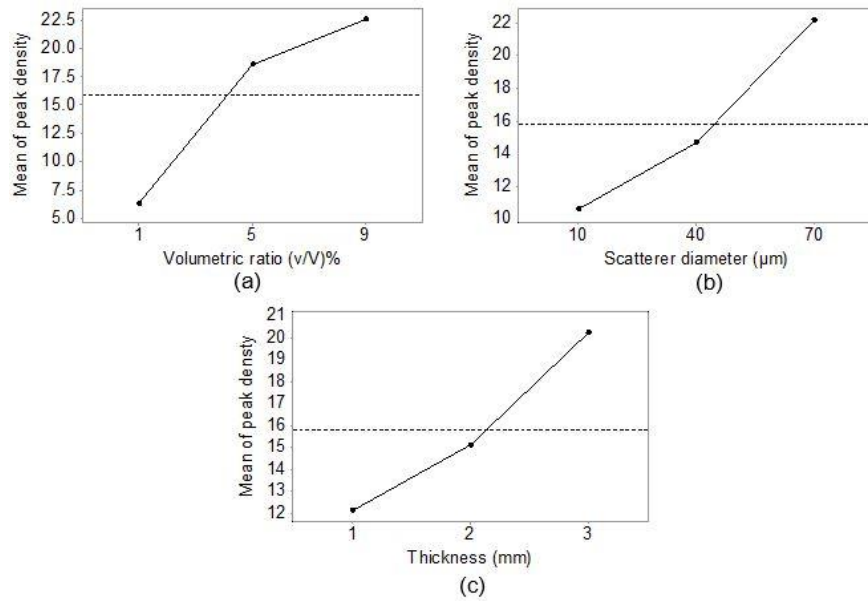
Fig.20 Statistical significance of (a) volumetric ratio, (b) scatterer diameter, and (c) sample thickness on peak density

3.4   Discussion

In this study, the sound scattering of high-frequency ultrasound in a pitch-catch setup was evaluated through analytical, computational, and experimental analysis. The main goal was to establish peak density as a sensitive parameter of high-frequency ultrasound. To achieve the goal, peak density was established as a function of sound scattering. From the analytical study, while assessing the single scattering, peak density was found to be very sensitive towards the change of scatterer size. Also, it showed an increasing trend with the increase in scatterer size. But in the case of changing the propagation path, the peak density did not

52

change since scattered waves did not have any interaction with other waves on their extended travel path. Therefore, to explore the effect of travel paths on peak density, it was necessary to explore multiple scattering where the scattered wave would continuously interact with other scattered waves from different scatterers through the propagation path.

In the computational modeling of multiple scattering, along with scatterer size and propagation path, the number of scatterers was also considered as another factor for peak density. Through computation modeling, it was observed that with increasing scatterer size, propagation distance, and the number of scatterers, the peak density increases. The effect of attenuation on peak density becomes less significant with scatterers being added per unit length at each level of thickness. This gave peak density an advantage while using high-frequency ultrasound before the signal fully attenuates. Furthermore, the effect of the randomness of the position of the scatterers was also evaluated through a simplified model. The factor which was evaluated in that analysis was the inter-scatterer distance. It was observed that with increasing inter-scatterer distance the peak density also increases. As the inter-scatterer distance decreases, the scattering wave interference gets limited in that smaller region of scatterers and does not sustain further while propagating as there are no other waves to interact with.

The experimental results validated the computational findings by showing similar peak density trends in terms of changing scatterer number, size, and propagation distance. It was important to observe the level of influence for each of the factors. Therefore, a full factorial design including three different levels of scatterer number, size, and propagation distance was created considering peak density the outcome. From the statistical analysis, it was

observed that the number of scatterers affects the peak density the most compared with the other two factors. The increasing number of scatterers increases the level of multiple scattering since more scattered waves from multiple scatterers get to interact with each other. Therefore, peak density can be shown as a function of acoustic scattering. As per the experimental setup, peak density can be used towards the detection of mm scale soft material. It has been studied that the inclusion of glass microbeads in tissue phantom increases the scattering quality of the phantom [107]. Furthermore, controlled dispersion of glass microspheres was used to mimic abnormal mass in soft tissues like calcified fibroadenoma containing stromal and epithelial cells [109]. Since a higher amount of glass beads can provide a higher peak density value compared to fewer beads, this parameter can be used to evaluate tissue abnormality by utilizing acoustic scattering. The authors did not find any previous research on phantom preparation by glass microbeads for mimicking either lobular or ductile carcinoma. But with the results obtained in this study, it can be concluded that peak density can be a very promising parameter for ultrasound analysis in cancer detection.

3.5   Conclusion

Ultrasound scattering was evaluated in the study through the pitch-catch technique at a high-frequency level. The scattering was evaluated for various scatterer sizes, numbers, and wave propagation distances. To quantify the scattering, the peak density of the frequency spectrum of the scattered wave was evaluated. It was found that the variation in scatterer number in the microstructure of the medium affects sound scattering the most which resulted in a huge impact on the peak density diversification. Other than that, scatterer size and wave propagation distance also play important roles in the peak density

variation. This makes peak density a very sensitive parameter to the microstructural change. Also, the inter-scatterer distance plays an important role in the multiple scattering for providing peak variation in the case of having the same number of scatterers in a sample in different orientations. Therefore, while working with the pitch-catch technique, peak density can be used to measure the level of multiple scattering while evaluating detailed microstructural characteristics.

CHAPTER 4

FINITE ELEMENT MODELING OF ULTRASOUND C-SCAN IMAGING

In the experimental C-scan imaging conducted by Stromer et al, the pitch-catch method was conducted where two high-frequency transducers of 25 MHz were used [55]. The bandwidth frequency range of the transducer was 22-41 MHz. The received signal was converted to a frequency spectrum and the magnitude variation of that signal was measured in terms of peak density. Based on the peak density value at different locations of the phantom, the C-scan image was reconstructed. For high-frequency imaging, soft pepper flakes and hard pepper seeds were inserted for detection inside the gelatin-based tissue phantom [110]. Although peak density successfully imaged the pepper seed since it was a hard scatterer, it could not identify the soft pepper flake's edge [55]. Therefore, to establish the peak density parameter as an effective through-transmission imaging tool, this limitation needs to be properly addressed and eradicated.

In this study, a computational model of C-scan imaging was developed. COMSOL Multiphysics was used to perform the finite element analysis. The results of this chapter can also be found in [68]. A 2D model was developed to keep the analysis computationally inexpensive. The analysis was conducted in different cross-sections obtained from the original 3D model. The first objective of this study was to mimic the experimental analysis of Stromer et al. by creating a computational model similar to the experimental C-scan imaging setup. Ultrasound propagation was conducted in a parametric study to mimic the imaging technique. A general Gaussian function was introduced in the incident pressure to imitate the pressure distribution in transducer bandwidth. After validating the simulation result by the experimental one obtained by Stromer et al, the computational model was

further utilized to detect the relative position of structure along the acoustic propagation path in the same model. It was observed that while moving the structure from the middle of the sample depth in that direction, the pressure magnitude variation strongly followed a second-degree polynomial trend.

4.1 Finite Element Analysis (FEA) Simulation

4.1.1 Model Description

The first objective of this study was to mimic the experimental analysis of Stromer et al. [55]. Therefore, the simulation model geometry was created by imitating the experimental sample. A gelatin phantom containing soft pepper flake was modeled for the simulation. Pepper flake was modeled as a thin cylinder of 3 mm diameter and 50 µm height. The gelatin phantom was created as a cube of 5 mm in length at each side. The 3D model geometry is shown in Fig.23. The center pepper flake was placed at 0.2 mm along the negative Y-axis from the phantom center.
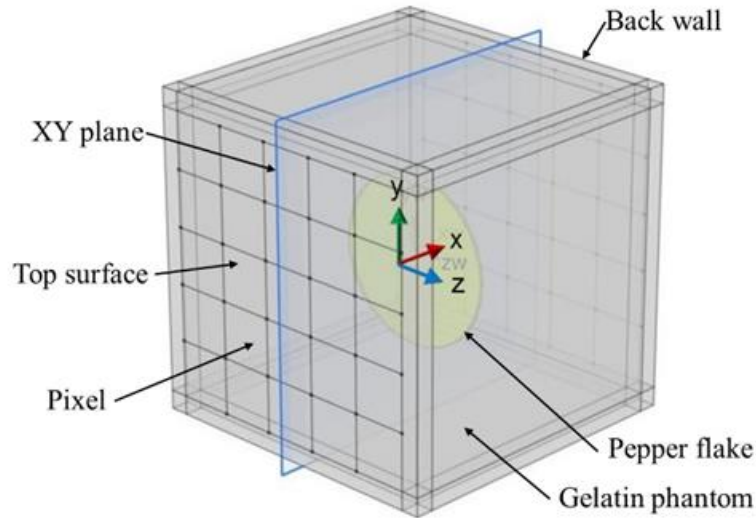
Fig.21 3D model geometry of gelatin phantom containing pepper flake

In the study of Stromer et al, two single-element transducers were used for the C-scan imaging where each transducer crystal diameter was 2 mm [55]. A raster scan pattern was used while selecting the step size as half of the crystal diameter resulting in an image resolution of 1 mm/pixel. Therefore, in this computational model, the top surface of the 3D model was divided into 25 pixels with each pixel area having a dimension of 1 mm on each side. Thus, the image resolution became 1mm/pixel. Similar to the experimental study, ultrasound imaging was conducted in a through-transmission or pitch-catch method. The signal was sent from the top surface and received at the bottom surface (back wall). After receiving the signal, the peak density of the frequency spectrum was measured. Then, the peak density value was used as the pixel value for the C-scan image reconstruction.

4.1.2   Model Simplification

In the case of the 3D model, because of the high frequency, the number of mesh elements was too high. To keep the model computationally inexpensive, the 3D model shown in Fig.23 was divided into 25 XY cross-section planes along the Z-axis. The peak density

result (section 4.1.4) was found very consistent from one cross-section to another. Thus, it was approximated that even with an increasing number of cross-section planes (e.g., 50, or 100 or more), the change in the average peak density value for each pixel would be very insignificant.

The distance between each plane was kept as 0.25 mm. Figure 2a shows 5 of those 25 cross-section planes from the middle of the 3D geometry. During model simplification, the pixel area got converted into lines. Therefore, instead of conducting simulation in the 3D model, the simulation was performed on the simplified 2D model. Finally, the results from all the 2D models were cumulated to get the 3D model result. In the 2D model shown in Fig.22b, the X direction indicates the depth of the sample, as well as the ultrasound propagation direction. The Y-direction indicates the width of the phantom. The gelatin sample was surrounded by a perfectly matched layer to ensure uninterrupted wave propagation (Fig.22b). The 2D geometry was divided into 5 sectors. The sectors were numbered numerically from top to bottom (Fig.22b). In the 2D model, each sector area acted as a pixel volume (voxel) from the 3D model. The ultra-sound wave was sent through each sector in the positive X-direction in a parametric study. For each frequency step, the ultrasound wave pressure was measured at the back wall of each sector. Peak density was calculated from the signal received from the back wall line shown in Fig.22b. Since each pixel area from the 3D model was converted into five lines (five 2D models), the average peak density value from those five 2D models was considered as the corresponding pixel value.
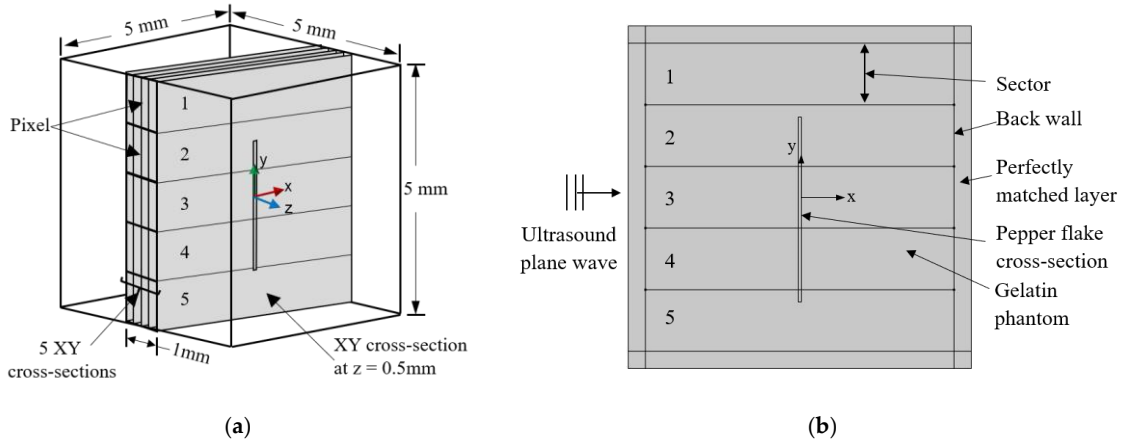
Fig.22 (a) 3D model with simplification details, (b) Simplified 2D XY plane (at Z = 0)

4.1.3   Simulation Physics

In this computation analysis, the underlying physics was similar to the 2D computation study (chapter 3.2) which was used in the previous research. The pepper flake was modeled as a linear elastic solid. The acoustic pressure that was applied to the soft flake was very small ($\leq$ 1Pa). Therefore, the strain value of the solid flake was assumed to be too insignificant to follow a non-linear stress-strain profile. Thus, a linear elastic approximation was considered. Therefore, the governing equations, as well as the boundary conditions, are not discussed here. As an advancement to the previous study, the transducer property was imitated in the input background pressure.

In the fluid and solid domains, the material properties are listed in Table *3* [43][111].

Table 3   Material property

Fluid region

Density (ρ_1)	1067 kg/m^3
Sound velocity	1540 m/s
Attenuation coefficient (α)	8.05 Np/m-MHz

Soft pepper flake	
Young's modulus	1.152×10^7 Pa
Density	608.1 kg/m^3
Poisson's ratio	0.29

A free triangular mesh was created inside the fluid and solid domain. A mapped mesh was used in the perfectly matched layer. A mesh sensitivity analysis was conducted to achieve convergence in the simulation result. With decreasing mesh size, the scattered pressure was calculated for different frequency steps between 22 to 41 MHz. The convergence was achieved for the mesh element size of one-sixth of the wavelength. The simulation was conducted with a mesh of a maximum of 3020168 elements. Computational configuration of a Core i7-9700 processor with 16 GB RAM was used to conduct the simulation.

In the experimental study, the frequency bandwidth of the high-frequency transducer was 22-41 MHz with a center frequency of 31.5 MHz [55]. Therefore, a similar frequency range was used for the computational analysis. Furthermore, the transducer property was closely approximated in the input background pressure by multiplying it with a generalized Gaussian function of pressure distribution among the frequency range (Fig.23) [112]. This enabled us to apply frequency-dependent pressure similar to a transducer with frequency bandwidth. The frequency step size was selected as 100 kHz. The model was computed for

the scattered pressure at each frequency step from 22 to 41 MHz and then all the frequency responses were compiled into a frequency spectrum at the back wall. A peak counting algorithm was used to count the number of peaks and valleys of each spectrum.
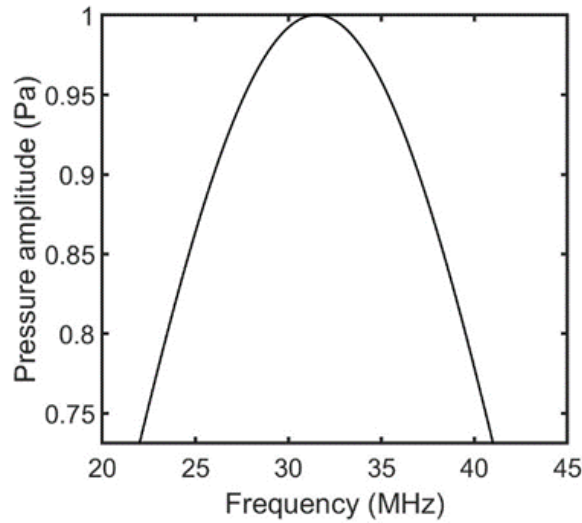
Fig.23 Incident background pressure distribution

4.1.4   Results and Discussion

In the experimental work by Stromer et al. an intuitive threshold pressure magnitude was applied during the peak density calculation which increased the image quality. The purpose of using the threshold value was to eliminate peaks with insignificant pressure magnitude. Similarly, in this study, a small threshold value of 0.02 Pa was applied during peak density calculation. The result shown in Fig.24 represents the peak density of the XY cross-section from the center of the Z-axis for all 5 sectors (Fig.22b). It is observed that peak density was higher in the sectors having a larger amount of pepper flake. Hence sector 1 had the lowest peak density since there was no pepper flake in that sector. Sector 5 also showed a very low peak density instead of having a tiny portion of the pepper flake. During the image

62

construction based on the peak density value, this kind of response (sector 5) resulted in an image that did not visualize a portion of the structure (pepper flake) boundary. This issue was further discussed in the following sections.
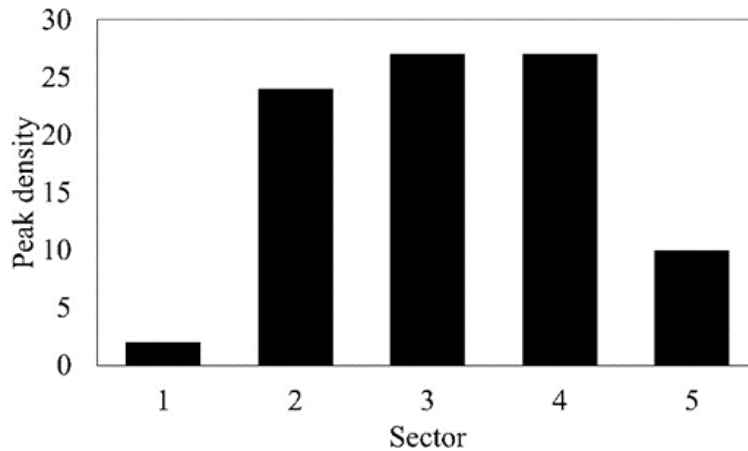
Fig.24 Peak density in all sectors at the center plane (Z=0)

The received signal spectrum was also analyzed for the computational model described above. The purpose of this analysis was to explore the signal propagation in terms of the received signal pattern. In Fig.25, it was evident that the sector 1, and 5 spectrums were similar to the Gaussian distribution of the incident pressure. This was because these sectors had very less, or no amount of pepper flake, and the incident pressure field was almost uninterrupted by the pepper flake. In the case of sectors 3 and 4, all the incident waves went through the pepper flake domain and the incident pressure spectrum was very much affected by the solid domain.

.
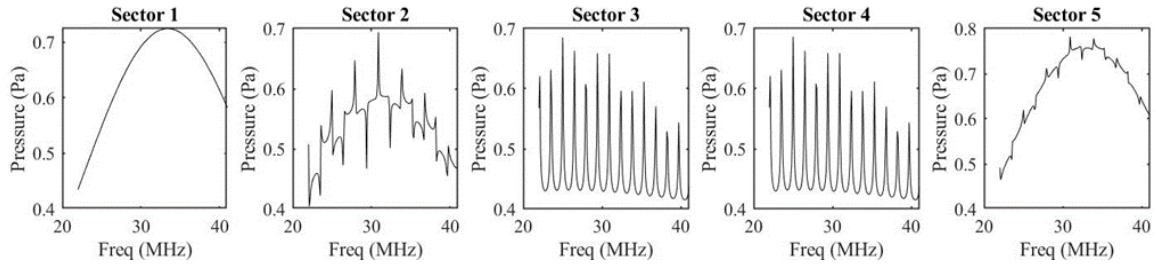
Fig.25 Frequency spectrum in different sectors at Z=0

Fig.26 represents the C-scan image obtained from the computational model. From Fig.26b, it was evident that the pixel area containing the pepper flake had a higher value of peak density compared to the pixel areas having no pepper flake. The higher the peak density, the darker was the pixel shade. The reconstructed image based on peak density value is shown in Fig.26c. Fig.26c delineates that almost all the pepper flake region was identified in the image except for the smaller region on the right side. This result was similar to the experimental results obtained by Stromer et al [55].

(a)   (b)   (c)
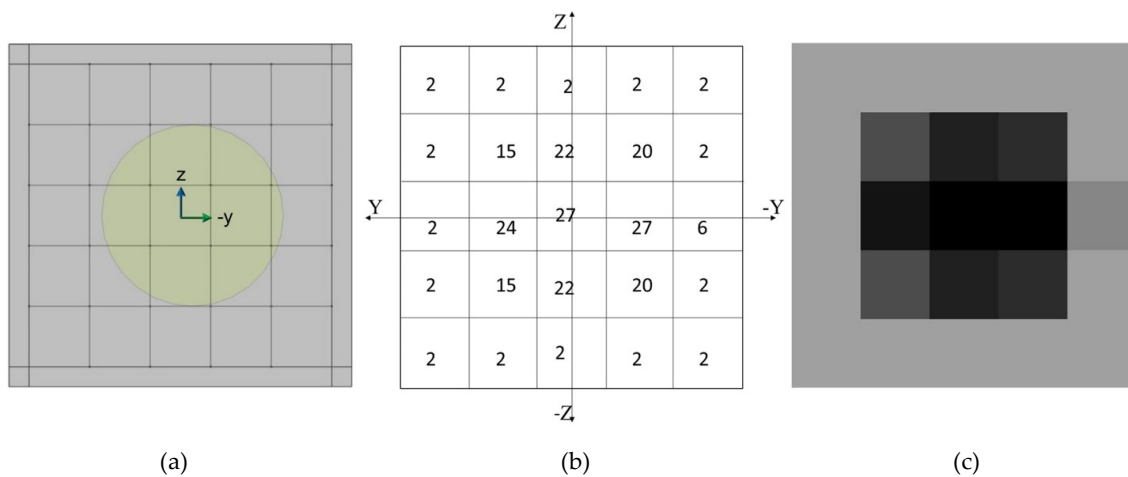
Fig.26 (a) Model geometry (YZ plane view), (b) peak density value of all pixels, (c) reconstructed image based on peak density

64

To avoid the boundary detection issue and to image the object boundaries conclusively, the pixels could be selected in a way that the pepper flake sectors were completely covered by the flake. In that case, all the sectors containing pepper flake would return significantly higher peak density compared to the sectors that did not contain any pepper flake at all (Fig.24). Accordingly, pixel shades having pepper flakes would be more pronounced than the rest of the pixels.

4.2 Structure Position Detection

In C-scan imaging, although the presence of the structure as well as its properties can be detected, little information can be achieved regarding the structure's relative position along the sound propagation path. In the previous section, the effectiveness of the peak density was analyzed in the case of C-scan imaging. In this section, the feasibility of using the peak density will be discussed on detecting the position of the pepper flake in the direction of the gelatin phantom depth while conducting the C-scan imaging.

4.2.1 Model Description

To conduct this study, another computational model was created where a cylindrical pepper flake was placed in the center of the phantom medium. In that way, sectors 3, 4, and 5 were completely covered by the rectangular flake cross-section while sectors 1, and 5 did not contain any flake at all (Fig.27). Since the X direction indicated the depth of the phantom, the rectangular cross-section was moved along the X-axis in both directions from the center of the phantom. Inside the 5 mm depth of the phantom, the flake was moved 0.5 mm each time creating 9 different positions for the flake inside the phantom as shown in Fig.27.

Since the flake was in a symmetrical position along the Y-axis, sector 2 and sector 4 resembled a similar type of sector. Therefore, the simulation was only conducted in sector 2 and sector 3 to detect the flake position. For each flake position, the peak density was calculated and then analyzed to observe any pattern in the peak density that could provide some information regarding its relative position.
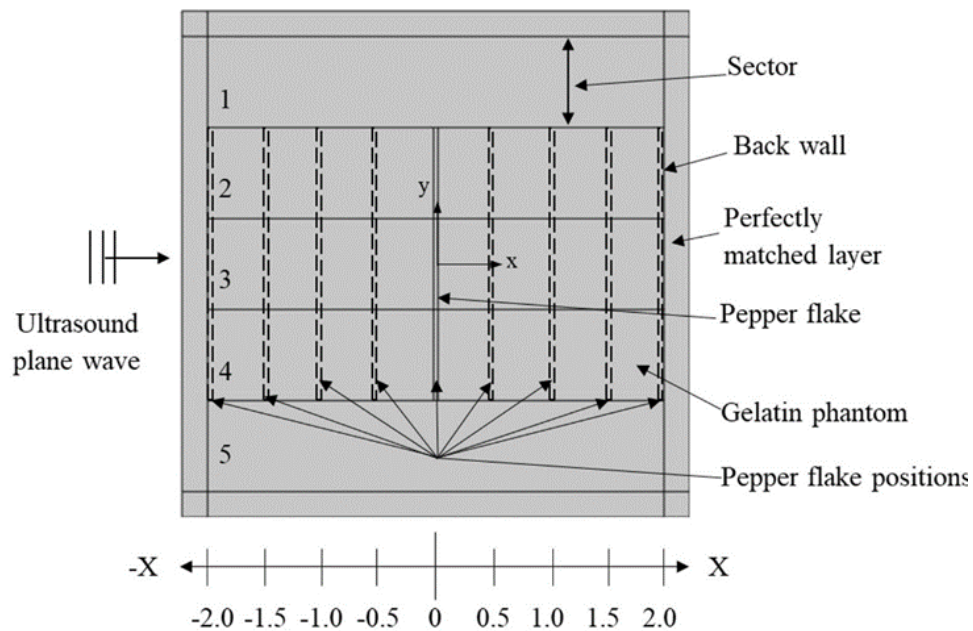
Fig.27 Pepper flake positions

4.2.2   Results and Discussion

Fig.28a, and Fig.28b show the peak density for the different positions of the flake at sector 2 and sector 3, respectively. From both plots, it was observed that the peak density did not change with the flake position. Therefore, the frequency spectrums for both sectors at all positions were analyzed to find any additional correlation.

66
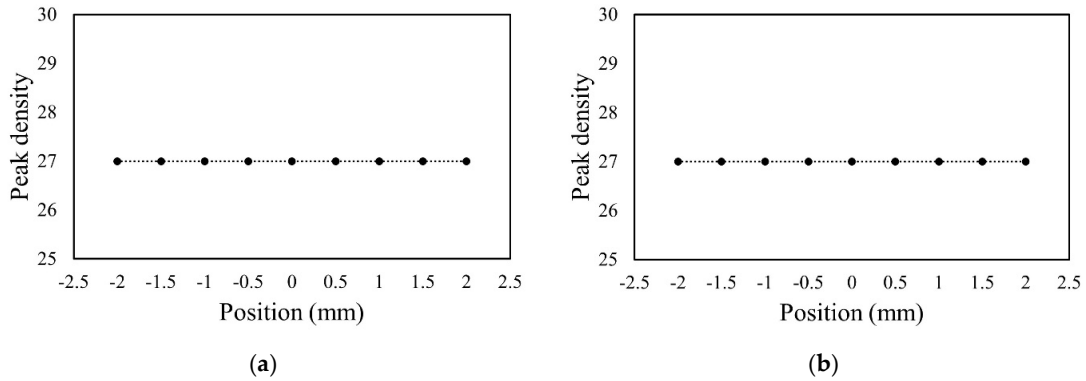
Fig.28 Peak density at all flake positions in (a) Sector 2, and (b) sector 3

Fig.29 and Fig.30 show the spectrums at all positions in sector 2 and sector 3, respectively. In both sectors 2 and 3, the peaks and valleys showed a general pattern with pronounced peaks and valleys. This should be for the case of measuring the wave pressure at the back wall during its gradual compression and rarefaction stages at different frequencies. In both sectors, a similar frequency spectrum pattern was observed. But a slight change in the pressure magnitude was noticed between peaks and valleys at different positions. Therefore, it was understood that, by studying the magnitude variation for those peaks and valleys, a conclusive correlation could be established between the flake position and magnitude variation. However, peak density was not able to depict the magnitude change in those peaks and valleys since the increasing pressure value did not affect the peak density. Therefore, another parameter was developed to depict the magnitude variation while capturing the change in peak or valley magnitude. This parameter was named Mean Peak to Valley Distance (MPVD) as it measured the average magnitude difference between all adjacent peaks and valleys. To measure MPVD, the distance (pressure difference) was

67

calculated from one peak to the next valley, and then from that valley to the next peak, and so on. Then all these distances were averaged to get the final value. Therefore, the MPVD would exhibit a change while the magnitude of the peaks and valleys changed in various locations.
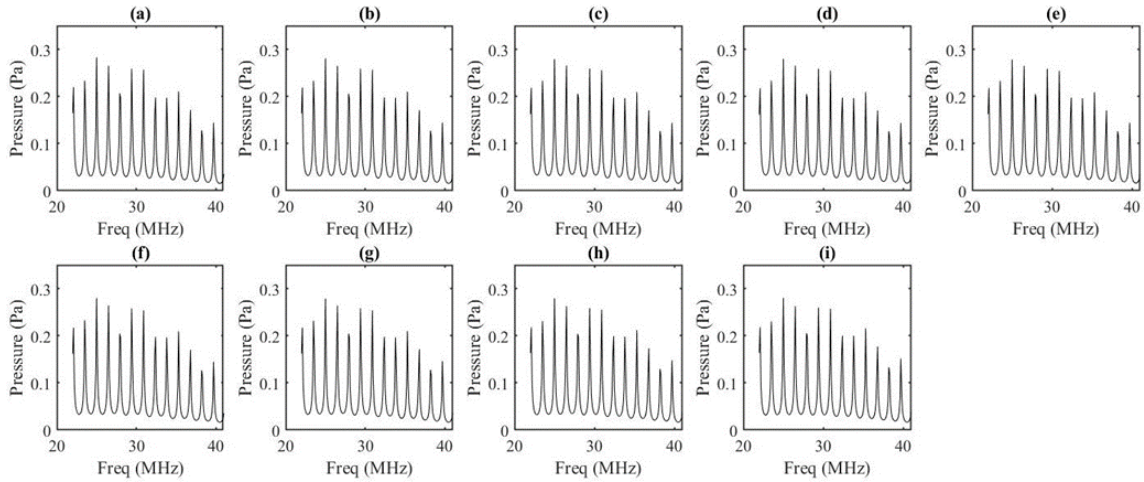
Fig.29 Frequency spectrum in sector 2 for flake positioned at (a) -2 mm, (b) -1.5 mm, (c) -1 mm, (d) -0.5 mm, (e) 0 mm, (f) 0.5 mm, (g) 1 mm, (h) 1.5 mm, and (i) 2 mm
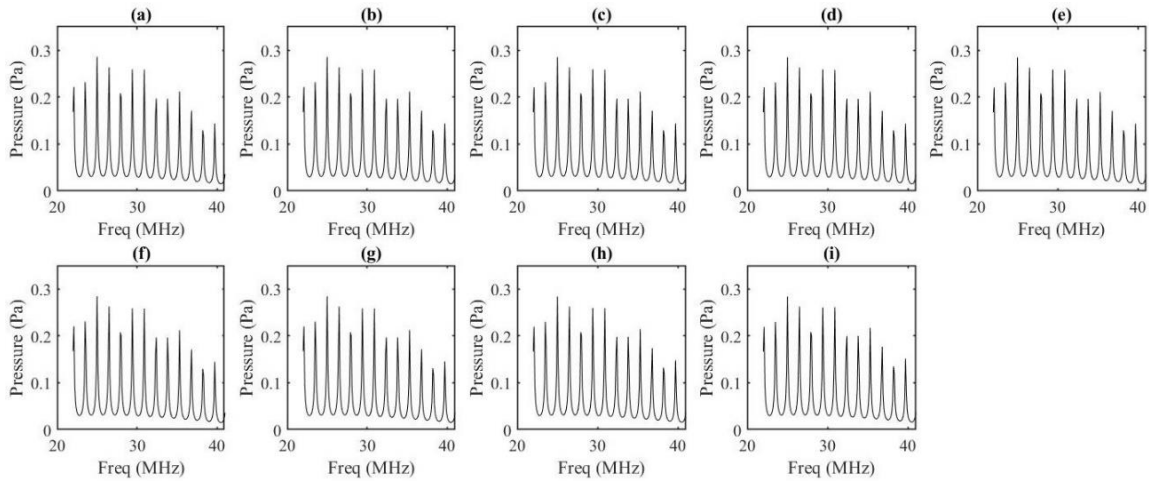
Fig.30 Frequency spectrum in sector 3 for flake positioned at (a) -2 mm, (b) -1.5 mm, (c) -1 mm, (d) -0.5 mm, (e) 0 mm, (f) 0.5 mm, (g) 1 mm, (h) 1.5 mm, and (i) 2 mm

Fig.31a and Fig.31b showed the MPVD results for sector 2 and sector 3 at all the locations of the pepper flake inside the phantom. In both sectors, the MPVD value was found to gradually increasing from the central location while following a 2nd-degree polynomial trendline. Furthermore, the increasing rate of MPVD value was higher while the flake getting closer to the back wall (0 mm to 2 mm) compared to the flake getting closer to the ultrasound source (0 mm to -2 mm). The primary reason behind the polynomial trend should be the flake's various positions where it interacted with the compression/rarefaction phases of the sound wave at those positions. But while the flake moving towards the back wall or bottom of the phantom, the scattered wave from the flake started attenuating less because of the decreasing travel path. Thus, scattered pressure started to increase at the back wall. The increasing pressure contributed to the MPVD value and affected the polynomial trend. Therefore, from -2 mm to 0 mm, the difference between MPVD values (negative slope) decreased while from 0 mm to 2 mm, the positive slope increased. One important factor is that the difference between MPVD values was very small compared to the original spectrum's pressure magnitude. Therefore, to perform this analysis at the experimental level, the frequency spectrums need to be normalized by reference signal to avoid the noise effect during the MPVD calculation [108].
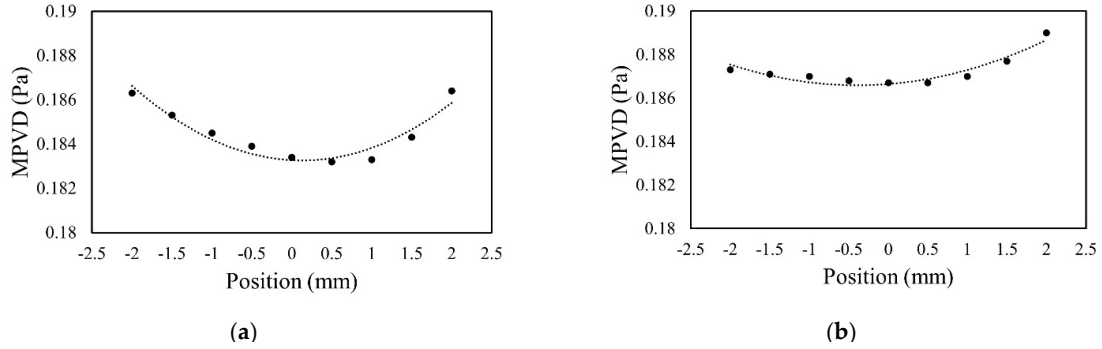
Fig.31 MPVD value at all flake positions in (a) Sector 2, and (b) sector 3

4.3   Discussion

In this study, the feasibility of the magnitude variation of the transmitted ultra-sound signal in the frequency domain was analyzed for C-scan imaging. The magnitude variation was expressed in terms of peak density and MPVD. In a previous experimental study by Stromer et al, peak density was found as a promising nonconventional parameter for C-scan imaging [55]. The study documented some inefficiencies for peak density to detect the boundary of the structure in the case of high-frequency analysis. Therefore, in this study, first, the experimental result from Stromer et al. was imitated in the computational C-scan imaging model which had a similar issue of boundary detection [55]. From the result, it was observed that peak density successfully generated a C-scan image of a thin pepper flake. Although peak density could not conclusively detect the flake's boundary in the pixel areas with a tiny amount of pep-per flake, the issue could be avoided by proper pixel area selection. Furthermore, if a smaller pixel size can be achieved for the imaging through a smaller transducer step size, most of the pepper flakes will be automatically placed fully inside the pixel area resulting in a better image. Even after that, there is a

70

chance of the flake being positioned partially. But it would be a negligible amount and thus the boundary detection would be much better. The smaller pixel can also be achieved experimentally by de-creasing the ultrasound beam width. We already know that smaller beam width is better for the lateral resolution for the conventional ultrasound parameter in C-scan im-aging. Therefore, it is evident that with an unconventional parameter like peak density, a smaller beam width would increase the resolution of the image.

In C-scan imaging, minimal information can be gathered about the structure position along with the depth of the sample. Therefore, studies were conducted by utilizing the magnitude variation to see the feasibility of achieving any information about the structure location. The cylindrical pepper flake was moved along the depth of the phantom for this study and magnitude variation was evaluated in terms of peak density for all locations. It was observed that peak density was not able to capture the change in the spectrum properly since peaks and valleys were changing their magnitude level resulting in similar peak densities for different positions. Thus, peak density could not establish any relationship with structure position. Therefore, the MPVD parameter was used to express the magnitude variation. MPVD perfectly captured the magnitude change of peaks and valleys. With gradually positioning the flake from the middle to the bottom of the phantom as well as to the transducer, the MPVD value showed a strong increasing trend. Therefore, the MPVD value can give us information about the structure location while creating C-scan images. To have more accurate information, only the significant peak and valley magnitude can be observed. Also, it is expected that with different shapes of the structures, significant peaks and valleys will be created at different frequency steps. It can also create a different pattern

71

of the signal. Thus, by analyzing the signal pattern more information can be gathered regarding the shape of the structure without imaging the sample.

In the medical sector, this C-scan imaging technique can be used to image tissue heterogeneity. To detect cancerous margins during breast-conserving therapy (BCT), it can be used to identify positive/negative margins instantly. The main challenge of using high-frequency ultrasound in C-scan imaging would be its increasing attenuation rate which limits this application to a low thickness level. In recent years, research had been conducted to evaluate quantitative ultrasound parameters in photoacoustic measurement and imaging [113], [114]. Therefore, future research can be done to evaluate the sensitivity of peak density to optical absorbance. With a promising result, this technique can be merged with photoacoustic C-scan imaging for much better imaging performance.

4.4 Conclusion

Computational modeling of ultrasound C-scan imaging was developed to analyze the feasibility of the peak density parameter of the transmitted frequency spectrum. A previous experimental study was imitated in the computational model for the validation of the analysis. The thin structure was successfully imaged through the computational study. With proper pixel area selection or smaller pixel size, a better boundary detection can be achieved in C-scan imaging while using the ultrasound peak density parameter. Peak density was not effective in giving information regarding the relative position of the structure along with the sample depth. Therefore, the magnitude variation of the signal was analyzed with MPVD parameter instead of peak density to detect structure position. With the increasing depth of the pepper flake inside the gelatin phantom, the MPVD value

72

changed while following a polynomial function. Therefore, in pitch-catch analysis, magnitude variation of the frequency spectrum is an effective tool for C-scan imaging as well as for extracting additional information about structure position.

CHAPTER 5

IDENTIFYING BREAST TUMOR GRADES THROUGH HIGH-FREQUENCY

ULTRASOUND

In this study, high-frequency ultrasound analysis was conducted computationally to evaluate multiple forward acoustic scattering to detect different histological features of cancerous tissue [115]. Two important factors from the histological grading were considered for the tissue modeling which were nuclear pleomorphism and malignant cell density. The design of experiment (DOE) also included two different cellular shapes-circular for initial approximation and elliptical for a close approximation. 22 to 41 MHz frequency range was used in this study to keep similarity with the previous research [70], [116]. Different response parameters in the frequency domain were evaluated in this study. One of the response parameters was spectral peak density that was found very responsive against microstructural changes [116][108]. The average magnitude difference between all the adjacent peaks and valleys was also analyzed which was called Mean Peak to Valley Distance (MPVD). Furthermore, the spectral pattern was analyzed to find out significant features of the spectrum from various malignant features. It was observed that with cellular structures tending towards the cancerous level, peak density increased and MPVD value decreased. Also, the cellular density contributed more to the multiple scattering than the pleomorphism.

5.1   Design of Experiment

Pathologists grade breast tumors based on three criteria. Among those criteria, nuclear pleomorphism and malignant cell density were selected for this study to create the DOE. In the case of nuclear pleomorphism, a total of 4 levels of nuclear diameter were used. The

initial nucleus diameter or the healthy nucleus diameter was kept as 10 µm. To delineate the gradual severity of the cancerous stage, the nuclear diameter was increased by 20% (12 µm), 40% (14 µm), and 60% (16 µm). For the initial stage, the healthy number of epithelial cells was kept as 750. In the case of increasing malignant cell density, the number of added malignant cells in normal tissue was 375 and 750. Therefore, with increasing cellular density, the total number of cells became 1125, and 1500 respectively. Furthermore, in previous research, the cells were approximated as spherical shaped where it was found that a closer approximation could be achieved through spheroidal cellular shape [62]. Therefore, the cellular shape was also considered as another factor for the DOE. Since simulations were conducted in two-dimensional models, the spherical and spheroidal cellular shape was considered as circular and elliptical, respectively. Another approximation was considered that the cell cross-sections were all taken from their center plane. Thus, the area of the cell and nucleus was kept uniform in all DOE combinations. Furthermore, to model elliptical cells, the direction of the major and minor axis of the ellipse became an important factor to consider. Since, in the cancerous stage, the malignant cells were arranged loosely from each other, the elliptical cells' major and minor axis could be in any direction inside the tissue. In this study, only two orientations of the elliptical cells were considered (horizontal and vertical). These orientations were equally distributed between normal and malignant cells.

In summary, the DOE consisted of 3 factors where nuclear pleomorphism, cell density, and cellular shape consisted of 4, 2, and 2 levels, respectively. Therefore, a total of 24 combinations were created for the full factorial design. Table *4* shows all the combinations that were analyzed in this study. From this table, combination 1 depicted the healthy breast

tissue, and combination 2 and 14 only showed increasing cellular density with no pleomorphism. Thus, combinations 2 and 14 were only depicted as dense breast tissue with no malignancy. Combinations 4, 7, and 10 from the circular shape model were similar to combination 1. Combinations 16, 19, and 22 from the elliptical cell model were similar to combination 13. In both cases, since there were no added malignant cells, nuclear pleomorphism was not considered. But these combinations were kept in this study to maintain consistency while analyzing the response parameter.

Table 4   Design of experiment (DOE)

Comb no.	Cell shape	Increase in malignant nucleus diameter (%)	Added number of malignant cells	Comb no.	Cell shape	Increase in malignant nucleus diameter (%)	Added number of malignant cells
1	Circular	0	0	13	Elliptical	0	0
2	Circular	0	375	14	Elliptical	0	375
3	Circular	0	750	15	Elliptical	0	750
4	Circular	20	0	16	Elliptical	20	0
5	Circular	20	375	17	Elliptical	20	375
6	Circular	20	750	18	Elliptical	20	375
7	Circular	40	0	19	Elliptical	40	0
8	Circular	40	375	20	Elliptical	40	375
9	Circular	40	750	21	Elliptical	40	750
10	Circular	60	0	22	Elliptical	60	0
11	Circular	60	375	23	Elliptical	60	375
12	Circular	60	750	24	Elliptical	60	750

For characterizing these different combinations, two response parameters were analyzed in this study. One of the response parameters was the ultrasound peak density of the frequency spectrum. The second response parameter was Mean Peak to Valley Distance (MPVD). Furthermore, the spectral pattern (large peaks or valleys, jaggedness, etc.) was analyzed to extract detailed frequency information for evaluating tissue microstructure at different malignancy levels.

5.2 Model Description

In the model geometry, the cells were generated randomly for both normal and malignant cases. The cells were created in a way that there was no inter-cellular contact. Thus, the model depicted loosely bonded cells inside the tissue. The model consisted of extracellular matrix, cytoplasm, and nucleus. Fig.32 depicts the model geometry for combinations 12 and 24 from the DOE. Both combinations had normal cells as well as malignant cells where the cellular shape was circular and elliptical, respectively. The malignant cells were evident in the model geometry as they had a larger nucleus (60% pleomorphism). In the case of the elliptical geometry, the cells were arranged in two different orientations based on their major and minor axis. A plane ultrasound wave was sent in the positive x-direction. For smooth acoustic wave propagation through the tissue boundary, a perfectly matched layer (PML) was introduced in the model. The 2D model area was 1300 µm x 1300 µm in dimension. In the case of the circular-shaped cellular model, the cell diameter was 25 µm [117], [118]. For the elliptical-shaped cellular model, the major and minor axis lengths of the cell were approximated 25 µm and 16 µm respectively.
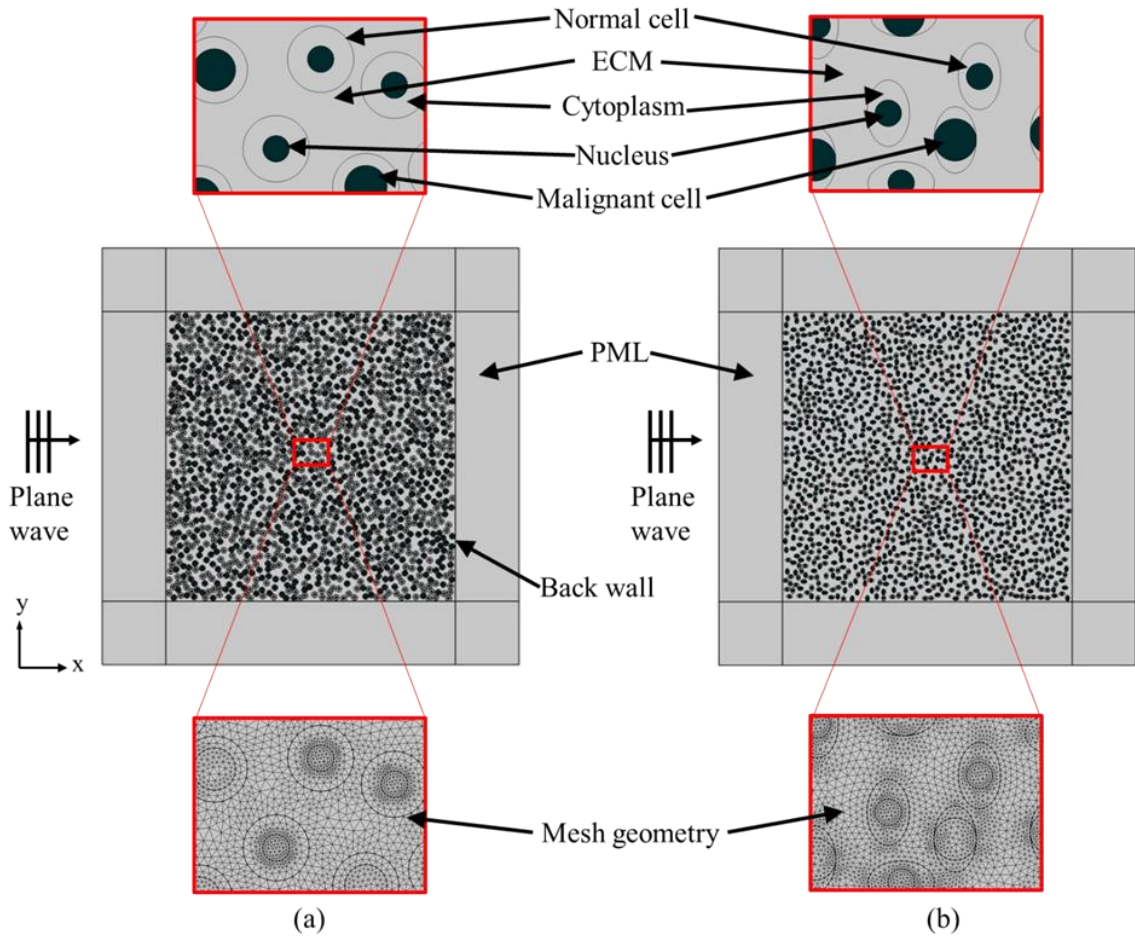
Fig.32 Model geometry of (a) combination 12 and (b) combination 24 from the DOE

5.3 Simulation Physics

Previously, computational modeling was conducted by approximating the ECM, nucleus, and cytoplasm as both solid and fluid [119]. Since the goal of this research was to explore the multiple scattering and different geometric features of the cell, all histological features were considered fluid. In the fluid medium, the acoustic wave propagation followed the Helmholtz equation shown in Eq. (1). The equation provides the acoustic pressure distribution as a function of frequency inside the medium.

78

$$\nabla.\left(-\frac{1}{\rho_c}(\nabla p_t - \boldsymbol{q_d})\right) - \frac{k_{eq}^2}{\rho_c}p_t = Q_m \tag{1}$$

In fluid, for the speed of sound c_c, attenuation coefficient α, and frequency f, the equivalent wave number, k_{eq} can be shown as

$$k_{eq}^2 = \left(\frac{2\pi f}{c_c} - i\ln(10)\frac{\alpha}{20}\right)^2 - k_z^2 = k^2 - k_z^2 \tag{2}$$

In this model, out of plane wave number k_z was set to zero. Monopole and dipole source term Q_m and $\boldsymbol{q_d}$ were both zero in this system. ρ_c is the fluid density. The total pressure, p_t is the summation of the background pressure field (p_b) and scattered pressure field (p_s). In the model, the background pressure field was expressed as wave propagation in $\widehat{e_x}$ direction defined as $p_b = p_0 e^{-ikx}$. Here k is the wavenumber which is the function of frequency (f) showed in Eq. (2).

Material properties in ECM, cytoplasm and nucleus are included in Table 5 [119].

Table 5   Material properties

	ECM	Cytoplasm	Nucleus
Density, ρ_c (kgm^{-3})	1060	998	1430
Longitudinal wave speed, c_c (ms^{-1})	1570	1483	1509
Attenuation coefficient, α $(dBm^{-1}MHz^{-1})$	70	70	70

The simulation was conducted for a high-frequency range from 22 to 41 MHz mimicking a high-frequency transducer with frequency bandwidth. In general, ultrasound transducers send pressure waves for a frequency range where the pressure magnitude is distributed in a bell-shaped curve and the maximum pressure magnitude is found at the center frequency. Therefore, the input background pressure for this model was distributed in a bell-shaped pattern over the frequency range and the maximum pressure amplitude was kept at 31.5 MHz (Fig.33). Furthermore, the frequency bandwidth was selected at 50% of the maximum amplitude. Therefore, pressure at 31.5 MHz was selected as 1 Pa and at both 22 and 41 MHz, it was kept 0.5 MPa (50% of max amplitude).
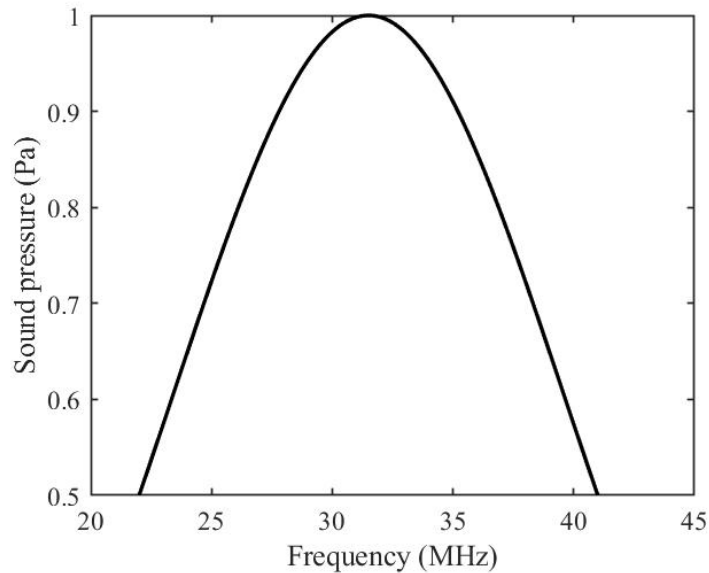
Fig.33 Background pressure distribution over the input frequency range

The frequency step size was 100 kHz for this model. Therefore, from the 22 to 41 MHz range, the model calculated scattered pressure for 190 frequency points. The average scattered pressure for each frequency point was measured from the back wall of the model geometry shown in Fig.32. Then the frequency spectrum was generated by accumulating all the scattered pressure in the frequency range. The free triangular mesh was used in the tissue geometry and the mapped mesh was used in the PML region. Mesh element size was selected as one-sixth of the wavelength.

To calculate the peak density, the number of peaks and valleys were counted from the frequency spectrum [17]. For calculating the MPVD parameter, the average pressure difference between all adjacent peaks and valleys was measured.

5.4   Results and Discussion

Fig.34 represents the peak density result for all the histological feature combinations in the cellular cell and elliptical cell model. In both models, it was evident that the peak density followed an overall increasing pattern with the increased number of malignant cells as well as increased nucleus size (pleomorphism). In the circular cell model (Fig.34a), the trend was more evident compared to the elliptical cell model (Fig.34b). The possible reason behind that could be the uniform cell area surrounding the nucleus in the circular model. This uniform cell shape created a homogeneous intra-cellular scattering compared to the elliptical cell model. A full factorial DOF analysis was conducted to inspect the main effect of the two histological features on peak density for both circular and elliptical-shaped cellular models. From Fig.35, it was evident that in circular models, malignant cell density had a profound impact on the increasing peak density. The pleomorphism had a non-

81

monotonic impact where it increased the peak density initially, but it seemed that the effect

was saturated after 20% pleomorphism. It also indicated that the multiple scattering causing

in the intra-cellular level affected peak density up to a certain level. General trends also

showed a similar impact in the elliptical shape model where malignant cell density

generally tended to increase the peak density. The pleomorphism did not seem to affect

peak density that much in the elliptical shape model.
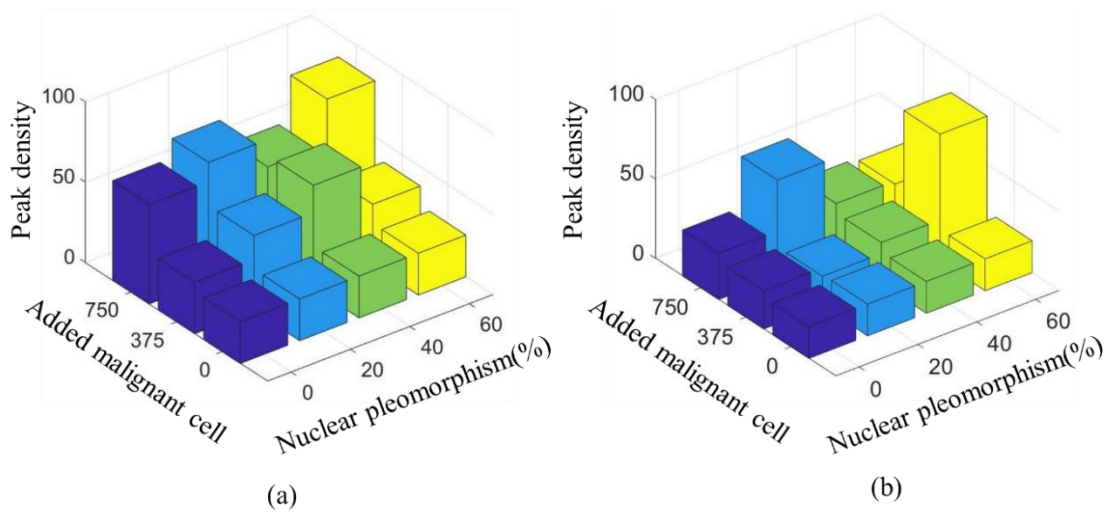
Fig.34 Peak density for (a) circular cell model (b) elliptical cell model
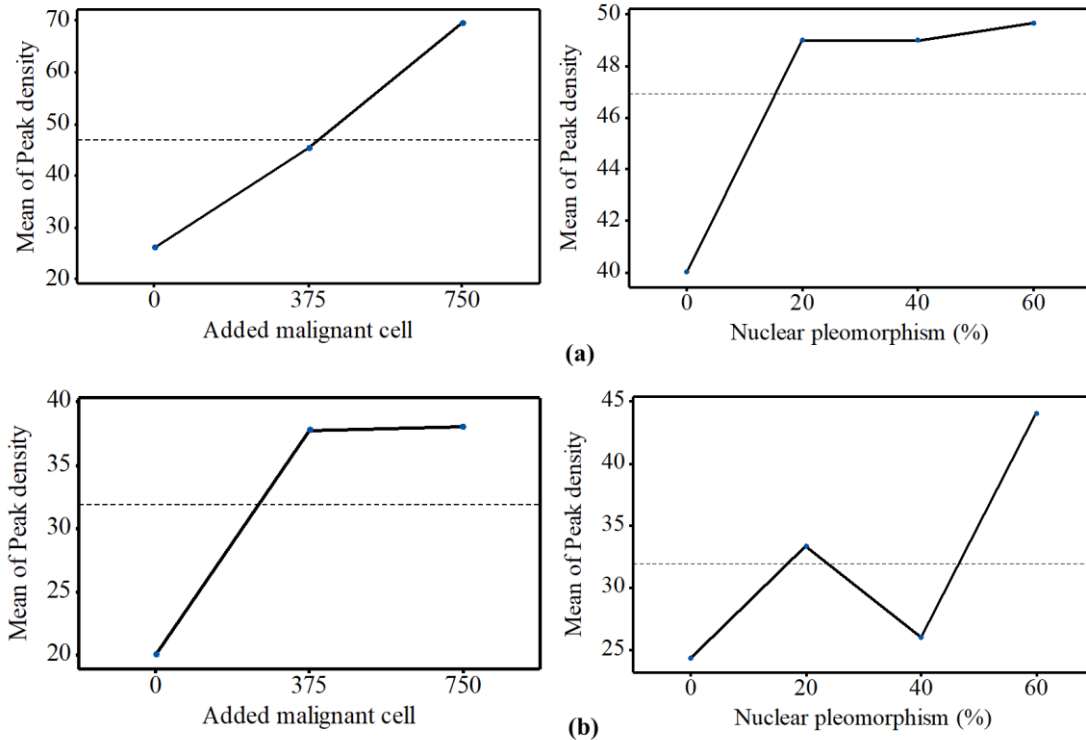
Fig.35 Main effects plots for the peak density in (a) circular-shaped, (b) elliptical-shaped

cell

In the case of the MPVD result, an overall decreasing trend with increasing histological features (cell density, pleomorphism) was observed only for the circular cell model (Fig.36a). The elliptical cell model failed to create a general correlation between MPVD and the histological features (Fig.36b). In the case of the main effect from the statistical analysis, it was observed that only the added number of malignant cells in the circular model affected the MPVD decrease (Fig.37). In the rest of the cases from Fig.37, the histological features affected the MPVD outcome insignificantly.
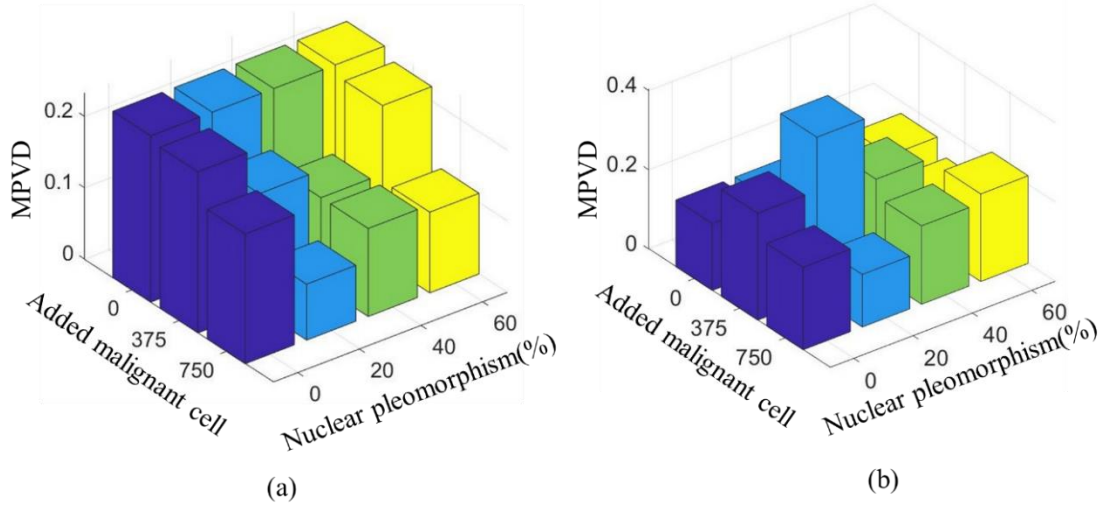
Fig.36 MPVD result for (a) circular cell model (b) elliptical cell model
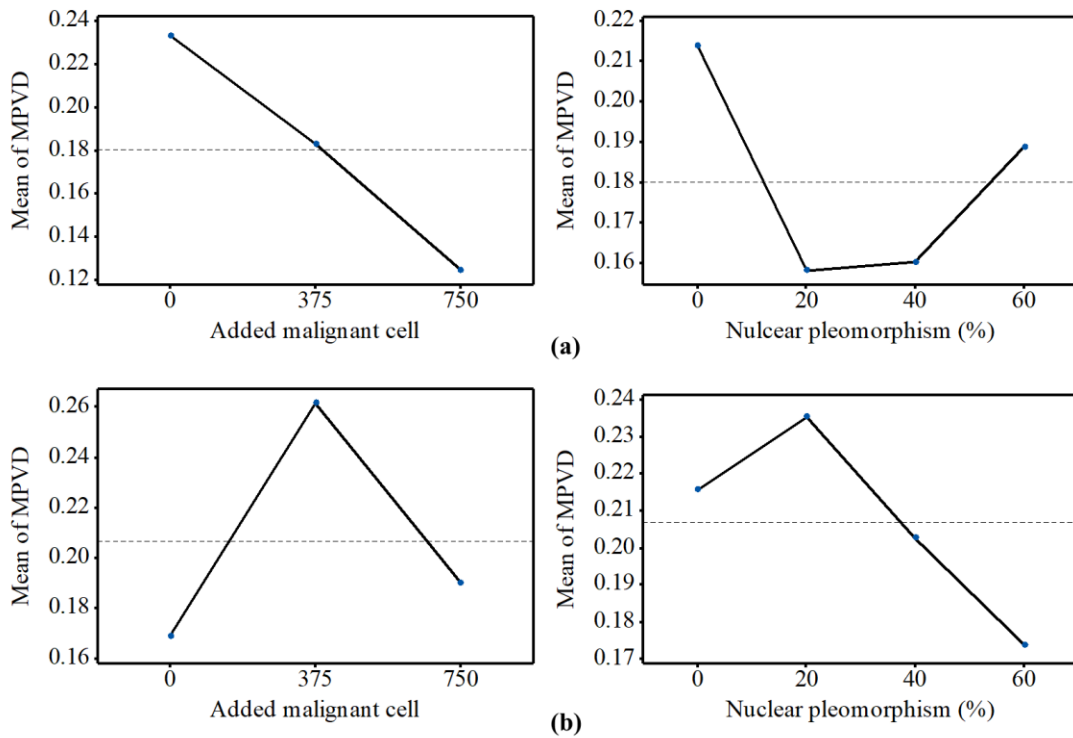
Fig.37 Main effects plots for the MPVD in (a) circular-shaped, (b) elliptical-shaped cell

84

MPVD variation depends on the peak to valley pressure difference in the frequency spectrum. Therefore, if the spectrum patterns remain similar while the peak to valley pressure magnitude varies, the MPVD trend could be more conclusive. In this study, since the cells were randomly dispersed, the scattering behavior was fully random. Even though the spectrums in all cases had a similarity at a certain level, the pressure magnitude was too random to provide a meaningful MPVD pattern. In the case of the circular cell, the scattered wavefront from the cells was consistent in all directions compared to the elliptical cells because of their geometry. In the horizontal elliptical cell, the forward scattering was more dominant compared to the vertical elliptical cell. Therefore, the randomness in scattering from the elliptical cell was more prominent compared to the circular cell. The only time MPVD showed a consistent decreasing trend, was for the added malignant cell parameter in the circular cell model. Although having random cell distribution, the shape consistency helped to create a better MPVD response in that case. It indicated that with increased scattering due to excess malignant cells, the peak to valley pressure magnitude decreased over the frequency bandwidth. Overall, for random cell dispersion, MPVD was not an effective response parameter to analyze.

The spectral pattern was also analyzed in this research to extract further information about different malignancy levels. For both cellular and elliptical models, the frequency spectrums were divided into two groups. Group 1 consisted of the signals acquired from 375 added malignant cells (Fig.38a and Fig.39a), and group 2 consisted of the signals acquired from 750 added malignant cells (Fig.38b and Fig.39b). In both groups, the

frequency spectrum from normal/healthy tissue (without malignant cells and pleomorphism) was added as a reference to visualize the change in spectrums for different malignant grades. In the case of the circular cell model, from Fig.38a, it is evident that all the spectrums with 375 malignant cells followed the overall bell-shaped pattern of the input background pressure. For the healthy tissue spectrum, a large peak between 30 to 35 MHz region was observed. A similar peak with slightly increased amplitude was seen when 375 cells were added with no pleomorphism (dense healthy tissue). But with increasing nuclear pleomorphism in the 375 malignant cells, the peak started to disappear. And finally, with 60% pleomorphism, the peak completely disappeared for the malignant tissue. In the case of the 750 added malignant cells (Fig.38b), this pattern was more pronounced. In the case of 750 added cells, for the dense healthy tissue, the peak between 30-35 MHz region had a much higher amplitude than the healthy tissue spectrum. But it started to decrease with increased nucleus size. Finally, similar to the 375 malignant cells, the peak completely vanished with 60% increased nucleus size in malignant tissue. Overall, in both 375 and 750 malignant cells, the jaggedness in the frequency spectrum started to increase with increasing nucleus size.
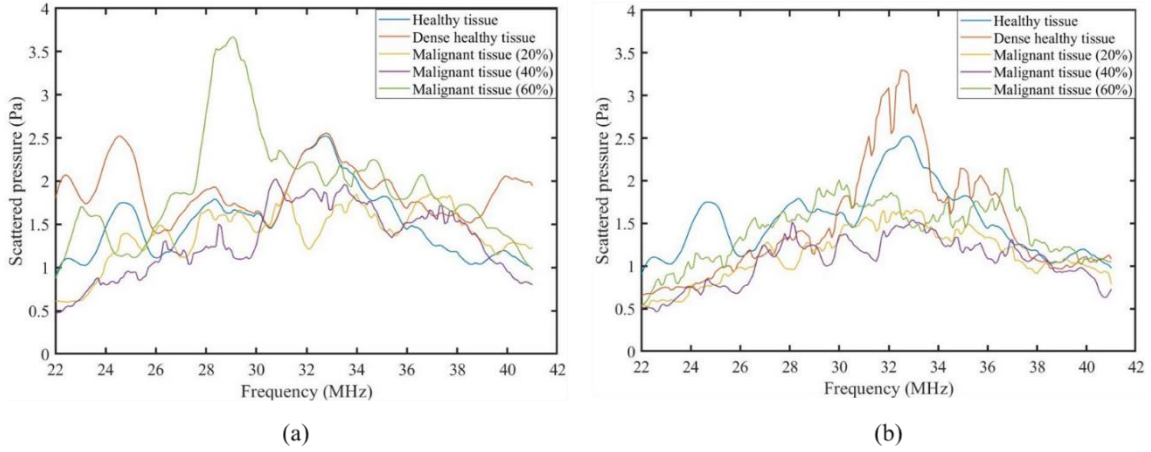
Fig.38 Circular cell: frequency spectrum of the normal histological spectrum with (a) spectrums for 375 added malignant cells at different pleomorphism levels, (b) spectrums for 750 added malignant cells at all pleomorphism levels
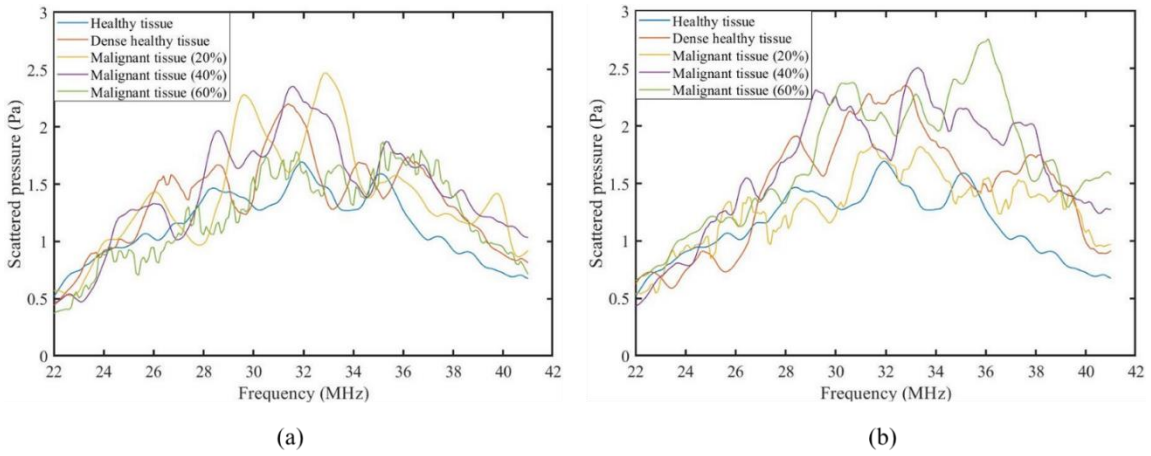
Fig.39 Elliptical cell: frequency spectrum of the normal histological spectrum with (a) spectrums for 375 added malignant cells at different pleomorphism levels, (b)spectrums for 750 added malignant cells at all pleomorphism levels

In the case of the elliptical cell shown in Fig.39, the spectrums with 375 and 750 cells followed an overall similar pattern to the circular cell. One major difference compared to the circular model was that there were two large peaks instead of one in the non-malignant spectrums as well as in the spectrum with low pleomorphism (20%). But similar to the circular cell model, these peaks gradually disappeared with increased pleomorphism and increasing jaggedness was observed in their pattern. Another difference that was spotted in the elliptical cell spectrums was the overall scattered pressure amplitude. All the spectrums with added malignant cells had a higher amplitude level compared to the healthy tissue spectrum.

From the spectral pattern, it was observed that although the nuclear pleomorphism had less of an effect on the response parameters (peak density and MPVD), it certainly affected the frequency spectrum. Therefore, by studying the frequency spectrum, information about nuclear pleomorphism can be extracted.

5.5   Conclusion

High-frequency ultrasound (22-41 MHz) was used to detect histological features in breast tumor tissue in a finite element analysis study. Histological features were selected for the study based on malignant tumor grading criteria. Malignant cell density and cell nuclear size were varied at multiple levels for the ultrasound measurement. The circular and elliptical cellular shapes were used for both histological features. Ultrasound peak density and MPVD parameters were evaluated to detect the different combinations of malignant features. Peak density showed a strong increasing correlation against the increasing number of malignant cells and malignant nucleus size for both cellular shapes. In contrast to that,

the MPVD parameter responded with a decreasing trend against the histological features only for the circular cell shape. For the elliptical cell shape, MPVD failed to provide a conclusive trend. Among the two histological features, malignant cell density was found dominant against the response parameters. The spectral pattern was also evaluated for all malignant feature combinations. The jaggedness increased in the frequency spectrum with increasing feature levels. A large peak was observed at the center region (30-35 MHz) of the frequency range for the normal tissue and primary malignant tissue. The center peak disappeared with increasing nuclear pleomorphism. Thus, by studying the spectral pattern, pleomorphism information could potentially be extracted. Overall, spectral variation in the frequency level showed a comprehensive correlation with different tumor grades.

CHAPTER 6

SURGICAL MARGIN ANALYSIS THROUGH QUANTITATIVE ULTRASOUND

One of the asymptotic breast carcinomas is ductal carcinoma in-situ (DCIS). The growth of malignant epithelial cells inside the breast duct is known as DCIS or intraductal carcinoma or stage zero cancer [120]–[122]. It is a non-invasive form of carcinoma which means that the cancerous cells are yet to spread outside of the duct or surrounding breast tissue. It occurs due to the genetic mutations in the cells of the breast duct [122]. It develops initially at a terminal duct lobular unit and then extends into the mammary ductal lobular system [123]. In the United States, around 60,000 DCIS cases are diagnosed every year and account for 20% to 25% of all breast carcinoma [124]–[127]. From the literature, a wide range of DCIS visibility (8-50%) through ultrasound imaging was found. But overall, ultrasound imaging is considered the least useful imaging technique to detect DCIS [128]. Therefore, quantitative ultrasound parameters, as well as spectral ultrasound analysis need to be explored in margin analysis to detect asymptotic malignancies like DCIS.

In this study, quantitative high-frequency ultrasound analysis was done through finite element modeling of multiple noninvasive breast duct pathologies of the surgical margin [129]. The analysis was done on different cancerous (positive) as well as noncancerous (negative) margin models. High-frequency ultrasound (22-41 MHz) was used for the analysis in both pulse-echo and pitch-catch methods. In this study, the surgical margin models consisted of normal duct, atypical ductal hyperplasia, malignant duct (DCIS), and calcified duct (benign and malignant) models. In the case of microcalcification, all three types of calcification compositions were used for modeling- (1) Calcium oxalate (CaC_2O_4), (2) Calcium carbonate ($CaCO_3$), and (3) Hydroxyapatite/HAp ($Ca_{10}(PO_4)_6(OH)_2$). While

calcium oxalate and calcium carbonate are associated with benign tumors, HAp is associated with malignant tumors [130]. The goal was to observe the feasibility of quantitative ultrasound to differentiate duct pathologies inside margin without calcification as well as to identify different types of microcalcifications which eventually would indicate the margin status (positive or negative). Quantitative ultrasound parameters like peak density and MPVD were used for the ultrasound evaluation because of their sensitiveness to the soft material microstructure [55], [68]. It was found that for the pitch-catch method, only the peak density parameter correlated with the pathological features of the breast duct with a conclusive pattern. In contrast to that, for pulse-echo mode, only the MPVD parameter provided a conclusive pattern to differentiate the pathological features of the breast duct. Furthermore, frequency domain spectral analysis was conducted to visualize the spectrum patterns. The goal was to correlate different features of the frequency spectrum with the margin models. From the spectral comparison, it was found that spectral features like overall pressure magnitude, peak pressure magnitude, and spectrum jaggedness could also provide meaningful information to differentiate various types of breast duct pathologies inside the margin.

6.1 Design of Experiment

The goal of this study was to explore the feasibility of quantitative ultrasound as an efficient intraoperative tool for surgical margin detection. The focus of this analysis was to identify DCIS during margin-tissue evaluation. To detect DCIS during the margin tissue examination, it was necessary to differentiate it from all other noninvasive histopathological cases of the breast duct. Therefore, in this study, different pathological cases of the breast duct were modeled. The first model that was considered for the study

was a normal breast duct. In the simplified normal duct model shown in Fig.40a, the duct contains glandular tissue while being surrounded by fatty/adipose tissue [131]. The duct diameter varies from 1 mm to 5-8 mm starting from the lobule to the nipple [132], [133]. In this case, the duct diameter is selected as 1 mm. Inside a normal duct, the glandular tissue contains two layers of epithelial cells [134]. The epithelial cell diameter is considered as 20 µm [119]. Therefore, the glandular tissue thickness is 40 µm in this model. Duct fluid is presented inside the normal duct. Based on the literature, the duct fluid is assumed as water [135]. The duct is surrounded by fatty tissue. In this 2D model, the fatty tissue dimension is 2 mm x 2 mm which is kept consistent for all the breast duct models in the design of the experiment (DOE).

Another proliferative breast disease that can be found in breast cancer tissues is ductal hyperplasia which occurs because of the overgrowth of epithelial cells inside the duct [124]. Three types of hyperplasia can occur inside the breast duct: (1) mild hyperplasia, (2) moderate hyperplasia, and (3) atypical ductal hyperplasia (ADH). In the case of the ADH, the risk of forming DCIS is 4 to 5 times higher than the normal duct [124]. In this study, the ductal hyperplasia was modeled in the form of ADH which is shown in Fig.40b. In this case, the proliferative glandular tissue thickness is considered as half of the duct radius i.e., 0.25 mm. The glandular tissue is modeled as a tumor or malignant tissue.
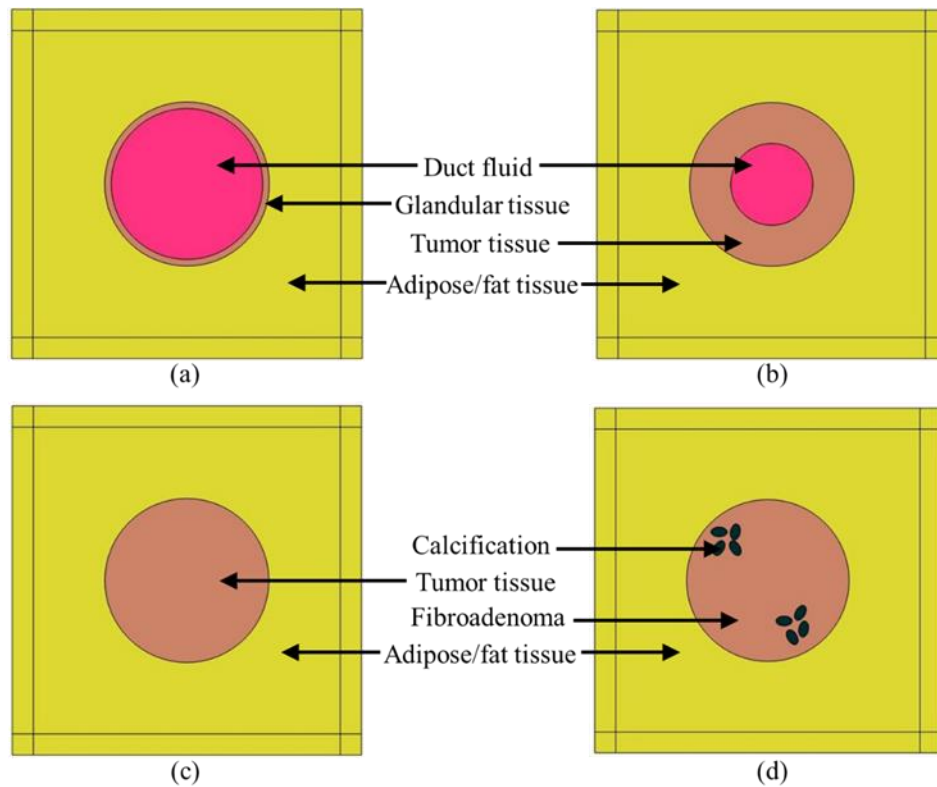
Fig.40 Breast duct models from DOE- (a) normal duct, (b) ductal hyperplasia, (c) duct with DCIS, (d) duct with calcification

The third model from the DOE, shown in Fig.40c was the DCIS breast duct model. Since DCIS is not invasive, the abnormal growth of epithelial cells is still confined by the duct. Therefore, in this model, the breast duct is filled with malignant/tumor tissue.

Calcification or microcalcification is a form of mineralization that can occur inside the duct due to different pathological conditions. To explore the feasibility of quantitative ultrasound in detecting calcification, the calcified duct analysis is conducted in an extended manner. All three types of micro-calcified (HAp, calcium carbonate, and calcium oxalate) ducts are included in the DOE. The HAp is associated with malignancy whereas calcium

carbonate (CC) and calcium oxalate (CO) are associated with the benign lesion. Two types of benign breast lumps are observed: (1) cysts and (2) fibroadenoma. The cyst is a sac filled with fluid whereas fibroadenoma represents the cell overgrowth inside the breast duct without being associated with malignancy [136]–[138]. As a benign lesion, fibroadenoma is chosen for modeling benign calcifications (CC and CO). The duct tissue for HAp is kept as tumor tissue whereas, for calcium carbonate and calcium oxalate, the duct tissue is kept as fibroadenoma (benign lesion). Usually, clustered microcalcifications are associated with DCIS [139]. In this model shown in Fig.40d, there were two microcalcification clusters with each having four oval-shaped calcified structures.

To create computational variation in all the surgical margin models, the duct is placed in five different positions in every margin model. One duct position is at the center of the tissue geometry. Two of the positions are at $\pm$ 0.4 mm from the center in the horizontal direction. The rest of the two positions are at $\pm$ 0.4 mm from the center in the vertical direction.

6.2   Finite Element Analysis

6.2.1   Simulation Physics

COMSOL Multiphysics software was used for the finite element analysis of the above-mentioned models from the DOE. The acoustic propagation could be modeled as either a longitudinal pressure wave or an elastic wave. In the case of tissue regions (fatty tissue, glandular tissue, tumor tissue, fibroadenoma), the stiffness was too low to accommodate elastic wave propagation [131]. Therefore, inside the tissue region as well as duct fluid, only longitudinal pressure wave propagation was modeled. For only longitudinal pressure

94

wave propagation, COMSOL solves the Helmholtz equation in pressure acoustics physics shown in Eq. (3.1), Eq. (3.3), Eq. (3.7), and Eq. (3.8) from section 3.2.1 and 3.2.2.

In the case of the microcalcification materials, the elastic wave propagation was supported due to the high stiffness. The strain value of the solid structure was too small to follow a non-linear stress-strain profile because of the smaller incident pressure ($\leq 1Pa$). Therefore, calcification materials were modeled as linearly elastic. For the elastic wave propagation, COMSOL solves the 2D Navier's equation in the solid mechanics physics shown in Eq. (3.4) from section 3.2.1. Since longitudinal wave was propagating through the tissue medium, and the elastic wave was propagating through the calcification medium, the respective Helmholtz equation and Navier's equation were coupled (micro calcified duct model) by the boundary conditions shown in Eq. (3.5) and Eq. (3.6) from section 3.2.1. The coupling included the tissue load on the calcification structure and the structural acceleration as experienced by the tissue.

6.2.2   Model Description

Fig.41 shows the detailed model description of the normal duct model. Ultrasound plane waves were sent along the positive x-direction of the model geometry. A perfectly matched layer (PML) was introduced to ensure that the sound wave left the model domain without any reflection. The computational analysis was conducted for both pitch-catch and pulse-echo propagation modes. For the pitch-catch mode, the scattered ultrasound pressure was measured at the back wall and for the pulse-echo mode, it was calculated at the front wall. A free triangular mesh was created in the tissue geometry and a mapped mesh was created in the PML region. A mesh sensitivity analysis was conducted to achieve convergence in

95

the simulation result. For this analysis, the maximum element size was selected as $\lambda/6$, $\lambda/7$, $\lambda/8$, and $\lambda/9$ where λ was the wavelength (μm). The convergence was achieved in all the models with a maximum element size of $\lambda/8$.
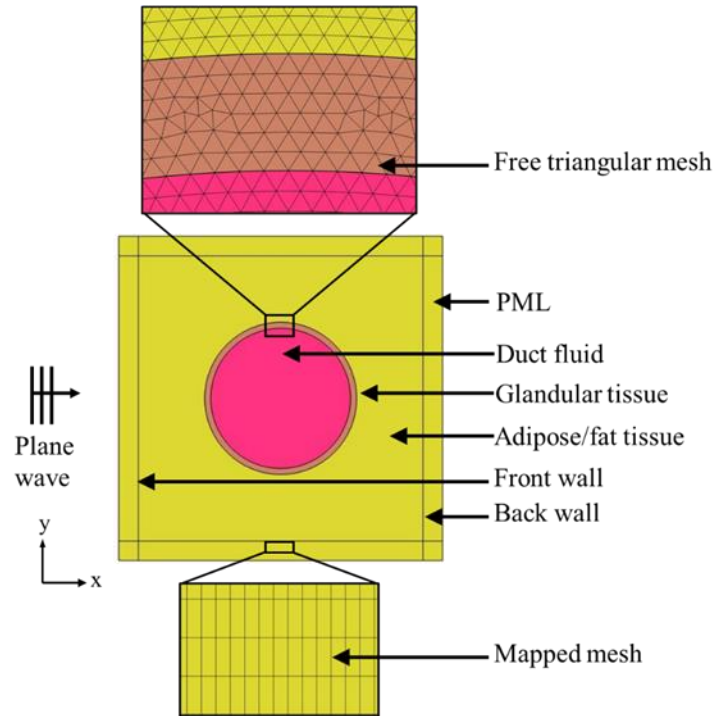
Fig.41 Computational model description

An extensive literature review was conducted to gather the material properties for different types of tissues as well as for microcalcification minerals [130], [140], [149]–[153], [141]–[148]. The material properties for all the tissues, duct fluid, and microcalcification minerals were listed in Table 6 and Table 7.

96

Table 6   Material properties for all tissues and duct fluid

	Density (ρ)	Sound speed (c)	Attenuation coefficient (α)
	kg/m^3	m/s	$Np/\text{m} - MHz$
Fatty tissue	869	1422	5.7
Glandular tissue	874	1487	10.5
Tumor tissue	1041	1548	11.28
Fibroadenoma	1060	1520	10.82
Duct fluid (water)	1000	1480	0.025

Table 7   Material properties for all microcalcification minerals

	Density (ρ)	Sound speed (c)	Young's modulus	Poisson's ratio
	kg/m^3	m/s	GPa	
Hydroxyapatite (HAp)	3180	1374	6	0.27
Calcium Carbonate	2930	5486	88.19	0.32
Calcium Oxalate	2200	4785	50.38	0.32

The simulation was conducted for a high-frequency range from 22 to 41 MHz to mimic a high-frequency transducer with frequency bandwidth. The transducer properties were followed similarly to the last study from section 5.3 (Fig.*33*).

6.2.3   Parameter Estimation

The frequency step size for the simulation was selected as 100 kHz. Therefore, starting from 22 MHz to 41 MHz, for every 100 kHz frequency increment, the ultrasound pressure wave was sent through the simulation model geometry. The average scattered pressure was measured at both the front and back wall for all 190 different frequencies. These pressure values were accumulated to create the frequency spectrum in both pulse-echo and pitch-catch mode.

To calculate the peak density parameter, the peaks and valleys were counted from the frequency spectrum [66]. To calculate the MPVD parameter, first, the pressure magnitude difference between each adjacent peak and valley was measured in the frequency spectrum. Then all these values were averaged to get the MPVD value for that corresponding spectrum. Additionally, the frequency spectrums from all the breast duct models were compared for both pulse-echo and pitch-catch modes to extract further pathology-based information.

6.3   Results and Discussion

Fig.42 shows the peak density and MPVD data from all the computational margin models for the pitch-catch ultrasound propagation mode. The mean peak density result was high for the normal duct inside the margin. With the increasing carcinoma level i.e., during hyperplasia and DCIS, the mean peak density started to decrease. When the calcification

98

was introduced in the duct, the peak density value again went up than the other carcinoma level. For the calcification models, from the peak density results, it was observed that both benign calcifications (CC and CO) had a similar mean peak density which was less than the malignant calcification (HAp). Without calcification, the standard deviation range of the malignant margin cases (ductal hyperplasia and DCIS) was outside (lower) of the range of the normal margin (normal duct). The standard deviation range of the calcified margin models was inside the range of the normal margin at some level.

In the case of the margin with normal duct, there were three different levels of materials i.e., fatty tissue, glandular tissue, and duct fluid. Thus, multiple ultrasound scattering occurred (at the fat-glandular tissue and glandular tissue-duct fluid interfaces). Therefore, the peak density value was high because peak density increases with an increasing level of scattering [70]. In the case of ductal hyperplasia inside the margin, although it had similar materials like the normal duct, the duct fluid region decreased to almost half, and the glandular tissue was substituted by the tumor tissue which covered more than half of the duct area. Compared to the duct fluid, tumor tissue possessed a very high attenuation coefficient. Therefore, the overall attenuation coefficient in the tumor-fluid region was higher than the glandular-fluid region from the normal duct. Accordingly, the acoustic scattering from the tumor-fluid interface became very insignificant since acoustic intensity decreased more compared to the normal duct. So, the hyperplasia model provided less peak density compared to the normal duct. In the case of the pure DCIS inside margin, there were only two materials (fatty tissue and tumor tissue). Therefore, the scattering level was lower than the previous two models and it yielded a further lower peak density value. When calcification was added to the model, multiple scattering again started to occur. Therefore,

99

the scattering level was high compared to the previous two carcinoma models. But since the tumor tissue (in case of HAp) and fibroadenoma (in case of CC and CO) occupied most of the duct area and had a high attenuation coefficient compared to the duct fluid (normal duct), the peak density value was lower for calcification compared to the normal duct. While comparing the benign and malignant calcification results, the stiffness of the CC and CO was much higher compared to that of HAp. From the literature, it was found that with increased stiffness in the material, the peak density decreases which complimented the result in this case [116].
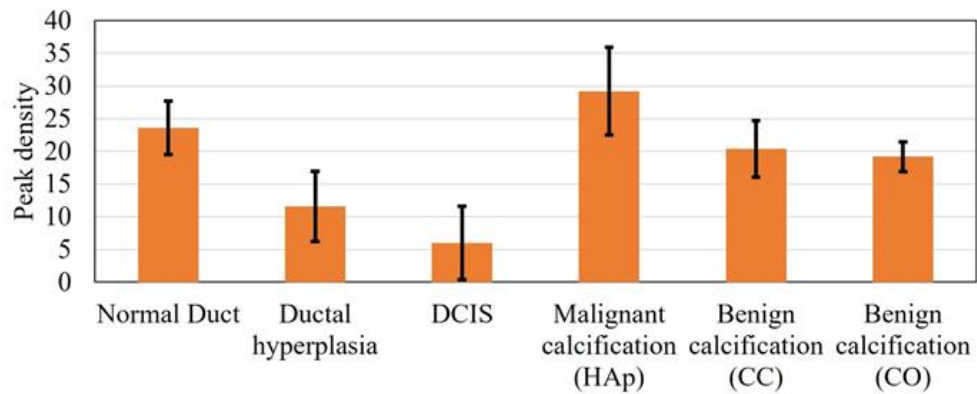
(a)
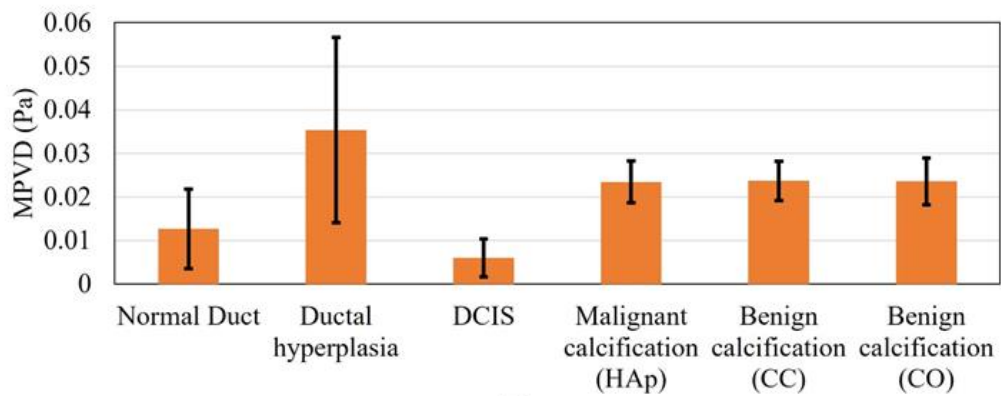
(b)

Fig.42 Parameter values for all the models in pitch-catch mode: (a) peak density, and (b)

MPVD

In the case of the MPVD results, the mean MPVD value of the hyperplasia model was the highest with the maximum standard deviation. The mean MPVD value for the normal duct and DCIS models was low compared to the hyperplasia and calcification models. Overall, the MPVD data failed to establish a meaningful trend with different duct pathologies. It was observed that both benign calcifications had a similar MPVD value which was slightly higher than the malignant calcification value.

Fig.43 shows the results of all the DOS models for the pulse-echo ultrasound propagation mode. In the case of the peak density results, all the margin models had higher peak density values except for the ductal hyperplasia. The highest mean value was recorded for the malignant calcification model. Overall, the peak density result in the pulse-echo mode failed to establish a meaningful trend with the margin models. In the case of pulse-echo mode, the scattered wave interacted with the incident wave while reaching the front wall of the model geometry. This might be one reason for the inconclusive relationship.

In the case of the MPVD data, the result was meaningful and was similar to the peak density result of the pitch-catch method. The mean MPVD of the normal duct was the highest and with increasing carcinoma, the value started to decrease. But when calcification was added to the model, the MPVD started to increase again. In contrast to the peak density pattern from the pitch-catch method, the malignant calcification MPVD was lower than the benign calcification MPVD value. But still, both benign calcification models provided similar

MPVD values which were similar to the "pitch-catch peak density" case (Fig.42a). Without calcification, the standard deviation range of the malignant margin cases (ductal hyperplasia and DCIS) was outside (lower) of the range of the normal margin (normal duct). The standard deviation range of the calcified margin models was also outside (lower) of the range of the normal margin. The difference in their range (malignant vs benign calcification) was partly distinguishable. From previous research, it was found that when peak density results provided similar values for different models, the MPVD became effective [68]. By definition, the MPVD depicted the average peak to valley pressure magnitude difference in a frequency spectrum. Therefore, even though the peak density was similar for all models, the spectrum pattern differed from each other because of the structural difference between all models. Accordingly, the change of values between all the peaks and valleys from different spectrums provided a meaningful MPVD correlation.
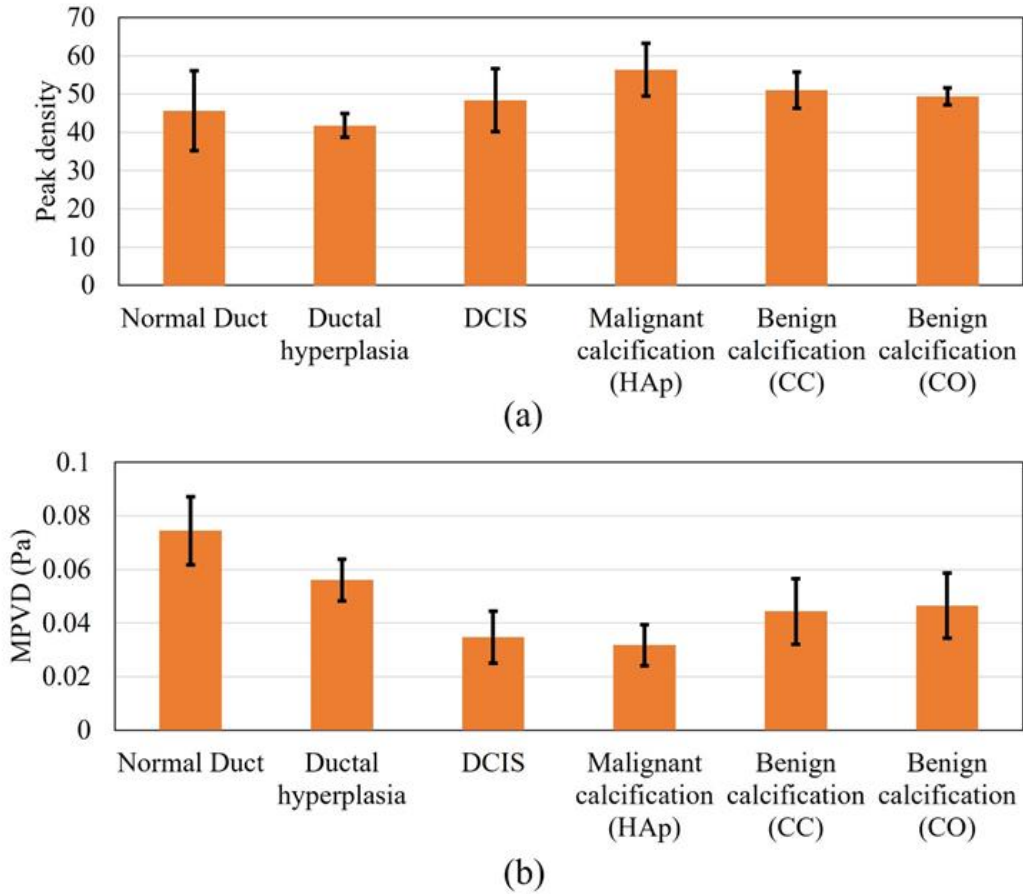
Fig.43 Parameter values for all the models in pulse-echo mode: (a) peak density, and (b) MPVD

In addition to analyzing the peak density and MPVD results, the frequency spectrums from all models were compared directly for both pulse-echo and pitch-catch ultrasound analysis modes. The goal of this analysis was to find specific patterns in the frequency spectrum which could provide more information about the different breast duct pathologies.

Fig.44 shows the frequency spectrums of all the margin models for the pitch-catch method of ultrasound analysis. From the figure, it was observed that the peak pressure values for

all the spectrums were at different frequency levels. The DCIS peak pressure was shifted to the right by approximately 3 MHz compared to the normal duct peak pressure. In the case of ductal hyperplasia, the peak pressure was shifted further right an additional 3 MHz compared to the DCIS model. Furthermore, only the peak pressure for the normal duct model occurred before the center frequency. In the case of DCIS and malignant calcification, the peak pressure was approximately at the center frequency. For the rest of the model spectrums, the peak pressure occurred after the center frequency. When calcification was added to the model, larger pressure magnitude variation (jaggedness) was observed compared to non-calcified models. The benign calcification (CC and CO) spectrums reached their peak pressure after 4 MHz com-pared with the malignant calcification (HAp) spectrum. The shifting peak pressure along the frequency axis was an outcome of the resonant frequency of material. At the resonant frequency, the material generates maximum sound pressure when subjected to external acoustic vibration. The resonant frequency changes with material properties. Therefore, with various tissue materials in the breast duct, different surgical mar-gin models possessed different resonant frequencies. Accordingly, the peak pressure of different models occurred at different frequencies. Thus, the frequency corresponding to the peak pressure could be an indicator of material properties as well as breast tissue pathologies. Additionally, the benign calcification spectrums were similar to each other explaining why they had similar peak density and MPVD. Overall, there was a clear difference between the malignant and benign calcification spectrums.
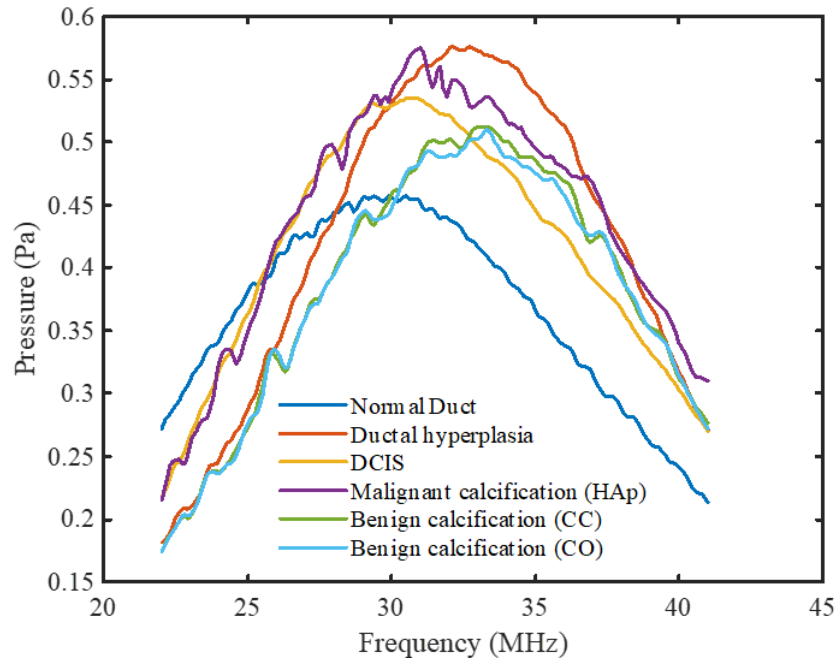
Fig.44 Frequency spectrums for all DOE models for the pitch-catch mode

Fig.45 shows the frequency spectrums of all the breast duct models for the pulse-echo method of ultrasound analysis. In this case, the spectrum patterns showed a clearer correlation between each other compared to the pitch-catch spectrums. Periodicity was observed in the normal duct spectrum due to the small thickness of the duct. The reflected acoustic wave from the duct wall came back to the front wall during its compression (high pressure) and rarefaction (low pressure) stages at the corresponding frequencies. With added malignancy and calcification in the normal duct geometry, the reflected wave from the tumor tissue as well as calcification started to contribute to the previous spectrum with different phases. Therefore, the periodicity in the spectrum started to fade away with malignancy. The overall patterns of the pulse-echo spectrums showed opposite characteristics to the pitch-catch spectrums. The peak pressure magnitude of the spectrums

105

shifted gradually to the left with added calcification level. Furthermore, the normal duct spectrum, in this case, had the highest overall pressure magnitude level with larger pressure magnitude variations between the peaks and valleys. Both the pressure level and peak to valley magnitude variation started to decrease with an added level of carcinoma. With the addition of calcification, they started to increase again. The calcification spectrums also showed the opposite trait to the previous method. In this case, the malignant calcification spectrum had a lower level of pressure magnitude and smaller variation compared to the benign calcification spectrums. However, similar to the previous mode, the CC and CO (benign) spectrum patterns were very similar as well as distinguishable to the HAp (malignant) spectrum.
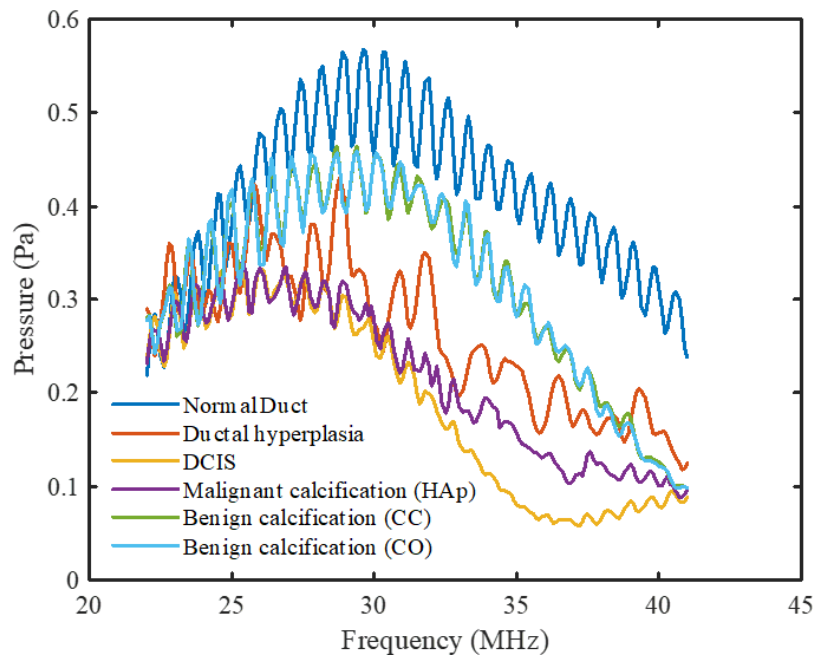
Fig.45 Frequency spectrums for all DOE models for the pulse-echo mode

Peak density in the pitch-catch method and MPVD in the pulse-echo method pro-vided meaningful trends with margin tissue pathologies. Although similar patterns were depicted by these response values for non-calcified margin models, the results were the opposite for the calcified models. In the case of the spectral comparison, some features of the frequency spectrums were found useful to differentiate the spectrums which were overall pressure magnitude level, peak pressure magnitude, and jagged-ness level of the spectrum. In the pulse-echo mode, DCIS can be identified by the low MPVD value as well as the low-pressure magnitude level in the spectrum with irregular jaggedness. Malignant calcification can be identified with a similar spectrum pattern with more jaggedness. In the pitch-catch mode, a lower peak density value can indicate the presence of the DCIS. Malignant calcification can be identified with a high peak density and high-pressure level in the frequency spectrum with distinguished and irregular jaggedness. By using quantitative ultrasound, the benign and malignant calcifications were differentiated at multiple levels. Therefore, the author's under-standing is that quantitative ultrasound analysis can be used as a very effective tool to identify different pathology levels of the margin intraoperatively. This characterization method can be implemented during breast conserving surgery to evaluate the surgical margin. Since the results can be obtained instantaneously, the surgeons will be able to understand the nature of the surgical margin histology (benign, malignant, or calcified) shortly after the tumor and margin excision. This will help the surgeons to decide whether or not further excision is necessary during the surgery. It is expected that including this method of margin characterization with conventional ultrasound imaging will increase the efficiency of the intraoperative ultrasound analysis by

107

reducing the reoperation rate among breast cancer patients. Furthermore, both pulse-echo and pitch-catch methods were found effective for this application although, for the latter method, it might be complicated to implement at the experimental level.

6.4 Conclusion

In this study, computational ultrasound analysis was conducted on different breast duct models that were created based on various malignant and benign cases. Quantitative parameters of high-frequency ultrasound (22-41 MHz) were used for the analysis. The analysis was conducted for both pulse-echo and pitch-catch ultrasound modes. It was found that the peak density parameter was effective in the pitch-catch method whereas the MPVD parameter was effective for the pulse-echo method. In both cases, the parameters showed a conclusive pattern to differentiate different breast duct pathology. The analysis was further extended to compare the frequency spectrums of all models. Spectral features like overall pressure magnitude, peak pressure magnitude, spectrum jaggedness were observed during the comparison. Pulse-echo and pitch-catch mode showed opposite traits for the spectrums in terms of these features. Compared to the pitch-catch mode, pulse-echo mode showed a more conclusive pattern in all the spectrums. Overall, quantitative ultrasound analysis was found effective for both methods to differentiate the pathological duct features. Along with ultrasound imaging, this analysis can be introduced to establish ultrasound as the primary and comprehensive tool for breast screening.

CHAPTER 7

CONCLUSION

7.1 Summary

The study was originally motivated by the necessity of creating an instantaneous margin detection process during breast conservation therapy. To this purpose, the study mainly focused on high-frequency ultrasound analysis of soft material because of its advantage of providing better axial and lateral resolution. For the quantitative ultrasound analysis, a comparatively new parameter, peak density was primarily selected for its sensitivity towards the microstructural change. The goal was to evaluate the feasibility of peak density in different aspects of ultrasound analysis for soft material characterization. The study was later expanded to identify the limitations of peak density parameters and address them by introducing a derivative parameter of peak density.

Chapter 0 started with a clear problem statement and research goal that was later achieved through this research. To understand ultrasound analysis and its application in material characterization, different types of ultrasound analysis processes were explained. Different types of ultrasound parameters were discussed including their limitations in material characterization. An extensive literature review was conducted on different aspects of soft material characterization which were addressed by the study that was included in the thesis. In chapter 2, underlying physics of ultrasound wave propagation in different types of material. An important characteristic of ultrasound propagation, acoustic scattering was discussed in detail which was beneficial to understand the peak density parameter of high-frequency ultrasound.

Chapter 3 illustrated a comprehensive study on the relationship between ultrasound parameters, peak density, and acoustic scattering which was fundamental towards understanding its feasibility in material characterization. The study was conducted in an analytical, computational, and experimental manner to establish peak density as a function of acoustic scattering.

One of the widely used ultrasound applications is ultrasound imaging. Therefore, in chapter 4, the application of peak density parameter in ultrasound C-scan imaging was shown through the computational study. The computational result was validated by the experimental outcome from the literature. The study was further extended to apply a derivative of peak density parameter named MPVD to detect structures relative position along with the depth during C-scan imaging. From the study, it was found that peak density and MPVD parameters can be used to produce a C-scan image of soft material as well as to detect its relative position.

After understanding the effectiveness of high-frequency ultrasound peak density and MPVD parameters, a similar analysis was applied to identify various histologic tumor grades (chapter 5). The study was conducted through finite element analysis of the cell-based model of breast tumors. In addition to the ultrasound parameters, the ultrasound frequency spectrums were also analyzed in the study. From this study, it was observed that through quantitative high-frequency ultrasound, histopathologic tumor grades can be identified which is beneficial during margin analysis.

Finally, the feasibility of high-frequency ultrasound was analyzed for detecting DCIS in the surgical margin of breast tumors (chapter 6). The goal was to identify different steps of

DCIS formation which is the most common form of non-invasive and asymptotic breast carcinoma. The study was conducted through finite element modeling and the study parameters were kept similar to chapter 5. All the pathologic cases associated with DCIS were included in that study. The results indicated that during breast-conserving surgery (lumpectomy), quantitative ultrasound has the potential to instantaneously identify DCIS in the surgical margin.

7.2   Scientific Contribution

The goal of this research was to establish ultrasound analysis as an instantaneous tissue margin detection tool through the QUS peak density and MPVD parameters. The research showed various aspects of ultrasound analysis that could be used for tissue characterization.

Breast cancer is the most common form of cancer among women in the United States and the second most common form of cancer among women worldwide. During breast conserving therapy, failing to identify breast tumor margin instantaneously as positive or negative, increases the re-excision rate as well as the local recurrence rate [154]. Furthermore, if a positive margin is found, the patient has to go through mental trauma to go for further surgery. Also, it is not economically feasible since BCT with radiation therapy costs on average $15,000 [155].

There are many intraoperative technologies available that are used to reduce the rate of positive margins. During lumpectomy, technologies like wire localization, radioactive seed localization, radioguided occult lesion localization, and ultrasound guidance were used for the excision of an adequate amount of tumor tissue including the margin [71]. In addition to that, intraoperative pathologic technologies like frozen section analysis, gross histology,

111

imprint cytology, specimen radiography, and sonography were also applied to lower the positive margin rates. These pathological techniques are comparatively time-consuming, resource-intensive, and require skilled operators [17], [156], [157]. Therefore, the findings from this research on quantitative ultrasound analysis will contribute to developing an ultrasound technology for instantaneous margin management which will ultimately decrease the reoperation and local recurrence rate. This will help breast cancer patients physically, psychologically, and financially.

Currently, mammography is considered the gold standard of breast screening for identifying non-invasive carcinoma like DCIS [81]. Some of its limitations such as screening dense breasts are solved by ultrasound imaging [80], [158]. Till now, ultrasound alone is not used for breast screening because of its limitations of providing false-positive results [159]–[161]. Ultrasound imaging in breast screening has limitations in detecting calcification [162], [163]. As a result, mammography is still the principal mode of breast screening which is comparatively expensive and deals with ionization. Establishing ultrasound analysis as the primary mode of breast screening can be a more economic and safer option. Therefore, combining the spectral-based ultrasound analysis from this research with conventional ultrasound imaging techniques can establish ultrasound as the primary breast screening method.

7.3   Future Recommendations

Based on the findings from the above studies, further research can be conducted on ultrasound peak density and MPVD parameters. The research can be done on evaluating

the parameters further as well as applying the parameters in other characterization fields. Some of the future research recommendations are discussed in this section.

7.3.1 Experimental Analysis on Real Tissue

In this thesis, chapters 5 and 6 discussed ultrasound analysis to identify tumor grades and specific tumor pathologies. The analysis was done computationally alone. Therefore, further research can be done on real tumors and breast pathology to analyze the effectiveness of peak density and MPVD on soft tissue characterization on an experimental level. Furthermore, the computational and experimental study can be expanded to characterize carcinoma in tissues of other human organs like the liver, kidney, uterus, etc.

7.3.2 Evaluating Various Transducer Properties

The current research on ultrasound peak density and MPVD parameters was associated with unfocused single-element transducers. Multiple array transducers have the capability of focusing and steering the ultrasound wave. Therefore, characteristics of the peak density and MPVD parameters can be evaluated for multiple-element transducers (e.g., linear array, circular array). Other than that, the parameters can be evaluated for a higher range of frequencies. By increasing the frequency level further (> 41 MHz) can change the scattering characteristic from diffractive to diffuse scattering. More information about peak density and MPVD parameters can be extracted from this analysis.

7.3.3 Photoacoustic Imaging

In recent years photoacoustic imaging showing great promise in the area of medical imaging [85], [95], [114], [164]. In photoacoustic imaging, the tissue absorbs optical energy (laser source) and generates a thermoelastic expansion which produces ultrasound

waves. In this case, the imaging process utilizes the optical absorbance property [165]. Therefore, materials that have similar acoustic properties, but different optical absorbance can be differentiated through photoacoustic imaging. In the case of C-scan imaging, the feasibility of peak density and MPVD parameters can be evaluated for photoacoustic imaging. If these parameters can be used for both ultrasound and photoacoustic imaging, combined imaging can be more effective than ultrasound imaging alone.

Instead of conducting the finite element modeling for the computational analysis of photoacoustic imaging, the k-space approach can be utilized. In finite element analysis, the mesh element size depends on the acoustic wavelength. Therefore, in the case of high-frequency wave propagation, it is really hard to conduct 3D simulation because of the large number of mesh elements being required to achieve convergence [68]. It was found that the k-space method offered comparatively low computational cost as well as better simulation efficiency [166]. Since it is a spectral method, it calculates the spatial gradients using FFTs. Therefore, it requires only two nodes per wavelength whereas the finite element analysis requires six to ten nodes per wavelength to achieve convergence. Realistic photoacoustic imaging can be performed in MATLAB through an open-source acoustic toolbox named k-Wave [167].

7.3.4 Characterization of Hard Materials

A similar technique to these above studies can be utilized to characterize hard materials. Hard materials accommodate elastic wave propagation due to having high stiffness. Therefore, additionally, wave mode conversion will occur in hard materials which can be correlated with peak density and MPVD parameters. Therefore, these parameters have the

114

potential for nondestructive testing of expensive materials in aerospace industries as well as medical industries (bone material characterization).

REFERENCE

[1]   C. H. Chen, *Ultrasonic and Advanced Methods for Nondestructive Testing and Material Characterization*. WORLD SCIENTIFIC, 2007.

[2]   R. Y. Chiao and L. J. Thomas, "Analytic evaluation of sampled aperture ultrasonic imaging techniques for NDE," *IEEE Trans. Ultrason. Ferroelectr. Freq. Control*, vol. 41, no. 4, pp. 484–493, Jul. 1994, doi: 10.1109/58.294109.

[3]   P. J. Shull, *Nondestructive evaluation: theory, techniques, and applications*. 2002.

[4]   J. Krautkrämer and H. Krautkrämer, *Ultrasonic Testing of Materials*. Berlin, Heidelberg: Springer Berlin Heidelberg, 1990.

[5]   "Breast Cancer Diagnosis - Types of Breast Cancer." https://www.cancer.org/cancer/breast-cancer/understanding-a-breast-cancer-diagnosis.html (accessed May 31, 2019).

[6]   "U.S. Breast Cancer Statistics | Breastcancer.org." https://www.breastcancer.org/symptoms/understand_bc/statistics (accessed Mar. 18, 2019).

[7]   C. E. DeSantis, J. Ma, A. Goding Sauer, L. A. Newman, and A. Jemal, "Breast cancer statistics, 2017, racial disparity in mortality by state," *CA. Cancer J. Clin.*, 2017, doi: 10.3322/caac.21412.

[8]   S. Litière *et al.*, "Breast conserving therapy versus mastectomy for stage I-II breast cancer: 20 year follow-up of the EORTC 10801 phase 3 randomised trial," *Lancet Oncol.*, vol. 13, no. 4, pp. 412–419, 2012, doi: 10.1016/S1470-2045(12)70042-6.

[9]   R. G. Pleijhuis, M. Graafland, J. De Vries, J. Bart, J. S. De Jong, and G. M. Van Dam, "Obtaining adequate surgical margins in breast-conserving therapy for patients with early-stage breast cancer: Current modalities and future directions," *Ann. Surg. Oncol.*, vol. 16, no. 10, pp. 2717–2730, 2009, doi: 10.1245/s10434-009-0609-z.

[10]   L. Jacobs, "Positive margins: The challenge continues for breast surgeons," *Ann. Surg. Oncol.*, vol. 15, no. 5, pp. 1271–1272, 2008, doi: 10.1245/s10434-007-9766-0.

[11]   S. E. Singletary, "Surgical margins in patients with early-stage breast cancer treated with breast conservation therapy," *Am. J. Surg.*, vol. 184, no. 5, pp. 383–393, 2002, doi: 10.1016/S0002-9610(02)01012-7.

[12]   A. L. Russo *et al.*, "Margin status and the risk of local recurrence in patients with early-stage breast cancer treated with breast-conserving therapy," *Breast Cancer Res. Treat.*, vol. 140, no. 2, pp. 353–361, 2013, doi: 10.1007/s10549-013-2627-6.

[13]   M. R. Kell, C. Dunne, J. P. Burke, and M. Morrow, "Effect of margin status on local recurrence after breast conservation and radiation therapy for ductal carcinoma in situ," *J. Clin. Oncol.*, vol. 27, no. 10, pp. 1615–1620, 2009, doi: 10.1200/JCO.2008.17.5182.

[14]   N. Houssami *et al.*, "Meta-analysis of the impact of surgical margins on local recurrence in women with early-stage invasive breast cancer treated with breast-conserving therapy," *Eur. J. Cancer*, vol. 46, no. 18, pp. 3219–3232, 2010, doi: 10.1016/j.ejca.2010.07.043.

[15]   K. E. Pengel *et al.*, "The impact of preoperative MRI on breast-conserving surgery of invasive cancer: A comparative cohort study," *Breast Cancer Res. Treat.*, vol. 116, no. 1, pp. 161–169, 2009, doi: 10.1007/s10549-008-0182-3.

[16]   M. Thill, K. Baumann, and J. Barinoff, "Intraoperative assessment of margins in breast conservative surgery - Still in use?," *J. Surg. Oncol.*, vol. 110, no. 1, pp. 15–20, 2014, doi: 10.1002/jso.23634.

[17]   T. P. Olson, J. Harter, A. Muñoz, D. M. Mahvi, and T. M. Breslin, "Frozen section analysis for intraoperative margin assessment during breast-conserving surgery results in low rates of re-excision and local recurrence," *Ann. Surg. Oncol.*, vol. 14, no. 10, pp. 2953–2960, 2007, doi: 10.1245/s10434-007-9437-1.

[18]   N. Lue *et al.*, "Portable optical fiber probe-based spectroscopic scanner for rapid cancer diagnosis: A new tool for intraoperative margin assessment," *PLoS One*, vol. 7, no. 1, 2012, doi: 10.1371/journal.pone.0030887.

[19]   T. Karni *et al.*, "A device for real-time, intraoperative margin assessment in breast-conservation surgery," *Am. J. Surg.*, vol. 194, no. 4, pp. 467–473, 2007, doi: 10.1016/j.amjsurg.2007.06.013.

[20]   M. Thill, "MarginProbe ® : intraoperative margin assessment during breast conserving surgery by using radiofrequency spectroscopy," *Expert Rev. Med. Devices*, vol. 10, no. 3, pp. 301–315, May 2013, doi: 10.1586/erd.13.5.

[21]   D. R. G. Faverly, J. H. C. L. Hendriks, and R. Holland, "Breast carcinomas of limited extent: Frequency, radiologic-pathologic characteristics, and surgical margin requirements," *Cancer*, vol. 91, no. 4, pp. 647–659, 2001, doi: 10.1002/1097-0142(20010215)91:4<647::AID-CNCR1053>3.0.CO;2-Z.

[22]   J. Mamou, M. L. Oelze, W. D. O'Brien, and J. F. Zachary, "Identifying ultrasonic

scattering sites from three-dimensional impedance maps," *J. Acoust. Soc. Am.*, vol. 117, no. 1, pp. 413–423, 2005, doi: 10.1121/1.1810191.

[23] L. G. Wilke *et al.*, "Rapid noninvasive optical imaging of tissue composition in breast tumor margins," *Am. J. Surg.*, vol. 198, no. 4, pp. 566–574, 2009, doi: 10.1016/j.amjsurg.2009.06.018.

[24] F. L. Lizzi, M. Greenebaum, E. J. Feleppa, M. Elbaum, and D. J. Coleman, "Theoretical framework for spectrum analysis in ultrasonic tissue characterization," *J. Acoust. Soc. Am.*, vol. 73, no. 4, pp. 1366–1373, 1983, doi: 10.1121/1.389241.

[25] E. P. Dimagno, P. T. Regan, J. E. Clain, E. M. James, and J. L. Buxton, "Human Endoscopic Ultrasonography," *Gastroenterology*, vol. 83, no. 4, pp. 824–829, 1982, doi: 10.1016/S0016-5085(82)80012-7.

[26] T. L. Szabo, *Diagnostic Ultrasound Imaging: Inside Out*, Second Edi. Elsevier, 2014.

[27] G. Ghoshal, M. L. Oelze, and W. D. O'brien, "Quantitative ultrasound history and successes," in *Quantitative Ultrasound in Soft Tissues*, Springer Netherlands, 2013, pp. 21–42.

[28] D. Zhang, X. Gong, and S. Ye, "Acoustic nonlinearity parameter tomography for biological specimens via measurements of the second harmonics," *J. Acoust. Soc. Am.*, vol. 99, no. 4, pp. 2397–2402, Apr. 1996, doi: 10.1121/1.415427.

[29] L. Taggart, R. Baddour, A. Giles, … G. C.-U. in medicine, and undefined 2007, "Ultrasonic characterization of whole cells and isolated nuclei," *Elsevier*, Accessed: Jun. 17, 2020. [Online]. Available: https://www.sciencedirect.com/science/article/pii/S0301562906017790.

[30] M. Insana, T. H.-U. imaging, and undefined 1990, "Parametric ultrasound imaging from backscatter coefficient measurements: image formation and interpretation," *Elsevier*, Accessed: Jun. 17, 2020. [Online]. Available: https://www.sciencedirect.com/science/article/pii/016173469090002F.

[31] M. Insana, R. Wagner, … D. B.-T. J. of the, and undefined 1990, "Describing small-scale structure in random media using pulse-echo ultrasound," *asa.scitation.org*, Accessed: Jun. 17, 2020. [Online]. Available: https://asa.scitation.org/doi/abs/10.1121/1.399283.

[32] M. Gudur, R. R. Rao, Y. S. Hsiao, A. W. Peterson, C. X. Deng, and J. P. Stegemann, "Noninvasive, quantitative, spatiotemporal characterization of mineralization in three-dimensional collagen hydrogels using high-resolution spectral ultrasound imaging," *Tissue Eng. - Part C Methods*, vol. 18, no. 12, pp. 935–946, Dec. 2012,

doi: 10.1089/ten.tec.2012.0180.

[33] F. Lizzi, M. Astor, E. Feleppa, … M. S.-U. in medicine &, and undefined 1997, "Statistical framework for ultrasonic spectral parameter imaging," *Elsevier*, Accessed: Jun. 12, 2020. [Online]. Available: https://www.sciencedirect.com/science/article/pii/S0301562997002007.

[34] M. C. Kolios, G. J. Czarnota, M. Lee, J. W. Hunt, and M. D. Sherar, "• Original Contribution ULTRASONIC SPECTRAL PARAMETER CHARACTERIZATION OF APOPTOSIS," 2002. Accessed: Jun. 17, 2020. [Online]. Available: www.mathworks.com.

[35] G. Ghoshal *et al.*, "Quantitative ultrasound imaging for monitoring in situ high-intensity focused ultrasound exposure," *Ultrason. Imaging*, vol. 36, no. 4, pp. 239–255, 2014, doi: 10.1177/0161734614524179.

[36] R. Libgot-Callé, F. Ossant, Y. Gruel, … P. L.-U. in medicine, and undefined 2008, "High frequency ultrasound device to investigate the acoustic properties of whole blood during coagulation," *Elsevier*, Accessed: Jun. 17, 2020. [Online]. Available: https://www.sciencedirect.com/science/article/pii/S0301562907003195.

[37] M. Lebertre, F. Ossant, L. Vaillant, … S. D.-U. in medicine &, and undefined 2002, "Spatial variation of acoustic parameters in human skin: an in vitro study between 22 and 45 MHz," *Elsevier*, Accessed: Jun. 17, 2020. [Online]. Available: https://www.sciencedirect.com/science/article/pii/S0301562902005008.

[38] B. Raju, K. Swindells, … S. G.-U. in medicine &, and undefined 2003, "Quantitative ultrasonic methods for characterization of skin lesions in vivo," *Elsevier*, Accessed: Jun. 17, 2020. [Online]. Available: https://www.sciencedirect.com/science/article/pii/S0301562903000097.

[39] J. B.-U. in medicine and undefined 1998, "Ultrasonic properties of tissues," *Inst. Phys. Publ. Bristol …*.

[40] S. Brand, E. Weiss, R. Lemor, & M. K.-U. in medicine, and undefined 2008, "High frequency ultrasound tissue characterization and acoustic microscopy of intracellular changes," *Elsevier*, Accessed: Jun. 17, 2020. [Online]. Available: https://www.sciencedirect.com/science/article/pii/S0301562908000495.

[41] S. Sathyanarayana *et al.*, "Challenges in Atherosclerotic Plaque Characterization With Intravascular Ultrasound (IVUS): From Data Collection to Classification," *IEEE Trans. Inf. Technol. Biomed.*, vol. 12, no. 3, p. 315, 2008, doi: 10.1109/TITB.2007.912352.

[42] F. L. Lizzi, M. Ostromogilsky, E. J. Feleppa, M. C. Rorke, and M. M. Yaremko,

"Relationship of Ultrasonic Spectral Parameters to Features of Tissue Microstructure," *IEEE Trans. Ultrason. Ferroelectr. Freq. Control*, vol. 34, no. 3, pp. 319–329, 1987, doi: 10.1109/T-UFFC.1987.26950.

[43] F. W. Kremkau, *Sonography Principles and Instruments*. 2014.

[44] K. Shung, R. S.-… on B. Engineering, and undefined 1976, "Scattering of ultrasound by blood," *ieeexplore.ieee.org*, Accessed: Jun. 17, 2020. [Online]. Available: https://ieeexplore.ieee.org/abstract/document/4121084/.

[45] K. Hoffmann, J. Jung, S. El Gammal, P. A.- Dermatology, and undefined 1992, "Malignant melanoma in 20-MHz B scan sonography," *karger.com*, Accessed: Jun. 17, 2020. [Online]. Available: https://www.karger.com/Article/Abstract/247403.

[46] E. Szymańska, A. Nowicki, K. Mlosek, … J. L.-E. journal of, and undefined 2000, "Skin imaging with high frequency ultrasound—preliminary results," *Elsevier*, Accessed: Jun. 17, 2020. [Online]. Available: https://www.sciencedirect.com/science/article/pii/S0929826600000975.

[47] B. Potkin, A. Bartorelli, J. Gessert, R. N.- Circulation, and undefined 1990, "Coronary artery imaging with intravascular high-frequency ultrasound.," *Am Hear. Assoc*, Accessed: Jun. 17, 2020. [Online]. Available: https://www.ahajournals.org/doi/abs/10.1161/01.cir.81.5.1575.

[48] C. R. Meyer, E. H. Chiang, K. P. Fechner, D. W. Fitting, D. M. Williams, and A. J. Buda, "Feasibility of high-resolution, intravascular ultrasonic imaging catheters," *Radiology*, vol. 168, no. 1, pp. 113–116, 1988, doi: 10.1148/radiology.168.1.3289084.

[49] M. D. Sherar, B. G. Starkoski, W. B. Taylor, and F. S. Foster, "A 100 MHz B-scan ultrasound backscatter microscope." Accessed: Jun. 17, 2020. [Online]. Available: https://www.sciencedirect.com/science/article/pii/0161734689900023.

[50] C. Pavlin, K. Harasiewicz, M. Sherar, F. F.- Ophthalmology, and undefined 1991, "Clinical use of ultrasound biomicroscopy," *Elsevier*, Accessed: Jun. 17, 2020. [Online]. Available: https://www.sciencedirect.com/science/article/pii/S016164209132298X.

[51] T. E. Doyle *et al.*, "Determining breast pathology in surgical margins with high-frequency ultrasound: phantom and numerical simulations," 2013, vol. 075081, pp. 075081–075081, doi: 10.1121/1.4800329.

[52] T. E. Doyle *et al.*, "High-frequency ultrasound for intraoperative margin assessments in breast conservation surgery: A feasibility study," *BMC Cancer*, vol. 11, 2011, doi: 10.1186/1471-2407-11-444.

[53] C. Carter, L. A. Neumayer, R. E. Factor, and T. E. Doyle, "Abstract P6-03-10: Using high-frequency ultrasound (20-80 MHz) to differentiate malignant vs benign breast tissue in surgical margins," *Cancer Res.*, vol. 78, no. 4 Supplement, pp. P6-03-10 LP-P6-03–10, Feb. 2018, [Online]. Available: http://cancerres.aacrjournals.org/content/78/4_Supplement/P6-03-10.abstract.

[54] C. E. Dalton, G. M. Wagner, H. A. Al-Ghaib, and T. E. Doyle, "Abstract P2-03-13: Pathology differentiation during breast conservation surgery using high-frequency ultrasound and peak frequency distribution," *Cancer Res.*, vol. 78, no. 4 Supplement, pp. P2-03-13 LP-P2-03–13, Feb. 2018, [Online]. Available: http://cancerres.aacrjournals.org/content/78/4_Supplement/P2-03-13.abstract.

[55] J. Stromer and L. Ladani, "Investigating ultrasound imaging in the frequency domain for tissue characterisation," *Nondestruct. Test. Eval.*, vol. 31, no. 3, pp. 209–218, 2016, doi: 10.1080/10589759.2015.1093627.

[56] G. Maskarinec, I. S. Pagano, M. A. Little, S. M. Conroy, S.-Y. Park, and L. N. Kolonel, "Mammographic density as a predictor of breast cancer survival: the Multiethnic Cohort," *Breast Cancer Res.*, vol. 15, no. 1, p. R7, Feb. 2013, doi: 10.1186/bcr3378.

[57] D. Gris, "Public Access NIH Public Access," vol. 185, no. 2, pp. 974–981, 2013, doi: 10.1038/mp.2011.182.doi.

[58] B. Alacam, B. Yazici, N. Bilgutay, F. Forsberg, and C. Piccoli, "• Original Contribution BREAST TISSUE CHARACTERIZATION USING FARMA MODELING OF ULTRASONIC RF ECHO," 2004, doi: 10.1016/j.ultra.medbio.2004.08.023.

[59] X. Z. Liu, X. F. Gong, D. Zhang, S. G. Ye, and B. Rui, "Ultrasonic characterization of porcine liver tissue at frequency between 25 to 55 MHz," *World J. Gastroenterol.*, vol. 12, no. 14, pp. 2276–2279, Apr. 2006, doi: 10.3748/wjg.v12.i14.2276.

[60] M. L. Oelze, J. F. Zachary, W. D. O'brien, and B. Program, "Characterization of tissue microstructure using ultrasonic backscatter: Theory and technique for optimization using a Gaussian form factor," *asa.scitation.org*, vol. 112, no. 3, pp. 1202–1211, Sep. 2002, doi: 10.1121/1.1501278.

[61] T. E. Doyle, "Iterative simulation of elastic wave scattering in arbitrary dispersions of spherical particles," *J. Acoust. Soc. Am.*, vol. 119, no. 5, pp. 2599–2610, 2006, doi: 10.1121/1.2184989.

[62] T. E. Doyle, A. T. Tew, K. H. Warnick, and B. L. Carruth, "Simulation of elastic wave scattering in cells and tissues at the microscopic level," *J. Acoust. Soc. Am.*, vol. 125, no. 3, pp. 1751–1767, 2009, doi: 10.1121/1.3075569.

121

[63] M. L. Oelze and J. F. Zachary, "• Original Contribution EXAMINATION OF CANCER IN MOUSE MODELS USING HIGH-FREQUENCY QUANTITATIVE ULTRASOUND," *Elsevier*, 2006, doi: 10.1016/j.ultrasmedbio.2006.05.006.

[64] Y. Bige, Z. Hanfeng, W. R.- Ultrasonics, and undefined 2006, "Analysis of microstructural alterations of normal and pathological breast tissue in vivo using the AR cepstrum," *Elsevier*, Accessed: Jun. 12, 2020. [Online]. Available: https://www.sciencedirect.com/science/article/pii/S0041624X05001058.

[65] K. P. E. Mercado, "Developing High-Frequency Quantitative Ultrasound Techniques to Characterize Three-Dimensional Engineered Tissues by," 2015.

[66] J. D. Stromer, "Evaluation of Soft Material Microstructure through High-frequency Ultrasound," 2016.

[67] L. Ladani, K. Paul, and J. Stromer, "High-Frequency Ultrasound Analysis in Both Experimental and Computation Level to Understand the Microstructural Change in Soft Tissues," in *Minerals, Metals and Materials Series*, Springer International Publishing, 2019, pp. 87–97.

[68] K. Paul, J. Stromer, S. Razmi, B. A. Pockaj, L. Ladani, and J. Razmi, "Computational Modeling of Ultrasound C-Scan Imaging Using Transmitted Signal Peak Density," *Appl. Sci. 2021, Vol. 11, Page 4924*, vol. 11, no. 11, p. 4924, May 2021, doi: 10.3390/APP11114924.

[69] A. Aubry, A. Derode, and M. Tanter, "Extraction of the multiple scattering contribution in weakly scattering media: Application to human soft tissues," *J. Acoust. Soc. Am.*, vol. 123, no. 5, pp. 3001–3001, May 2008, doi: 10.1121/1.2932568.

[70] K. Paul and L. Ladani, "Relationship between peak density and acoustic scattering in high-frequency ultrasound wave propagation," *SN Appl. Sci.*, vol. 2, no. 8, p. 1418, Aug. 2020, doi: 10.1007/s42452-020-03208-w.

[71] R. J. Gray, B. A. Pockaj, E. Garvey, and S. Blair, "Intraoperative Margin Management in Breast-Conserving Surgery: A Systematic Review of the Literature," *Ann. Surg. Oncol.*, vol. 25, no. 1, pp. 18–27, 2018, doi: 10.1245/s10434-016-5756-4.

[72] M. Ramos *et al.*, "Ultrasound-guided excision combined with intraoperative assessment of gross macroscopic margins decreases the rate of reoperations for non-palpable invasive breast cancer," *Breast*, vol. 22, no. 4, pp. 520–524, 2013, doi: 10.1016/j.breast.2012.10.006.

[73] M. Moschetta, M. Telegrafo, T. Introna, L. Coi, L. Rella, and V. Ranieri, "original

article Role of specimen US for predicting resection margin status," vol. 36, no. October, pp. 201–204, 2015.

[74] B. Mesurolle *et al.*, "Sonography of postexcision specimens of nonpalpable breast lesions: Value, limitations, and description of a method," *Am. J. Roentgenol.*, vol. 186, no. 4, pp. 1014–1024, 2006, doi: 10.2214/AJR.05.0002.

[75] V. Londero, C. Zuiani, M. Panozzo, A. Linda, R. Girometti, and M. Bazzocchi, "Surgical specimen ultrasound: Is it able to predict the status of resection margins after breast-conserving surgery?," *Breast*, vol. 19, no. 6, pp. 532–537, 2010, doi: 10.1016/j.breast.2010.06.001.

[76] E. R. St John *et al.*, "Diagnostic accuracy of intraoperative techniques for margin assessment in breast cancer surgery a meta-analysis," *Ann. Surg.*, vol. 265, no. 2, pp. 300–310, 2017, doi: 10.1097/SLA.0000000000001897.

[77] S. Y. Nam, L. M. Ricles, L. J. Suggs, and S. Y. Emelianov, "Imaging strategies for tissue engineering applications," *Tissue Eng. - Part B Rev.*, vol. 21, no. 1, pp. 88–102, Feb. 2015, doi: 10.1089/ten.teb.2014.0180.

[78] H. R. Kim and H. K. Jung, "Histopathology findings of non-mass cancers on breast ultrasound," *Acta Radiol. Open*, vol. 7, no. 6, p. 205846011877495, 2018, doi: 10.1177/2058460118774957.

[79] L. C. H. Leong, L. S. J. Sim, A. R. Jara-Lazaro, and P. H. Tan, "Ultrasound breast elastographic evaluation of mass-forming ductal carcinoma-in-situ with histological correlation - New findings for a toothpaste sign," *Asian Pacific J. Cancer Prev.*, vol. 17, no. 5, pp. 2673–2678, 2016, doi: 10.7314/APJCP.2016.17.5.2673.

[80] K. R. Cho *et al.*, "Non-calcified ductal carcinoma in situ: Ultrasound and mammographic findings correlated with histological findings," *Yonsei Med. J.*, vol. 49, no. 1, pp. 103–110, 2008, doi: 10.3349/ymj.2008.49.1.103.

[81] T. Nagashima *et al.*, "Ultrasound demonstration of mammographically detected microcalcifications in patients with ductal carcinoma in situ of the breast," *Breast Cancer*, vol. 12, no. 3, pp. 216–220, 2005, doi: 10.2325/jbcs.12.216.

[82] W. Li *et al.*, "Application of Contrast-Enhanced Ultrasound in the Diagnosis of Ductal Carcinoma In Situ: Analysis of 127 Cases," *J. Ultrasound Med.*, vol. 39, no. 1, pp. 39–50, 2020, doi: 10.1002/jum.15069.

[83] G. Ghoshal, M. L. Oelze, and W. D. O'brien, "Quantitative ultrasound history and successes," in *Quantitative Ultrasound in Soft Tissues*, Springer Netherlands, 2013, pp. 21–42.

[84] F. Lizzi, M. Ostromogilsky, … E. F.-I. transactions on, and undefined 1987, "Relationship of ultrasonic spectral parameters to features of tissue microstructure," *ieeexplore.ieee.org*, Accessed: Jun. 17, 2020. [Online]. Available: https://ieeexplore.ieee.org/abstract/document/1539921/.

[85] S. Sethuraman, J. H. Amirian, S. H. Litovsky, R. W. Smalling, and S. Y. Emelianov, "Ex vivo Characterization of Atherosclerosis using Intravascular Photoacoustic Imaging," *Opt. Express*, vol. 15, no. 25, p. 16657, Dec. 2007, doi: 10.1364/oe.15.016657.

[86] M. Versaci and F. C. Morabito, "Image Edge Detection: A New Approach Based on Fuzzy Entropy and Fuzzy Divergence," *Int. J. Fuzzy Syst.*, pp. 1–19, Feb. 2021, doi: 10.1007/s40815-020-01030-5.

[87] S. Madhukumar and N. Santhiyakumari, "Evaluation of k-Means and fuzzy C-means segmentation on MR images of brain," *Egypt. J. Radiol. Nucl. Med.*, vol. 46, no. 2, pp. 475–479, 2015, doi: 10.1016/j.ejrnm.2015.02.008.

[88] G. A. Gordon, S. Canumalla, and B. R. Tittmann, "Ultrasonic C-scan imaging for material characterization," *Ultrasonics*, vol. 31, no. 5, pp. 373–380, 1993, doi: 10.1016/0041-624X(93)90071-7.

[89] T. Kundu, M. Ehsani, K. I. Maslov, and D. Guo, "C-scan and L-scan generated images of the concrete/GFRP composite interface," *NDT E Int.*, vol. 32, no. 2, pp. 61–69, 1999, doi: 10.1016/S0963-8695(98)00044-9.

[90] M. Thornton, L. Han, and M. Shergold, "Progress in NDT of resistance spot welding of aluminium using ultrasonic C-scan," *NDT E Int.*, vol. 48, pp. 30–38, 2012, doi: 10.1016/j.ndteint.2012.02.005.

[91] R. Růžek, R. Lohonka, and J. Jironč, "Ultrasonic C-scan and shearography NDI techniques evaluation of impact defects identification," *NDT E Int.*, vol. 39, no. 2, pp. 132–142, 2006, doi: 10.1016/j.ndteint.2005.07.012.

[92] M. Restori and J. E. Wright, "C-scan ultrasonography in orbital diagnosis," *Br. J. Ophthalmol.*, vol. 61, no. 12, pp. 735–740, 1977, doi: 10.1136/bjo.61.12.735.

[93] T. Hasiotis, E. Badogiannis, and N. G. Tsouvalis, "Application of ultrasonic C-scan techniques for tracing defects in laminated composite materials," *Stroj. Vestnik/Journal Mech. Eng.*, vol. 57, no. 3, pp. 192–203, 2011, doi: 10.5545/sv-jme.2010.170.

[94] S. G. Ye, K. A. Harasiewicz, C. J. Pavlin, and F. S. Foster, "Ultrasound Characterization of Normal Ocular Tissue in the Frequency Range from 50 MHz to 100 MHz," *IEEE Trans. Ultrason. Ferroelectr. Freq. Control*, vol. 42, no. 1, pp. 8–

14, 1995, doi: 10.1109/58.368319.

[95]   H. Jin, S. Liu, R. Zhang, S. Liu, and Y. Zheng, "Frequency Domain Based Virtual Detector for Heterogeneous Media in Photoacoustic Imaging," *IEEE Trans. Comput. Imaging*, vol. 6, pp. 569–578, Jan. 2020, doi: 10.1109/tci.2020.2964240.

[96]   K. Imielińska, M. Castaings, R. Wojtyra, J. Haras, E. Le Clezio, and B. Hosten, "Air-coupled ultrasonic C-scan technique in impact response testing of carbon fibre and hybrid: Glass, carbon and Kevlar/epoxy composites," *J. Mater. Process. Technol.*, vol. 157–158, no. SPEC. ISS., pp. 513–522, 2004, doi: 10.1016/j.jmatprotec.2004.07.143.

[97]   J. P. S. Garcia, P. T. Garcia, R. B. Rosen, and P. T. Finger, "A 3-dimensional ultrasound C-scan imaging technique for optic nerve measurements," *Ophthalmology*, vol. 111, no. 6, pp. 1238–1243, 2004, doi: 10.1016/j.ophtha.2003.10.026.

[98]   T. E. Doyle *et al.*, "High-frequency ultrasound for intraoperative margin assessments in breast conservation surgery: A feasibility study," *BMC Cancer*, vol. 11, no. 1, p. 444, 2011, doi: 10.1186/1471-2407-11-444.

[99]   G. B. (George B. Arfken and H.-J. Weber, *Mathematical methods for physicists*. Academic Press, 1995.

[100]   K. Graff, "Wave motion in elastic solids: Oxford University Press," 1975.

[101]   D. Nicholas, C. Hill, D. N.-U. in M. & Biology, and undefined 1982, "Evaluation of backscattering coefficients for excised human tissues: principles and techniques," *Elsevier*, Accessed: Jun. 18, 2020. [Online]. Available: https://www.sciencedirect.com/science/article/pii/0301562982900643.

[102]   G. Kino, *Acoustic waves: devices, imaging, and analog signal processing*. 1987.

[103]   D. T. Blackstock, *Fundamentals of physical acoustics*. Wiley, 2000.

[104]   J. J. Faran, "Sound Scattering by Solid Cylinders and Spheres," *J. Acoust. Soc. Am.*, vol. 23, no. 4, pp. 405–418, 1951, doi: 10.1121/1.1906780.

[105]   R. Hickling, "Analysis of Echoes from a Solid Elastic Sphere in Water," *J. Acoust. Soc. Am.*, vol. 34, no. 10, pp. 1582–1592, Oct. 1962, doi: 10.1121/1.1909055.

[106]   M. P. Hossain and K. Paul, "Thermal conductivity analysis of single-walled carbon nanotube using finite element modeling," in *AIP Conference Proceedings*, Jul. 2018, vol. 1980, doi: 10.1063/1.5044375.

[107] E. L. Madsen, G. R. Frank, and F. Dong, "Liquid or solid ultrasonically tissue-mimicking materials with very low scatter," *Ultrasound Med. Biol.*, vol. 24, no. 4, pp. 535–542, 1998, doi: 10.1016/j.procs.2016.09.052.

[108] J. Stromer and L. Ladani, "Examination of a spectral-based ultrasonic analysis method for materials characterization and evaluation," *Biomed. Signal Process. Control*, vol. 40, pp. 454–461, 2018, doi: 10.1016/j.bspc.2017.10.010.

[109] S. L. Vieira, T. Z. Pavan, J. E. Junior, and A. A. O. Carneiro, "Paraffin-Gel Tissue-Mimicking Material for Ultrasound-Guided Needle Biopsy Phantom," *Ultrasound Med. Biol.*, vol. 39, no. 12, pp. 2477–2484, 2013, doi: 10.1016/j.ultrasmedbio.2013.06.008.

[110] K. Al Mahmud, F. Hasan, M. I. Khan, and A. Adnan, "On the Molecular Level Cavitation in Soft Gelatin Hydrogel," *Sci. Rep.*, vol. 10, no. 1, p. 9635, Jun. 2020, doi: 10.1038/s41598-020-66591-9.

[111] J. Nam, J. Byun, T. Kim, M. Kim, and D. Kim, "Measurement of Mechanical and Physical Properties of Pepper for Particle Behavior Analysis," *J. Biosyst. Eng.*, vol. 43, no. 3, pp. 173–184, 2018.

[112] S. Delrue, K. Van Den Abeele, E. Blomme, J. Deveugele, P. Lust, and O. B. Matar, "Two-dimensional simulation of the single-sided air-coupled ultrasonic pitch-catch technique for non-destructive testing," *Ultrasonics*, vol. 50, no. 2, pp. 188–196, 2010, doi: 10.1016/j.ultras.2009.08.005.

[113] B. Lashkari, L. Yang, and A. Mandelis, "The application of backscattered ultrasound and photoacoustic signals for assessment of bone collagen and mineral contents.," *Quant. Imaging Med. Surg.*, vol. 5, no. 1, pp. 46–56, 2015, doi: 10.3978/j.issn.2223-4292.2014.11.11.

[114] L. Xi, L. Zhou, and H. Jiang, "C-scan photoacoustic microscopy for invivo imaging of Drosophila pupae," *Appl. Phys. Lett.*, vol. 101, no. 1, p. 13702, Jul. 2012, doi: 10.1063/1.4732797.

[115] K. Paul, J. Stromer, S. Razmi, B. A. Pockaj, and L. Ladani, "Finite Element Analysis of Identifying Breast Cancer Tumor Grades Through Frequency Spectral Variation of High-Frequency Ultrasound," *IPEM-Translation*, vol. 1, p. 100003, Apr. 2022, doi: 10.1016/J.IPEMT.2022.100003.

[116] J. Stromer and L. Ladani, "Influence of Microstructure on the High-Frequency Ultrasound Measurement of Peak Density," *J. Nondestruct. Eval. Diagnostics Progn. Eng. Syst.*, vol. 1, no. 4, Nov. 2018, doi: 10.1115/1.4041067.

[117] H. Naujoks, "Rapid #: -17305186 Determining the Nuclear Area in Normal Breast

Epithelia," 2021.

[118] B. D. Lawrence, Z. Pan, A. Liu, D. L. Kaplan, and M. I. Rosenblatt, "Human corneal limbal epithelial cell response to varying silk film geometric topography in vitro," *Acta Biomater.*, vol. 8, no. 10, pp. 3732–3743, 2012, doi: 10.1016/j.actbio.2012.06.009.

[119] T. E. Doyle, A. T. Tew, K. H. Warnick, and B. L. Carruth, "Simulation of elastic wave scattering in cells and tissues at the microscopic level.," *J. Acoust. Soc. Am.*, vol. 125, no. 3, pp. 1751–1767, 2009, doi: 10.1121/1.3075569.

[120] H. Ben Pan, "The Role of Breast Ultrasound in Early Cancer Detection," *J. Med. Ultrasound*, vol. 24, no. 4, pp. 138–141, 2016, doi: 10.1016/j.jmu.2016.10.001.

[121] V. Londero, C. Zuiani, A. Furlan, J. Nori, and M. Bazzocchi, "Apporto dell'ecografia e della biopsia percutanea con guida ecografica nella diagnosi del carcinoma duttale in situ (CDIS) della mammella," *Radiol. Medica*, vol. 112, no. 6, pp. 863–876, 2007, doi: 10.1007/s11547-007-0183-z.

[122] "Ductal carcinoma in situ (DCIS) - Symptoms and causes - Mayo Clinic." https://www.mayoclinic.org/diseases-conditions/dcis/symptoms-causes/syc-20371889 (accessed Sep. 10, 2021).

[123] S. R. Wellings, "A Hypothesis of the Origin of Human Breast Cancer from the Terminal Ductal Lobular Unit," *Pathol. - Res. Pract.*, vol. 166, no. 4, pp. 515–535, Apr. 1980, doi: 10.1016/S0344-0338(80)80248-2.

[124] "hyperplasia-of-the-breast-ductal-or-lobular @ www.cancer.org." [Online]. Available: https://www.cancer.org/cancer/breast-cancer/non-cancerous-breast-conditions/hyperplasia-of-the-breast-ductal-or-lobular.html.

[125] T. Watanabe *et al.*, "Ultrasound Image Classification of Ductal Carcinoma In Situ (DCIS) of the Breast: Analysis of 705 DCIS Lesions," *Ultrasound Med. Biol.*, vol. 43, no. 5, pp. 918–925, 2017, doi: 10.1016/j.ultrasmedbio.2017.01.008.

[126] V. L. Ernster and J. Barclay, "Increases in Ductal Carcinoma In Situ (DCIS) of the Breast in Relation to Mammography: A Dilemma," *JNCI Monogr.*, vol. 1997, no. 22, pp. 151–156, Jan. 1997, doi: 10.1093/JNCIMONO/1997.22.151.

[127] S. KP, "Ductal carcinoma in situ of the breast: current concepts and future directions," *Arch. Pathol. Lab. Med.*, vol. 137, no. 4, pp. 462–466, Apr. 2013, doi: 10.5858/ARPA.2012-0078-RA.

[128] M. Shehata *et al.*, "Ductal Carcinoma in Situ: Current Concepts in Biology, Imaging, and Treatment," *J. Breast Imaging*, vol. 1, no. 3, pp. 166–176, 2019, doi:

10.1093/jbi/wbz039.

[129] K. Paul, S. Razmi, B. A. Pockaj, L. Ladani, and J. Stromer, "Finite Element Modeling of Quantitative Ultrasound Analysis of the Surgical Margin of Breast Tumor," *Tomogr. 2022, Vol. 8, Pages 570-584*, vol. 8, no. 2, pp. 570–584, Mar. 2022, doi: 10.3390/TOMOGRAPHY8020047.

[130] N. Martini *et al.*, "Characterization of breast calcification types using dual energy x-ray method," *Phys. Med. Biol.*, vol. 62, no. 19, pp. 7741–7764, 2017, doi: 10.1088/1361-6560/aa8445.

[131] N. G. Ramião, P. S. Martins, R. Rynkevic, A. A. Fernandes, M. Barroso, and D. C. Santos, "Biomechanical properties of breast tissue, a state-of-the-art review," *Biomech. Model. Mechanobiol.*, vol. 15, no. 5, pp. 1307–1323, 2016, doi: 10.1007/s10237-016-0763-8.

[132] "Breast Ultrasonography: Practice Essentials, Technique, Invasive Ultrasonography." https://emedicine.medscape.com/article/1948269-overview (accessed Sep. 15, 2021).

[133] D. M. Ferris-James, E. Iuanow, T. S. Mehta, R. M. Shaheen, and P. J. Slanetz, "Imaging approaches to diagnosis and management of common ductal abnormalities," *Radiographics*, vol. 32, no. 4, pp. 1009–1030, 2012, doi: 10.1148/rg.324115150.

[134] A. L. Amin, A. C. Purdy, J. D. Mattingly, A. L. Kong, and P. M. Termuhlen, "Benign Breast Disease," *Surg. Clin. North Am.*, vol. 93, no. 2, pp. 299–308, 2013, doi: 10.1016/j.suc.2013.01.001.

[135] "Nipple discharge - Mayo Clinic." https://www.mayoclinic.org/symptoms/nipple-discharge/basics/definition/sym-20050946 (accessed Sep. 06, 2021).

[136] "Fibroadenoma of the Breast Fact Sheet | Westmead BCI." https://www.bci.org.au/breast-cancer-information/fact-sheets/fibroadenoma-of-the-breast/ (accessed Sep. 13, 2021).

[137] "Fibroadenoma with microcalcifications | Radiology Case | Radiopaedia.org." https://radiopaedia.org/cases/fibroadenoma-with-microcalcifications?lang=us (accessed Sep. 13, 2021).

[138] "Common Benign Lumps | Johns Hopkins Medicine." https://www.hopkinsmedicine.org/health/conditions-and-diseases/common-benign-lumps (accessed Sep. 13, 2021).

[139] "Understanding Breast Calcifications."

https://www.breastcancer.org/symptoms/testing/types/mammograms/mamm_show/calcifications (accessed Sep. 15, 2021).

[140] M. M. Elsewe, "Evaluation of em absorption loss over breast mass for breast cancer diagnosis," *Proc. Annu. Int. Conf. IEEE Eng. Med. Biol. Soc. EMBS*, pp. 3897–3900, 2011, doi: 10.1109/IEMBS.2011.6090968.

[141] L. Keijzer, M. Lagendijk, … N. S.-P. of the, and undefined 2018, "Measurement of the speed of sound, attenuation and mass density of fresh breast tissue," *books.google.com*, Accessed: Aug. 23, 2021. [Online]. Available: https://books.google.com/books?hl=en&lr=&id=VTZMDwAAQBAJ&oi=fnd&pg=PA369&dq=measurement+of+the+sound+of+speed,+mass+density+and+attenuation+coeffiecient+of+fresh+beast+tissue&ots=wsDyvkTNz7&sig=qg1UF4wrbpYhrOY4laNBrp65nHw.

[142] C. Li, N. Duric, P. Littrup, and L. Huang, "IN VIVO BREAST SOUND-SPEED IMAGING WITH ULTRASOUND TOMOGRAPHY," *Ultrasound Med. Biol.*, vol. 35, no. 10, p. 1615, Oct. 2009, doi: 10.1016/J.ULTRASMEDBIO.2009.05.011.

[143] M. O. Culjat, D. Goldenberg, P. Tewari, and R. S. Singh, "A review of tissue substitutes for ultrasound imaging," *Ultrasound Med. Biol.*, vol. 36, no. 6, pp. 861–873, 2010, doi: 10.1016/j.ultrasmedbio.2010.02.012.

[144] K. Nam, J. A. Zagzebski, and T. J. Hall, "Quantitative Assessment of in vivo Breast Masses using Ultrasound Attenuation and Backscatter," *Ultrason. Imaging*, vol. 35, no. 2, p. 146, 2013, doi: 10.1177/0161734613480281.

[145] R. I. Martin and P. W. Brown, "Mechanical properties of hydroxyapatite formed at physiological temperature," *J. Mater. Sci. Mater. Med. 1995 63*, vol. 6, no. 3, pp. 138–143, Mar. 1995, doi: 10.1007/BF00120289.

[146] N. Sasaki, H. Umeda, S. Okada, R. Kojima, and A. Fukuda, "Mechanical properties of hydroxyapatite-reinforced gelatin as a model system of bone," *Biomaterials*, vol. 10, no. 2, pp. 129–132, 1989, doi: 10.1016/0142-9612(89)90046-X.

[147] B. J. Andrés, "CRC PR E S S PRINCIPLES and APPLICATIONS Biomaterials Edited by."

[148] F. Ren, E. D. Case, A. Morrison, M. Tafesse, and M. J. Baumann, "Resonant ultrasound spectroscopy measurement of Young's modulus, shear modulus and Poisson's ratio as a function of porosity for alumina and hydroxyapatite," *Philos. Mag.*, vol. 89, no. 14, pp. 1163–1182, 2009, doi: 10.1080/14786430902915388.

[149] J. Ekprasert, I. Fongkaew, P. Chainakun, R. Kamngam, and W. Boonsuan, "Investigating mechanical properties and biocement application of CaCO3

precipitated by a newly-isolated Lysinibacillus sp. WH using artificial neural networks," *Sci. Rep.*, vol. 10, no. 1, Dec. 2020, doi: 10.1038/S41598-020-73217-7.

[150] "Calcite Optical Material." https://www.crystran.co.uk/optical-materials/calcite-caco3 (accessed Sep. 13, 2021).

[151] D. Di Tommaso, S. E. R. Hernández, Z. Du, and N. H. de Leeuw, "Density functional theory and interatomic potential study of structural, mechanical and surface properties of calcium oxalate materials," *RSC Adv.*, vol. 2, no. 11, pp. 4664–4674, May 2012, doi: 10.1039/C2RA00832G.

[152] R. Vairavan *et al.*, "Single lump breast surface stress assessment study," *AIP Conf. Proc.*, vol. 1885, no. September, 2017, doi: 10.1063/1.5002444.

[153] M. P. André, C. H. Barker, N. Sekhon, J. Wiskin, D. Borup, and K. Callahan, "Pre-Clinical Experience with Full-Wave Inverse-Scattering for Breast Imaging," pp. 73–80, 2008, doi: 10.1007/978-1-4020-8823-0_10.

[154] T. S. Menes, P. I. Tartter, I. Bleiweiss, J. H. Godbold, A. Estabrook, and S. R. Smith, "The consequence of multiple re-excisions to obtain clear lumpectomy margins in breast cancer patients," *Ann. Surg. Oncol.*, vol. 12, no. 11, pp. 881–885, 2005, doi: 10.1245/ASO.2005.03.021.

[155] W. E. Barlow, S. H. Taplin, C. K. Yoshida, D. S. Buist, D. Seger, and M. Brown, "Cost Comparison of Mastectomy Versus Breast-Conserving Therapy for Early-Stage Breast Cancer," *JNCI J. Natl. Cancer Inst.*, vol. 93, no. 6, pp. 447–455, Mar. 2001, doi: 10.1093/JNCI/93.6.447.

[156] T. Osako *et al.*, "Efficacy of intraoperative entire-circumferential frozen section analysis of lumpectomy margins during breast-conserving surgery for breast cancer," *Int. J. Clin. Oncol.*, vol. 20, no. 6, pp. 1093–1101, 2015, doi: 10.1007/s10147-015-0827-2.

[157] B. W. Maloney, D. M. M. III, B. W. Pogue, K. D. Paulsen, W. A. W. M.D., and R. J. B. M.D., "Review of methods for intraoperative margin detection for breast conserving surgery," *https://doi.org/10.1117/1.JBO.23.10.100901*, vol. 23, no. 10, p. 100901, Oct. 2018, doi: 10.1117/1.JBO.23.10.100901.

[158] A. Izumori, K. Takebe, and A. Sato, "Ultrasound findings and histological features of ductal carcinoma in situ detected by ultrasound examination alone," *Breast Cancer*, vol. 17, no. 2, pp. 136–141, 2010, doi: 10.1007/s12282-009-0134-8.

[159] W. A. Berg *et al.*, "Combined screening with ultrasound and mammography vs mammography alone in women at elevated risk of breast cancer," *JAMA - J. Am. Med. Assoc.*, vol. 299, no. 18, pp. 2151–2163, 2008, doi: 10.1001/jama.299.18.2151.

[160] M. S. Bae *et al.*, "Breast Cancer Detected with Screening US: Reasons for Nondetection at Mammography," *https://doi.org/10.1148/radiol.13130724*, vol. 270, no. 2, pp. 369–377, Feb. 2014, doi: 10.1148/RADIOL.13130724.

[161] W. Buchberger, A. Niehoff, P. Obrist, P. DeKoekkoek-Doll, and M. Dünser, "Clinically and mammographically occult breast lesions: Detection and classification with high-resolution sonography," *Semin. Ultrasound, CT MRI*, vol. 21, no. 4, pp. 325–336, Aug. 2000, doi: 10.1016/S0887-2171(00)90027-1.

[162] C. YC *et al.*, "Sonographic evaluation of mammographically detected microcalcifications without a mass prior to stereotactic core needle biopsy," *J. Clin. Ultrasound*, vol. 30, no. 6, pp. 323–331, 2002, doi: 10.1002/JCU.10074.

[163] M. S. Soo, J. A. Baker, and E. L. Rosen, "Sonographic Detection and Sonographically Guided Biopsy of Breast Microcalcifications," *http://dx.doi.org/10.2214/ajr.180.4.1800941*, vol. 180, no. 4, pp. 941–948, Nov. 2012, doi: 10.2214/AJR.180.4.1800941.

[164] D. Piras, W. Xia, … W. S.-I. J. of, and undefined 2009, "Photoacoustic imaging of the breast using the twente photoacoustic mammoscope: present status and future perspectives," *ieeexplore.ieee.org*, Accessed: Sep. 17, 2020. [Online]. Available: https://ieeexplore.ieee.org/abstract/document/5353740/.

[165] P. Beard, "Biomedical photoacoustic imaging," *Interface Focus*, vol. 1, no. 4, p. 602, 2011, doi: 10.1098/RSFS.2011.0028.

[166] Q. Chang, T. Peng, and Y. Liu, "Tomographic damage imaging based on inverse acoustic wave propagation using k-space method with adjoint method," *Mech. Syst. Signal Process.*, vol. 109, pp. 379–398, 2018, doi: 10.1016/j.ymssp.2018.02.049.

[167] B. E. Treeby and B. T. Cox, "k-Wave: MATLAB toolbox for the simulation and reconstruction of photoacoustic wave fields," *J. Biomed. Opt.*, vol. 15, no. 2, p. 021314, 2010, doi: 10.1117/1.3360308.

APPENDIX A

MATLAB CODE

```matlab
%Calculating peak density

function count=count_peak(signal, thres)

%count_peak calculates the total number of peaks and valleys (peak density) in a
spectrum
%signal: frequency spectrum
%thres: threshold value during peak density calculation
%count: peak density

count = 0;
min = Inf;
max = -Inf;
slope = 0;

for i=1:length(signal)
 element = signal(i);
 if (element > max)
    max = element;
    %slope = 1;
 end
 if (element < min)
    min = element;
    %slope = 0;
 end

 if (slope ==1)
   if (element < max-thres)
    min = element;
    slope = 0;
    count = count +1;
   end
 else
   if (element > min+thres)
    max = element;
    slope = 1;
    count = count +1;
   end
 end
end
end
```

133

APPENDIX B

JAVA CODE

```java
//Creating random cell geometry (cytoplasm, nucleus) in COMSOL
int NUMBER_OF_CIRCLE = 3000; // Number of normal cell circle 1500
int NUMBER_OF_CANCER = 1500;
int nonOverlapArrayIndex = 0;

double[][] nonOverlappedAraay = new double[NUMBER_OF_CIRCLE][3];

double[] x1CordinateArray = new double[NUMBER_OF_CIRCLE];
double[] x2CordinateArray = new double[NUMBER_OF_CIRCLE];
double[] y1CordinateArray = new double[NUMBER_OF_CIRCLE];
double[] y2CordinateArray = new double[NUMBER_OF_CIRCLE];
double[] firtstRadiousArray = new double[NUMBER_OF_CIRCLE];
double[] secondRadiousArray = new double[NUMBER_OF_CIRCLE];

model.component("comp1").geom("geom1").lengthUnit("um");
model.component("comp1").geom("geom1").selection().create("csel1",
"CumulativeSelection");
model.component("comp1").geom("geom1").selection("csel1").label("cytoplasm");
model.component("comp1").geom("geom1").selection().create("csel2",
"CumulativeSelection");
model.component("comp1").geom("geom1").selection("csel2").label("nucleus");




double AREA_WIDTH = 1300.0;
double AREA_LENGTH = 1300.0;
double PML = 50.0;
double fixed_radius = 12.50; //cytoplasm radius
double normal_radius = 5.0; //nucleus radius
double cancer_radius = 8.0; //nuclear pleomorphism




model.component("comp1").geom("geom1").create("r1", "Rectangle");
model.component("comp1").geom("geom1").feature("r1").set("base", "center");
model.component("comp1").geom("geom1").feature("r1").set("size", new
double[]{AREA_LENGTH+2*PML, AREA_WIDTH+2*PML});
model.component("comp1").geom("geom1").feature("r1").set("layerleft", true);
model.component("comp1").geom("geom1").feature("r1").set("layerright", true);
model.component("comp1").geom("geom1").feature("r1").set("layertop", true);
model.component("comp1").geom("geom1").feature("r1").setIndex("layer", 50.0, 0);

for (int i = 0; i < NUMBER_OF_CIRCLE;) {
  //first circle

  x1CordinateArray[i] = (2.0*Math.random()-1.0)*AREA_LENGTH/2;
```

```java
y1CordinateArray[i] = (2.0*Math.random()-1.0)*AREA_WIDTH/2;
firtstRadiousArray[i] = fixed_radius;

if (i == 0) {
  nonOverlappedAraay[i][0] = x1CordinateArray[i];
  nonOverlappedAraay[i][1] = y1CordinateArray[i];
  nonOverlappedAraay[i][2] = firtstRadiousArray[i];
  nonOverlapArrayIndex++;
  i++;
  continue; //first circle
}

//second circle from previous circle
boolean overlap = false;
for (int j = 0; j < nonOverlapArrayIndex; j++) {

  double x1 = x1CordinateArray[i];
  double x2 = nonOverlappedAraay[j][0];
  double y1 = y1CordinateArray[i];
  double y2 = nonOverlappedAraay[j][1];
  double r1 = firtstRadiousArray[i];
  double r2 = nonOverlappedAraay[j][2];

  double l = Math.sqrt((x1-x2)*(x1-x2)+(y1-y2)*(y1-y2));
  if (l <= r1+r2) {
    System.out.println("Circumference of C1  and C2  intersect");
    overlap = true;
    break;
  }

  else {
    System.out.println("C1 and C2  do not overlap");
    overlap = false;
  }

}

if (Math.abs(x1CordinateArray[i]) > ((AREA_LENGTH/2)-firtstRadiousArray[i]) ||
Math.abs(y1CordinateArray[i]) > ((AREA_WIDTH/2)-firtstRadiousArray[i]))
{
  continue;
}

if (overlap == false) {
  nonOverlappedAraay[nonOverlapArrayIndex][0] = x1CordinateArray[i];
```

136

```
        nonOverlappedAraay[nonOverlapArrayIndex][1] = y1CordinateArray[i];
        nonOverlappedAraay[nonOverlapArrayIndex][2] = firtstRadiousArray[i];
        nonOverlapArrayIndex++;

        int ind = i;

        model.component("comp1").geom("geom1").create("c"+ind, "Circle");
        model.component("comp1").geom("geom1").feature("c"+ind).set("r",
firtstRadiousArray[i]);
        model.component("comp1").geom("geom1").feature("c"+ind).set("pos", new
double[]{x1CordinateArray[i], y1CordinateArray[i]});

        with(model.component("comp1").geom("geom1").feature("c"+ind));
          set("contributeto", "csel1");
        endwith();
        ind++;

        if (i <= NUMBER_OF_CANCER) {
          model.component("comp1").geom("geom1").create("c"+ind, "Circle");
          model.component("comp1").geom("geom1").feature("c"+ind).set("r", cancer_radius);
          model.component("comp1").geom("geom1").feature("c"+ind).set("pos", new
double[]{x1CordinateArray[i], y1CordinateArray[i]});

          with(model.component("comp1").geom("geom1").feature("c"+ind));
            set("contributeto", "csel2");
          endwith();
        }

        else {
          model.component("comp1").geom("geom1").create("c"+ind, "Circle");
          model.component("comp1").geom("geom1").feature("c"+ind).set("r",
normal_radius);
          model.component("comp1").geom("geom1").feature("c"+ind).set("pos", new
double[]{x1CordinateArray[i], y1CordinateArray[i]});

          with(model.component("comp1").geom("geom1").feature("c"+ind));
            set("contributeto", "csel2");
          endwith();
        }

        ind++;

        i = i+2;
      }
}
```

```
model.component("comp1").geom("geom1").run();
```